White Rose Research Online

eprints@whiterose.ac.uk
https://eprints.whiterose.ac.uk
Universities of Leeds, Sheffield and York

Deposited via The University of Sheffield.

White Rose Research Online URL for this paper:
https://eprints.whiterose.ac.uk/id/eprint/174337/

Version: Accepted Version

Article:
Bernardo, G., Lopes, T., Lidzey, D.G. et al. (2021) Progress in upscaling organic photovoltaic devices. Advanced Energy Materials, 11 (23). 2100342. ISSN: 1614-6832

https://doi.org/10.1002/aenm.202100342

This is the peer reviewed version of the following article: Bernardo, G., Lopes, T., Lidzey, D. G., Mendes, A., Progress in Upscaling Organic Photovoltaic Devices. Adv. Energy Mater. 2021, 2100342., which has been published in final form at https://doi.org/10.1002/aenm.202100342. This article may be used for non-commercial purposes in accordance with Wiley Terms and Conditions for Use of Self-Archived Versions.

Reuse
Items deposited in White Rose Research Online are protected by copyright, with all rights reserved unless indicated otherwise. They may be downloaded and/or printed for private study, or other acts as permitted by national copyright laws. The publisher or other rights holders may allow further reproduction and re-use of the full text version. This is indicated by the licence information on the White Rose Research Online record for the item.

Takedown
If you consider content in White Rose Research Online to be in breach of UK law, please notify us by emailing eprints@whiterose.ac.uk including the URL of the record and the reason for the withdrawal request.

UNIVERSITY OF LEEDS
University of Sheffield
UNIVERSITY of York

Progress in upscaling organic photovoltaic devices

Gabriel Bernardo[1,*], Tânia Lopes[1], David Lidzey[2], Adélio Mendes[1]

[1]LEPABE, Department of Chemical Engineering, University of Porto, 4200-465 Porto, Portugal

[2]Department of Physics and Astronomy, The University of Sheffield, Sheffield S3 7RH, U.K.

Corresponding author's email: gbernardo@fe.up.pt

Abstract

Organic photovoltaic (OPV) cells have recently undergone a rapid increase in power conversion efficiency (PCE) under AM 1.5G conditions, as certified by the National Renewable Energy Laboratory (NREL), which have jumped from 11.5 % in October 2017 to 18.2 % in December 2020. However, the NREL certified PCE of large area OPV modules is still lagging far behind (11.7 % in July 2020). Additionally, there has been a rapidly growing interest in the use of OPVs for dim light indoor applications, with reported PCE of some large area ($\geq$ 1 cm^2) devices, under 1000 lx, well above 20 %. The transition of OPV from the lab to the market requires the development of effective manufacturing processes that can scale-up laboratory-scale devices into large area devices, without sacrificing performance and simultaneously minimizing associated manufacturing costs. This review article focuses on four important challenges that OPV technology has to face to achieve a reliable lab-to-fab transfer, namely: i) the upscaling of ITO-based single cells and the interconnection of single cells into large area modules (single cells *vs* modules); ii) the development of alternatives to vacuum processing (vacuum-based processing *vs* vacuum-free processing); iii) the development of alternatives to ITO-based substrates (ITO-based devices *vs* ITO-free devices) and iv) strategies for improving the lifetime of large area OPV cells and modules. As a benchmark for upscaling, this review mainly reports the development and characterization of devices (single cells and modules) with an active area $\geq$ 1.0 cm^2.

1. Introduction

Among the emerging solar cell technologies, organic photovoltaic cells (OPVs) have attracted great interest due to their promising performance and potential for low cost manufacture. OPVs can be manufactured over large areas, on lightweight plastic substrates with high flexibility, using high-throughput roll-to-roll (R2R) fabrication, which is compatible with solution processing technologies, potentially resulting in large reductions in fabrication costs and in the energy payback time (EPBT).

Research in OPVs started in the 1980's with the demonstration of a bilayer device, based on copper phthalocyanine and a perylene tetracarboxylic derivative, that exhibited a power conversion efficiency (PCE) of ~1 %, as described in the seminal work by Tang [1]. Later, in 1992, Sariciftci et al. [2] reported photo-induced electron transfer from a conducting polymer to fullerene. As a way to deal with the short exciton diffusion lengths in organic semiconductors, in 1995 Heeger et al. [3] introduced the concept of interpenetrating bicontinuous network of donor and acceptor materials, known as bulk-heterojunction (BHJ). OPVs were dominated by fullerene-based acceptors [4, 5] for over two decades but, due to rapid developments in non-fullerene acceptors (NFA), fullerene acceptors have been outperformed in efficiency and progressively replaced by NFAs [6-12]. After a period of slow progress in the efficiency of small area (typically < 10 mm^2) single junction OPV devices, observed between ~2012 – 2018, OPVs have witnessed a rapid development in the last two years, with NREL certified efficiencies under AM 1.5G conditions jumping from 11.5 % in October 2017 to 18.2 % in December 2020 [13]. These outstanding improvements were largely due to the development of new polymer donors [14-21] and new NFAs [19-23], and have caused a surge of research activity in the OPV field.

In recent years, OPV devices have attracted growing interest as energy harvesters for indoor environments under artificial light sources, such as white light-emitting diodes (LEDs) and fluorescent lamps [24-31]. The cell requirements for indoor and outdoor light are crucially different, as the indoor light power is typically <1.0 $mW \cdot cm^{-2}$, i.e. 100-1000 times weaker than in AM 1.5G (100 $mW \cdot cm^{-2}$) and the spectrum of the indoor light is narrower and limited to the wavelength range 400-700 nm. Recent studies have demonstrated the high potential of OPVs for indoor applications, with reported PCE for small area devices of 28 % [32] and more recently 31 % [33]. OPVs are, therefore,

currently envisaged as a future indoor energy harvester technology for powering low-power electronics and portable devices for the Internet of Things [26].

Despite such progress, the potential advantages that OPV devices have to offer are still far from being a reality. Record OPV efficiencies are typically achieved with small active area devices (< 1.0 cm^2), produced on rigid glass substrates under inert conditions, employing costly vacuum deposition steps and costly and scarce elements such as indium in the semi-transparent front electrode. For example, the current maximum NREL certified PCE of modules with an active area ranging 200-800 cm^2 is 11.7 % [34]; a value much lower than 18.2 % reported for small area devices.

There are several key challenges that OPV technology has to overcome to achieve a reliable lab-to-fab transfer [35]. One upscaling challenge is related to the choice and optimization of the photo-active layer (PAL), including its deposition method. As a result of the limited exciton diffusion length (~10 nm) and charge carrier mobility in organic semiconductors, the optimized thickness of the PAL in OPVs is typically less than 300 nm. Furthermore, the performance of large area OPV cells and modules is very sensitive to the presence of defects (which cause leakage currents) and thickness inhomogeneities in the active layer [36, 37]. Therefore, one of the great challenges in the fabrication of high-efficiency large-area OPVs consists in the deposition of thin defect-free PAL with a homogeneous thickness over large areas. The upscaling of OPVs requires the use of large scale deposition methods such as inkjet printing [38, 39], spray coating [40, 41], doctor-blading/blade coating, slot-die coating, knife coating, gravure printing, flexographic printing, rotary screen printing and flat-bed screen printing. All these printing and coating techniques have their own advantages and disadvantages and they have been extensively described in a number of review articles [41-49]. Other upscaling challenges relate to the use of green solvent formulations for PAL deposition, which replace the halogenated solvents typically used in small scale device development [43, 50-53]. Other challenges concerns the development of new molecularly engineered donor and acceptor materials that can exhibit a high efficiency when formed into thick active layers (desirable for upscaling) [42, 43, 54, 55]. These challenges have been previously reviewed [42, 43, 50, 54, 56], including some very recent reviews [42, 43, 50, 54], and will not be the subject of specific attention here.

This review mostly addresses the development of single cells and modules with an active area ≥ 1.0 cm^2, which has been considered as the minimum critical area for a scalability proof-of-principle [54, 57, 58], and will focus on the following key issues:

Single cells *versus* modules: Strategies are needed for upscaling individual cells and for upscaling modules of serially connected cells, minimizing performance losses. The efficiencies reported for large area cells are typically significantly lower than for small area cells, due to factors such as the limited conductivity of the transparent contact and the occurrence of film thickness heterogeneities in the PAL. A general technique to overcome the limited conductivity of the transparent contact is by connecting several smaller cells in series. This ensures that the photocurrent produced by the module is limited, while the voltage increases linearly with the number of cells. The production of these monolithically series-connected OPV cells requires patterning of each deposited layer to electrically connect them together. This technique, however, can also introduce large photocurrent and electrical fill factor losses which are mainly caused by the high electrical resistance of the interconnects.

ITO-based *versus* ITO-free devices: Indium-tin-oxide (ITO) is commonly used as a transparent conductive electrode in OPV cells and modules, however indium is an expensive and rare metal. Furthermore, ITO only has a modest conductivity limiting the current extraction from large area devices. It also only has modest mechanical flexibility which makes it inappropriate for flexible device applications. For these reasons, several strategies explore replacing the ITO bottom electrode in large area devices.

Vacuum-based *versus* vacuum-free processing: Top (back) metal electrodes are usually deposited by thermal evaporation under vacuum. This vacuum-based process restricts the high throughput manufacture goal of OPVs and increases the associated costs. Solution-processed electrodes, to be used as alternative to the thermally evaporated electrodes, are therefore highly desirable as they could reduce significantly the EPBT.

Improving the stability of large-area OPVs: The operational lifetimes of large area devices are still significantly lower than the market requirements of ≥ 10 years. Strategies are needed to improve the stability of the devices including the development of new encapsulation strategies.

This review article is divided in three main parts: the first part (Section 2), addresses the upscaling of OPV devices based on ITO substrates and is divided in two sub-sections,

which deal with the upscaling of single cells and the upscaling of modules consisting of connected cells. Inside each of these sub-sections, the upscaling using vacuum-based and vacuum-free processing are also considered separately. The second part (Section 3), addresses the upscaling of ITO-free cells and modules and separately considers the upscaling using different types of ITO-free bottom electrodes such as metal-based, carbon-based and conducting polymer-based bottom electrodes. The third part (Section 4) then, addresses the testing and improvement of the operational lifetime stability of large area ($\geq$ 1 cm^2) devices. Finally, Section 5 draws general conclusions regarding the future development of this very active research field.

2. Upscaling of ITO-based devices

Indium tin oxide (In_2O_3:Sn, ITO) possesses a large number of highly mobile free carriers and an energy bandgap ~3.8 eV. Due to these properties, ITO exhibits low electronic resistivity (~10–20 Ω/□ on glass) and high optical transparency (>80 % in the visible region), and is the most commonly used transparent bottom (front) electrode for OPVs [59]. ITO can be deposited on glass or plastic substrates by sputtering under ultra-high vacuum (UHV).

This section reviews the upscaling of OPV devices based on ITO bottom electrodes and is divided in two parts: Section 2.1 deals with upscaling of single cells and Section 2.2. deals with the upscaling of modules of serially connected cells.

2.1. Upscaling of ITO-based single cells

The most significant upscaling studies of ITO-based single cells are reviewed here and the performance of the most representative devices, processed either with or without metal evaporated top electrodes, are indicated in Table S1 in Supporting Information and are shown in Figure 1.

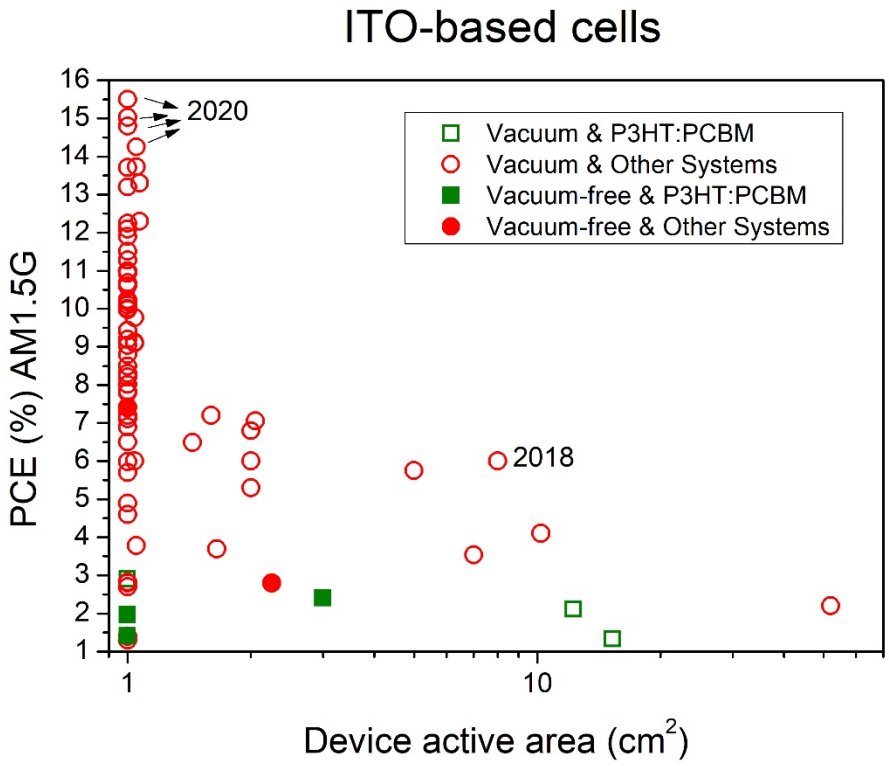

Figure 1. Performance of large area (≥ 1 cm^2) ITO-based OPV single cells under AM 1.5G conditions. The highest efficiency cells have been reported very recently, as indicated.

2.1.1. With vacuum conditions

The large majority of studies on the upscaling of ITO-based single cells have relied on the use of top electrodes evaporated under vacuum conditions and follow different strategies to achieve highly efficient devices with active areas ≥ 1.0 cm^2. Some studies have focused on optimizing large area coating and printing techniques; others have tested new donors, new acceptors and new ternary PALs; different devices architectures and cathode interfacial layers have also been considered.

Among the scalable coating and printing techniques studied for large area OPVs are blade-coating [60-64], slot-die coating [64-69], spray-coating [70-76], inkjet-printing [77-79], maobi coating [37] and wire-bar coating [80].

Blade-coating of PALs, consisting of the donor:acceptor blend PBTA-TF:IT-M from non-halogenated solvent mixtures was used to produce cells with an active area of 1 cm^2 and a PCE of 10.6 % [60]. Blade-coating was also explored by some authors [61-63] to deposit the PAL films by layer-by-layer (LbL) sequential processing, using non-orthogonal solvents. As compared to the common BHJ strategy, LbL presents several unique advantages including a much greater control of the D:A morphology over large areas, as well as better charge transport and extraction properties. Using this strategy, OPV cells based on bilayer donor:acceptor PALs were reported with an active area of 1.0 cm^2 and PCEs > 10 %, outperforming the corresponding standard donor:acceptor (BHJ) based devices [61-63]. The work by Sun et al. [63] is particularly impressive, wherein they used an LbL blade-coating strategy to produce cells with an average PCE of 15.03 % compared to PCE of 14.01 % for reference BHJ based devices. These cells had the structure ITO/PEDOT:PSS/PAL/PNDIT-F3N-Br/Ag, where the PAL consisted of the polymer donor PM6 and the NFA Y6.

An innovative deposition method was reported by Kim et al. [64] to simplify the fabrication of tandem OPVs. PAL materials (PTB7-Th:$PC_{71}BM$) were mixed with a non-conjugated polyelectrolyte [polyethyleneimine (PEI)]. widely used as a cathode interfacial material. A blade or slot-die coating the PEI:PAL nanocomposite was used to create a bilayer with a PEI bottom layer and a PAL top layer via a spontaneous vertical phase separation of the materials driven by their surface energy differences. Cells with an active area of 1.0 cm^2 achieved a PCE of 9.1 %.

Cells with area of 2 cm^2 and a PAL of PTB7:$PC_{71}BM$ deposited using a slot-die R2R coating approach that combined additives and the use of an in-line drying oven, achieved an average PCE of 5.30 % [66]. A sequential slot-die (SSD) coating strategy, using a non-halogenated solvent, was used to deposit a ternary PAL, composed of PTB7-Th:PCBM: *p*-DTS($FBTTH_2$)$_2$, forming flexible cells with areas of 1 and 2 cm^2, achieving PCEs of 7.11 % and 6.8 % respectively [67]. A study of the effect of shear impulse during coating on the morphology of BHJs, reported 1.04 cm^2 cells based on two different slot-die coated PALs of PTB7-Th:$PC_{71}BM$ and PBDB-T:ITIC, with maximum PCEs reported of 9.10 % and 9.77 % respectively [68]. Wu et al. [69] reported slot-die coated cells with 1.0 cm^2 active area and PCE of 11.19 % based on the NFA system PBDB-T-SF:IT-4F.

Spray-coating has been explored as a scalable PAL deposition technique to produce large area OPV cells [70-76] and the corresponding mechanisms of film formation have been studied in detail [74]. Notably, Park et al. [70] created cells with size of 12.5 cm^2 and PCE of 1.68 % from spray-coated P3HT:PCBM. Yang and co-workers [72] reported OPV cells with active areas of 1.0 and 10.2 cm^2 and PCEs of respectively 4.6 % and 4.1 % based on spray-coated PALs of PBDT-TFQ:$PC_{71}BM$. Later, the same authors [75] used spray-coating to deposit the PAL system PBTI3T:$PC_{71}BM$ in single cells with an active area of 1 cm^2 that achieved an optimized PCE of 6.10 %. These are amongst the highest efficiency large area cells based on spray-coated PALs reported so far in the literature.

Inkjet printing has also been studied to deposit the PAL of large area OPV cells [77-79]. Reference cells with 1 cm^2 active area, based on PV2000 PAL, inkjet printed using non-halogenated solvents, achieved a PCE of 4.9 % [78]. Corzo et al. [79] reported 1.0 and 2.0 cm^2 active area cells with PCEs of ~6 %, based on an inkjet printed P3HT:O-IDTBR PAL, which are amongst the highest performances reported for inkjet printed large area cells. One of the main advantages of inkjet printing – freedom of design – was also exploited by fabricating a 2.2 cm^2 solar cell in the form of a marine turtle, as shown in Figure 2. This cell achieved a PCE of 4.76 %, therefore demonstrating the versatility of digital inkjet printing for free-form manufacturing.

Maobi coating has been used to patch defects in the spin-coated PAL of large area cells, based on PBDB-T:ITIC [37]. Cells with areas of 1.6, 8 and 52 cm^2 achieved PCEs of respectively 7.2, 6.0 and 2.2 %, where the larger cells contained a silver grid deposited on ITO to reduce the carrier collection path length.

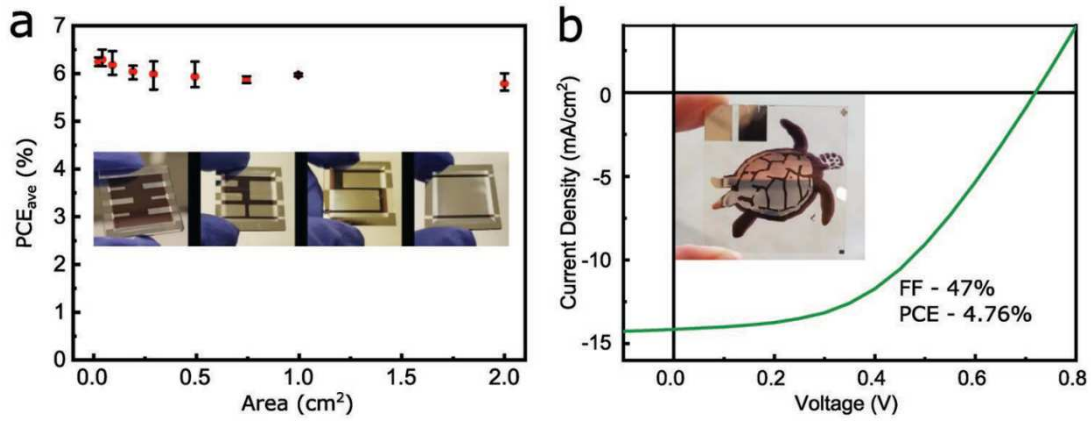

Figure 2. a) The performance of P3HT:O-IDTBR devices as a function of cell area and b) *J–V* of free-form inkjet-printed solar cell in the shape of a marine turtle on top of ITO glass. (reproduced with permission from ref. [79]).

Scalable techniques have also been investigated for the deposition of interfacial layers. Notably, Kang et al. [80] demonstrated cells with an active area of 1.0 cm^2 and PCE of 10.1 %, with structure glass/ITO/MoOx/PB3T:I-TM/PFN-Br/Al, where a very thin and highly uniform MoOx interfacial layer was wire-bar coated.

In the above studies of scalable processing techniques, the PAL was deposited either under ambient or inert conditions, however comparative studies of these two processing conditions are scarce. Dkhil et al. [81] reported 1.0 cm^2 cells based on PTB7-Th:$PC_{71}BM$ achieving PCEs of 7.84 % and 7.08 % when processed under inert and air conditions respectively.

Optimizing the molecular structures of organic photoactive materials has been the most successful method to increase the performance of the OPV devices and hence new NFAs [82-85], polymer donors [86-90] and small-molecule donors [91] have been tested with much success in large area cells.

In a seminal work, Zhao et al. [82] reported, in 2016, OPV cells with 1.0 cm^2 and structure ITO/ZnO/PBDB-T:ITIC/MoO_3/Al with a certified PCE of 10.78 %; a value much higher than the PCE of 7.45 % for a reference PBDB-T:$PC_{71}MB$ based device, resulting from a much broader PAL absorption band and a more appropriate molecular energy level alignment. This was the first example of a NFA-based OPV cell exhibiting higher PCE than the corresponding fullerene-based OPV and paved the way for the outstanding improvements in PCE observed in the following years. More recently, Cui et al. [83, 84] reported new NFAs with improved performances in OPV cells. First, the fluorine atoms

on BTP-4F (Y6) were replaced with chlorine atoms originating BTP-4Cl, which has an extended optical absorption [83]. Single cells with an active area of 1 cm^2 (Figure 3) and inverted structure ITO/ZnO/PBDB-TF:BTP-4Cl/MoO_3/Al, achieved a PCE of 15.3 % and improved V_{OC}, mainly due to reduced non-radiative energy losses, combined with a broader photo-response range. However, the BTP-4Cl has poor solubility and to improve the relationship between solubility and device efficiency, the alkyl chains in BTP-4Cl were later finely tuned creating the material BTP-eC9 [84]. OPV cells with an active area 1 cm^2 and structure glass/ITO/PEDOT:PSS/PBDB-TF:BTP-ec9/PFN-Br/Al, where the PAL was blade-coated, achieved a very impressive maximum PCE of 16.2 % (average 15.5 %), which is among the top performances for single-junction OPV cells with an active area ≥ 1.0 cm^2, due to improved J_{SC} and FF.

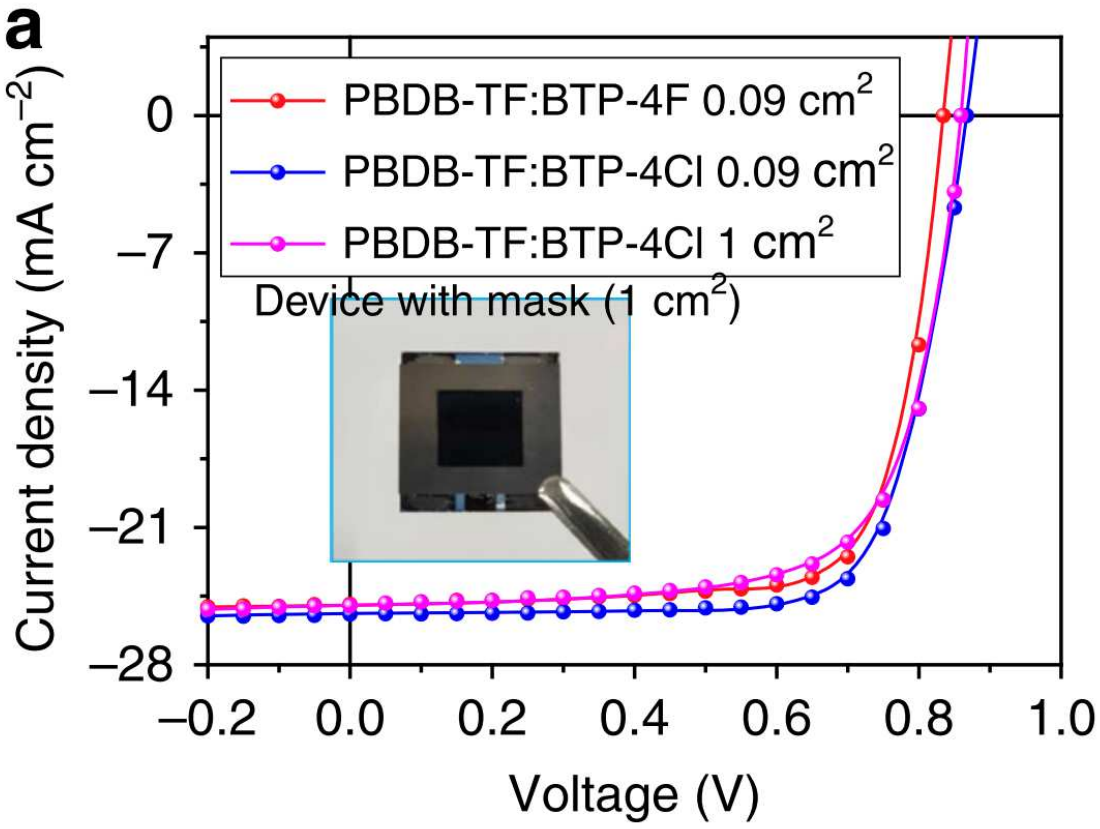

Figure 3. *J-V* curves of PBDB-TF:BTP-4Cl cell with active area of 1 cm^2. *J-V* curves for small area devices are shown for comparison (reproduced with permission from ref. [83]).

Different novel polymeric donors have been tested in large area OPV cells including the random co-polymers PTAZDCB20 [86] and PDT2fBTBT10 [87], the chlorinated polymer PBDB-T-2Cl [88], P2F-EHp [89] and the copolymer T1 (0.8 PBDB-TF + 0.2 PTO_2) [90]. Replacement of the fluorine atoms in PBDB-T-2F with chlorine atoms

originating PBDB-T-2Cl was shown to reduce the polymer HOMO and LUMO levels, contributing to an increase in V_{OC} and PCE of the corresponding devices [88]. Cells with the structure ITO/ZnO/PBDB-T-2Cl:IT-4F/MoO_3/Al and with an active area 1 cm^2, achieved a PCE of 11.51 %. Fan et al. [89] synthesized new polymer donors (P2F-EH, P2F-EHp, P2F-EO) by fine-tuning modification of the side chains or end groups of existing high-performance polymers, and tested them in OPV devices. A certified PCE of 12.25 % was achieved in single cells with an active area of 1 cm^2 based on the structure ITO/PEDOT:PSS/P2F-EHp: IT-2F/PFNDI-Br/Ag. Cui et al. [90] (2019) synthesized copolymers of PBDB-TF with PTO2 which, compared with PBDB-TF, show lower HOMO levels and broader optical absorption and are very soluble in most common solvents including non-halogenated solvents. OPV cells with 1 cm^2 and inverted structure ITO/ZnO/PAL/MoO_3/Al, where the PAL was blade-coated from non-halogenated solvents and consisted of a blend of copolymer T1 (0.8 PBDB-TF + 0.2 PTO_2) and the small molecule NFA IT-4F, achieved a PCE of 13.1 %.

Ternary blending of the PAL, either with two donors and one acceptor (D_1:D_2:A) or with one donor and two acceptors (D:A_1:A_2), has also proved and effective strategy to increase the PCE of devices compared to the corresponding devices based on binary blends [92-95]. The D_1:D_2:A strategy was used by Zhang et al. [92] to produce cells with 5 cm^2 active area and PCE of 5.75 % based on PTB7-Th:p-DTS($FBTTH_2$)$_2$:$PC_{71}BM$. Liu et al. [93] reported 1.05 cm^2 active area OPV cells based on two different ternary blade-coated PAL structures: PM6/ICBA:IT-4F (named as PPHJ) and PM6:ICBA:IT-4F (BHJ), where ICBA is a minority component. Devices with PPHJ and BHJ structures achieved PCEs of 14.25 % and 13.73 % respectively - both higher than similar devices without ICBA. Baran et al. [94] used a ternary blend D:A_1:A_2 strategy to produce 1 cm^2 active area cells with structure ITO/ZnO/P3HT:IDTBR:IDFBR/MoO_3/Ag, which achieved a PCE of 6.5 %. The improved PCE, compared to the binary blend, was assigned to improved light harvesting in the visible region and to changes in microstructure that reduced charge recombination and increase the photo-voltage. All-polymer cells based on the ternary blend PBTA-Si:PTzBI-Si:N2200 were reported by Fan et al. [95]. Cells with 1.0 cm^2 active area and structure custom-ITO/PEDOT:PSS/PAL/PFNDI-Br/Ag, achieved a PCE of 10.01 %, where the custom-ITO, had a metal frame on its periphery.

A different strategy to optimize the performance of large area single cells has consisted in the study of different cell architectures [96] and different cathode interfacial layers

(CIL) [97-99]. Some authors [36, 96] reported that multi-junction (tandem, triple, four) ITO-based cells suffer lower reductions in PCE on upscaling than the corresponding single junction cells, suggesting that multi-junction OPV cells can achieve higher efficiency and improved scalability. Kang et al. [97] studied the impact of different CILs on the performance of cells with structure ITO/PEDOT:PSS/PBDB-T-2F:IT-4F/CIL/Al. The best performances were obtained with a CIL consisting of naphthalene diimide (NDI)-based organic molecule (NDI-N), with cells having a 1.0 cm^2 active area achieved a PCE of 13.2 %. Another study addressed the impact of the surface morphology of a ZnO CIL on the performance of inverted OPV cells [98]. Bai et al. [99] produced highly efficient (average PCE = 11.28 %) semi-transparent cells with 1 cm^2 active area and structure ITO/$Al(acac)_3$/PM6:Y6/MoO_3/Ag (15 nm), where aluminum(III) acetylacetonate $Al(acac)_3$ was used as a novel CIL.

Large area ITO-based single cells, with top electrodes evaporated under vacuum, exhibited promising PCE values (particularly considering they were fullerene-based), have also been reported, sometimes as reference cells [100-103].

Large area ITO-based OPV single cells are also being investigated for indoor applications and the first report was made by Steim et al. [104] in 2011. Cells based on P3HT:PCBM and with an area of 1 cm^2, achieved a PCE of 2.7 % under AM 1.5G conditions (i.e. 100,000 lx) and achieved a PCE of ~7 %, corresponding to a power output of 19 $\mu W \cdot cm^{-2}$, under a fluorescent lamp with 1000 lx. The requirements of shunt (R_p) and serial (R_s) resistances were observed to be different for indoor and outdoor cells, with indoor cells coping with higher R_s values ($R_s \leq 50\ \Omega \cdot cm^{-2}$) than outdoor cells ($R_s \leq 3\ \Omega \cdot cm^{-2}$) but requiring higher R_p values ($R_p \geq 85\ k\Omega \cdot cm^{-2}$) than outdoor cells ($R_p \geq 1\ k\Omega \cdot cm^{-2}$).

Quite recently, Cui et al. [85] synthesized a novel NFA (IO-4Cl) and blended it with PBDB-TF to obtain a PAL with an absorption spectrum that matches that of indoor light sources. Under AM 1.5G conditions, 1 cm^2 cells with the acceptor IO-4Cl achieved a PCE of 9.80 % which was lower than that reference cells with the acceptor IT-4F (PCE = 12.5 %) having an identical size. By contrast, under light from a 2,700K LED lamp at 1000 lux, the same IO-4Cl-based cells achieved a PCE of 26.1 %; a value that was much greater than the PCE of 21.2 % obtained with the IT-4F-based cells. These results showed that the best blend compositions for AM 1.5G and indoor conditions are not necessarily the same. The IO-4Cl-based cells were then up-scaled to an active area of 4 cm^2 and the

corresponding PCE at 1000 lux was determined as 23.9 %. The authors observed that under indoor lighting, the parasitic R_s caused by the transparent electrodes was not a limiting factor to the PCE and therefore large-area OPV cells do not need to be made of thin strips. Additionally, under indoor lighting the performance of OPVs was observed to be less dependent on the PAL thickness than under 1 Sun AM 1.5 G conditions, meaning that thickness uniformity requirements over large areas are less stringent for indoor applications; a result that potentially facilitates upscaling using printing techniques.

In other work [105], 1 cm^2 active area cells were studied with two additional PAL blends (PBDB-TF:ITCC and PBDB-TF:$PC_{71}BM$). Under AM 1.5G conditions, ITCC and $PC_{71}BM$ based cells achieved PCEs of 10.3 % and 8.43 % respectively. Under 1000 lux (2700 K) LED illumination, the ITCC-based cell achieved a PCE of 22.0 % with a V_{OC} of 0.962 V corresponding to an output power (P_{out}) of 66.5 $\mu W.cm^{-2}$, and the $PC_{71}BM$-based cell achieved a PCE of 18.1 % with a V_{OC} of 0.784 V and a P_{out} of 54.7 $\mu W.cm^{-2}$. The performance of OPV cells for indoor applications was again observed to be less dependent on the PAL thickness.

2.1.2. With vacuum-free conditions

Upscaling studies of ITO-based cells under vacuum-free conditions, i.e. not relying on the use of thermal evaporated top electrodes, have been scarce and explore different vacuum-free processing strategies for depositing the top electrodes.

Eutectic metal alloys with low melting points (m.p.), such as Wood´s metal (m.p. ~70 ºC – 50% Bi : 25 % Pb : 12.5 % Cd : 12.5 % Sn) and Field's metal (m.p. of ~62 ºC - 51 % In : 32.5 % Bi : 16.5 % Sn), were coated at temperatures above melting point and tested as top electrodes in large area OPV cells [106-108], but with very limited success (Table S1). Using Field's metal cathode, the best PCEs reported were 2.4 % in P3HT:PCBM cells with an active area of 3 cm^2 [107] and 3.1 % in PTB7:$PC_{71}BM$ cells with an active area of 2.25 cm^2 [108].

Silver inks have also been deposited using inkjet or screen-print (under ambient conditions) and used as the top electrodes (either grids or full-layers) of large area OPV cells, however the reported results were quite modest [109, 110] (Table S1).

A more successful vacuum-free processing approach was reported by Czolk et al. [101] who produced reference ITO-based OPV cells, with 1.0 cm^2 active area and top electrodes

consisting of Ag nanowires (AgNWs) intermixed with PEDOT:PSS. These cells had the structure glass/ITO/PEDOT:PSS/ZnO/PAL/AgNWs:PEDOT:PSS, where the PAL consisted of a ternary blend of PffBT4T-2OD:$PC_{61}BM$:$PC_{71}BM$, and achieved an impressive PCE of 7.4 %

2.2. Upscaling of ITO-based modules

In this section the most significant upscaling studies of ITO-based OPV modules are reviewed. The performances of the most representative ITO-based OPV large area modules, processed with and without top metal evaporated electrodes, are shown in Table S2 in Supporting Information and plotted in Figure 4.

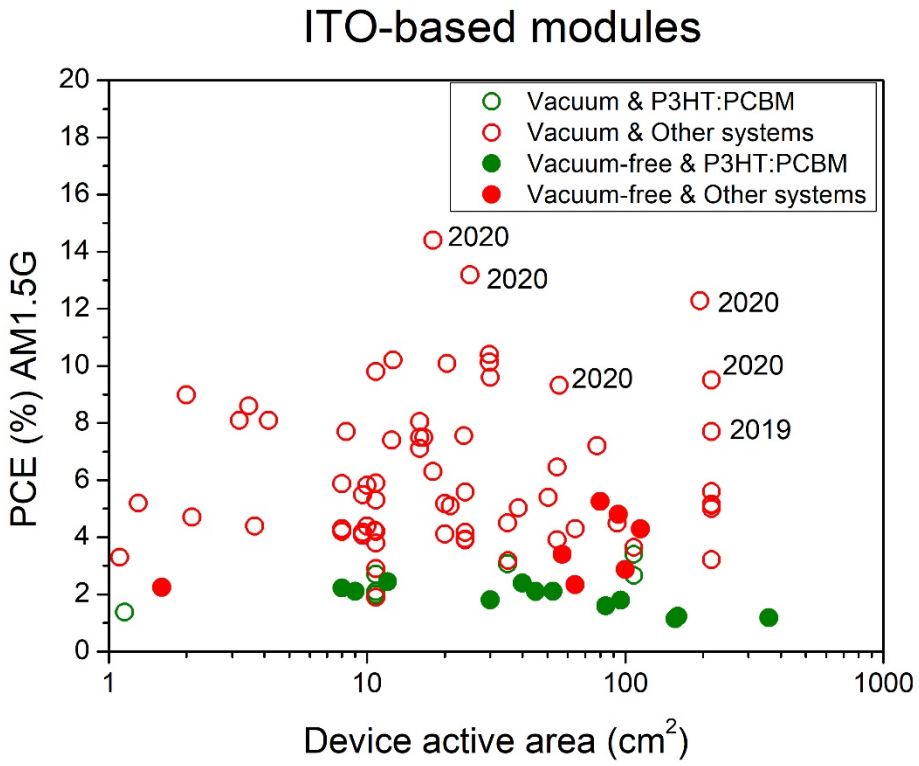

Figure 4. Performance of large area (≥ 1 cm^2) ITO-based OPV modules under AM 1.5G conditions. As shown, the most efficient modules have been reported very recently.

Due to several technological issues, enlarging the area of single cells to increase the maximum output power is not always the best solution. Inhomogeneities in the active layer may degrade device performance, and these effects scale with the area of the cell. Furthermore, and more importantly, the limited conductivity of electrodes such as ITO makes it difficult to extract the large photocurrents generated in large area single cells. A common technique used to overcome the limited conductivity of the transparent front contact consists in connecting several narrow single cells in series. Assuming that in a

module all the *i* cells connected in series behave identically, then the total photo-generated current J_{SC}(Module) equals the $J_{SC}(i)$ of each individual cell, i.e. J_{SC}(Module) = $J_{SC}(i)$. On the other hand, V_{OC}(Module) = Σ $V_{OC}(i)$. Therefore, this series connection strategy is typically preferred as it ensure that the photocurrent produced by the module remains limited (reducing resistive power losses), while the voltage increases linearly with the number of cells (Figure 5).

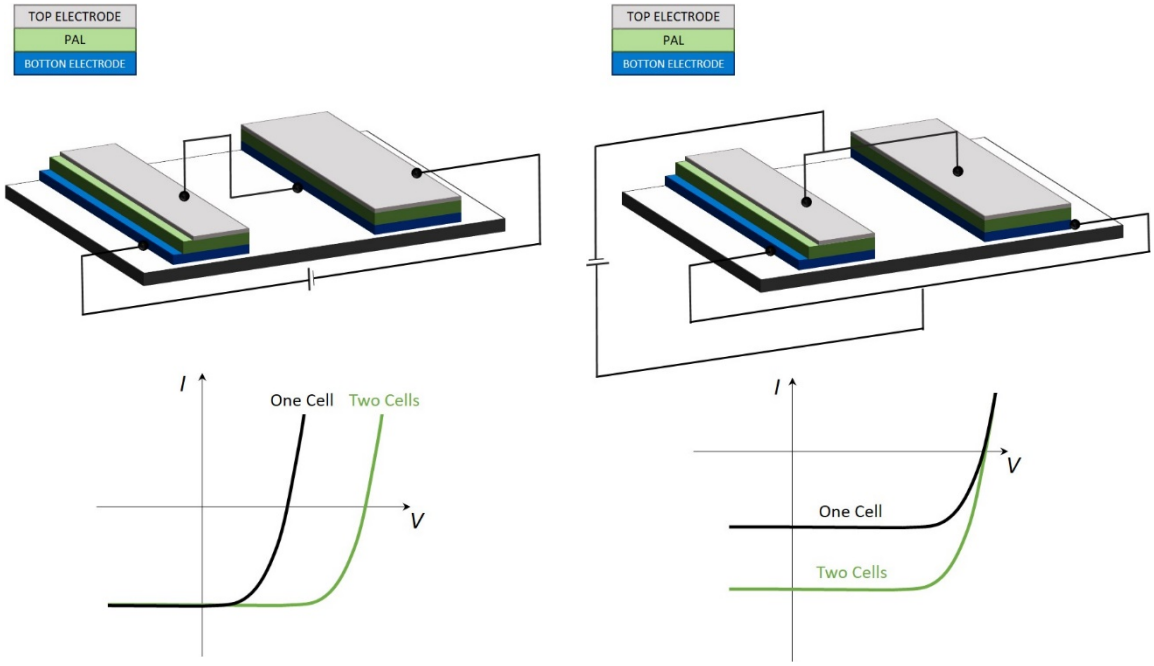

Figure 5. Schematic representation of the connection of two identical solar cells and the corresponding IV characteristic curves: (a) series connection; (b) parallel connection.

Although connection in series can be achieved by externally connecting cells that were produced separately (as is commonly done in the silicon photovoltaic industry), producing integrated monolithic OPV modules is far more attractive from a manufacturing perspective. In a monolithic connection, all the different layers are processed on one substrate and patterned in such a way that the different cells become interconnected in series, i.e. the bottom electrode of one cell is directly connected to the top electrode of an adjacent cell. This is shown in Figure 6, where (i) pattern P1 disconnects the individual bottom electrodes of all cells within the module from each other, (ii) pattern P2 removes the material stack between the bottom and top electrodes allowing the formation of a low ohmic contact, and finally (iii) pattern P3 divides the top electrodes between adjacent cells. The area between the P1 and P3 lines is the so-called "dead area" because it does not contribute to energy production. The ratio between the photoactive area and the total area of the module is referred to as the geometric fill factor

(GFF). The smaller the dead area, the larger the GFF and the higher the module efficiency. Therefore, lines P1, P2 and P3 should be made as narrow as possible.

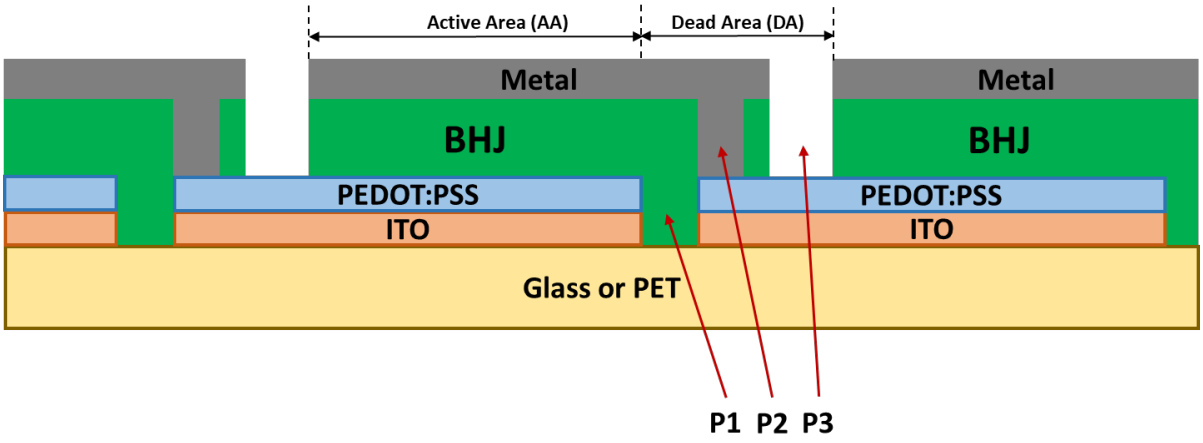

Figure 6. Schematic illustration of an OPV module with lines P1, P2 and P3.

Common coating and printing techniques (like blade-coating, slot-die coating, screen printing, inkjet printing, gravure printing and spray coating) can produce patterns making interconnections between single cells within a module by depositing the bottom electrode, the PAL, and the top electrode as one-dimensional stripes which are slightly offset with respect to each other. However, the relatively low resolution of these deposition techniques requires typical scribe widths ≥ 1 mm to prevent intermixing between inks applied to adjacent cells. This limits the achievable GFF to values typically below 85 %. An alternative approach consists in creating lines P1 - P3 by laser ablation which allows a much higher-precision (reproducible scribe width in the range 20 – 100 µm depending on the laser system), high-throughput and mask-free patterning process. Laser ablation employs a focused laser beam to selectively ablate materials from a surface [111-114]. When processing the different OPV layers, different wavelength and pulse duration are selected to reach different pulse energies which can melt and evaporate the processed layer without damaging the underlying layer. By minimizing the inactive areas used to interconnecting the individual solar cells in series within the module, a GFF of over 95 % can be achieved.

For a module with a given total area, increasing the number of cells within the module leads to an increase in the number of interconnects (number of cells − 1) which leads to a decrease in the GFF and a decrease in the overall module efficiency. On the other hand, decreasing the number of cells leads to an increase in cell width and in resistance losses

due to the limited conductivity of the electrodes (especially ITO). Therefore, the optimum number of cells for a given area results from a balance of these two contradictory effects [115] and can be simulated as described by Lucera et al. [116].

2.2.1. With vacuum conditions

In 2007, Frederik Krebs at the Denmark Technical University (DTU) [117] published one of the earliest reports of an OPV module. This consisted of 91 individual cells, each with an active area of 2.4 × 3.0 cm^2, connected in series and parallel, making up a total active area of 655 cm^2 displaying, however, a very low PCE of 0.0002 %.

Later, in 2009, Tipnis et al. [118] reported on the use of laser ablation to pattern OPV modules of connected cells and since then, the use of lasers for the patterning OPV modules has been the subject of intensive research [119-125].

In 2013, Brabec and co-workers [119], used an ultrafast fs-laser ablation system, with a pulse duration of <350 fs at repetition rates up to 960 kHz, to pattern OPV modules based on the structure ITO/AZO/P3HT:PCBM/PEDOT:PSS/Ag. Here a GFF > 90 % was achieved with the module consisting of 10 monolithically interconnected stripe cells, each with width of 1.0 mm. The best modules with an active area of 1.15 cm^2, had a total interconnection width of 178 µm and a GFF of 83 % and attained a PCE of 1.38 %. The same laser system was later used by the group to; i) extend this concept to tandem P3HT-based modules with 10-cells and a device area of 1.1 cm^2 achieving a GFF of ~85 % and a PCE of 3.3 % [120]; ii) produce P3HT-based modules consisting of 14 cells in series, with a total area of 35 cm^2 achieving a GFF > 95 % and a PCE of 3.07 % [121] and iii) produce modules with GFF of 98.5 % consisting of 14 cells connected in series with a total active area of 35 cm^2 and a total interconnection width below 100 µm. These were based on a PAL blend of PBTZT-stat-BDTT-8:$PC_{61}BM$ and achieved maximum PCEs of 4.2 % and 5.3 % respectively on polyethylene-terephthalate/ITO-Metal-ITO (PET/IMI) and on glass/fluorine-doped tin oxide (FTO) substrates [122].

A ps-laser ablation system, with a pulse duration of 6 ps, at repetition rates of 50 kHz for ITO and 400 kHz was used by Röttinger et al. [124] to pattern both metal and organic layers. This produced modules consisting of six stripes that were based on the PAL blend HDR14:C_{60}. A GFF of 94 % and a PCE of 4.3 % were achieved for an aperture area of 64 cm^2.

Very recently, a ns-laser ablation system with a pulse duration of 20 ns was used by Distler et al. [125] to produce modules from the cell structure glass/ITO/ZnO/PM6:Y6:$PC_{61}BM$/MoOx/Ag having a GFF > 95 %. By carefully tuning the laser ablation parameters combined with a modification of the standard patterning sequence (the P2 patterning was divided in two separate steps P2a and P2b) and an optimization of the active cell width (see Figure 7), the authors were able to produce; i) modules of 12 cells in series with total/active areas of 26.2/25.0 cm^2 and total area PCE of 12.6 % and ii) larger modules of 33 cells with total/active areas of 204.0/194.8 cm^2 and total area PCE of 11.7 %. These values currently represent world record energy efficiencies. The authors demonstrated that the required quality and reproducibility of laser patterning can be achieved with ns-lasers, rather than fs-lasers, thus reducing significantly the investment cost.

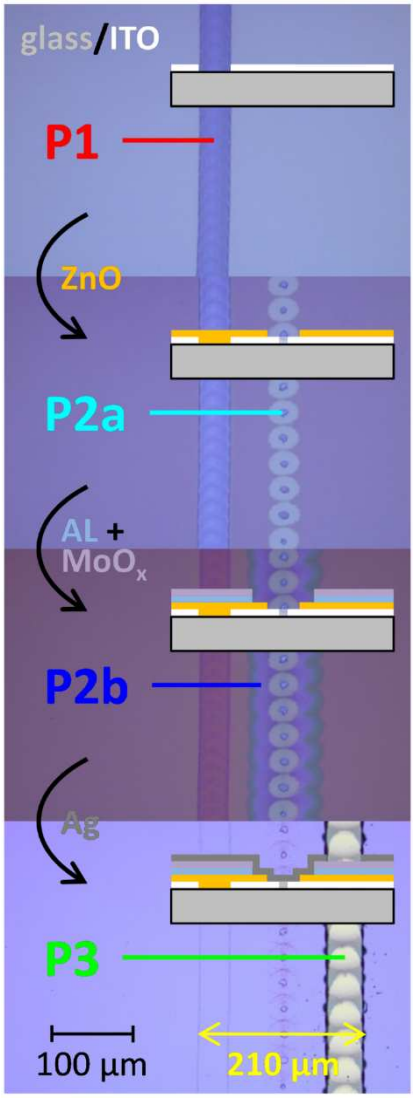

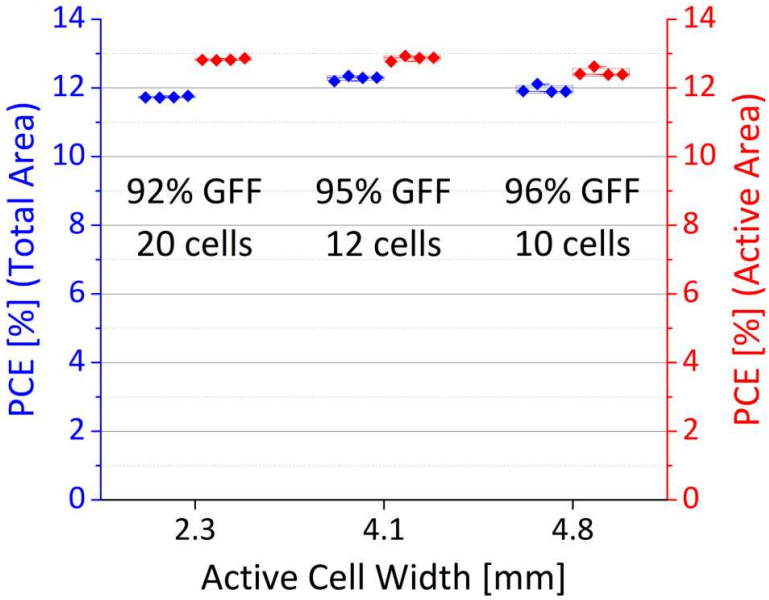

Figure 7. (a) Bright-field microscope images of all laser lines involved in the module production process, namely, P1, P2a, P2b, and P3, together with cross-section sketches of the layer stack after each laser patterning step. The black arrows indicate the different coating steps, that is, electron transport layer (ZnO), active layer (AL: PM6:Y6: PC60BM), hole transport layer (MoOx), and top electrode (Ag); (b) Power conversion efficiencies (PCE) with respect to the total area (blue data, left y-axis) and the active area (red data, right axis) of modules comprising three different layouts (four modules each layout). The layout variation consists in different cell widths (see x-axis), a different number of cells connected in series, and different geometric fill factors (GFF). The total area of all modules is 26.2 cm^2. (Reproduced with permission from Ref. [125]).

Alternative techniques for OPV patterning (i.e. not involving the use of lasers) have also been investigated. These included; i) a chemical-based patterning process achieved by printing thin lines of a fluoro-surfactant to repel the subsequently deposited PAL layer [126, 127] and ii) a mechanical scribing processes [127, 128]. However, the GFF demonstrated was low.

Different module architectures and interfacial layers have also been explored in an attempt to increase the overall efficiencies [96, 129-131]. Lee et al. [129] proposed a new architecture that avoids P2 patterning during the module production. In this architecture, the cells are connected in series with alternating conventional and inverted configurations using self-aligned dual charge-selecting interfacial layers. A module based on PCDTBT:$PC_{71}BM$ was demonstrated having an active area of 10.68 cm^2, a high GFF of 96 % and a PCE of 4.24%.

To reduce the resistive contribution from ITO, Xiao et al. [96] used a metal bus bar sub-electrode around 95 % of the cell perimeter for each cell, which had an active area of 1 cm^2. Cells were then connected in series to form columns of 5 cells, while 5 columns were connected in parallel to form a module with a total active area of 25 cm^2 and an average PCE of 6.5 %.

Hong et al. [130] demonstrated a new module architecture without patterning the electron transport layer (ETL) and hole transport layer (HTL). The inverted structure device ITO/ZnO/PAL/MoO_3/Ag consisted of patterned ITO, a stripe-patterned PAL (PTB7-Th:$PC_{71}BM$) and single-layers of ZnO and MoO_3 without any patterning. A module PCE of 7.5 % was demonstrated with area of 4.15 cm^2 and a GFF of 90 %.

Dong et al. [131] doped a ZnO CIL with the naphthalene-diimide based derivative NDI-PFNBr, which improved the PCE of the corresponding devices. Modules with active areas of 16 cm^2 (4 cells) and 93 cm^2 (13 cells), based onm the structure glass/ITO/NDI-

PFNBr@ZnO/PTB7-Th:$PC_{71}BM$/MoO_3/Ag achieved PCEs of 8.05 % and 4.49 % respectively. Reference modules with a ZnO CIL had an active area of 16 cm^2 and achieved a PCE of 7.11 %.

Research of scalable deposition techniques to produce large area modules has also been the focus of much interest. Among the techniques that have been considered include blade-coating [132-141], slot-die coating [65, 66, 69, 142-146], spray-coating [75], reverse gravure coating [147], Maobi coating [37, 148] and water transfer printing [149].

Blade coating of large area modules has received special attention by Meng and co-workers [132-137]. Blade coating with uniform blade acceleration, instead of uniform blade speed, was used to create a more homogeneous film morphology and uniform film thickness [132]. The active layers were patterned manually using a knife edge and a metal interconnection mask as overlay. Modules with a total active area of 108 cm^2 composed of 10 cells connected in series achieved PCEs of 2.66 % and 3.64 % respectively for PALs consisting of P3HT:$PC_{61}BM$ and POD2TDTBT:$PC_{71}BM$ blends. Rapid-drying blade-coating was later used by the same group to optimize the PAL morphology [133]. Blade-coating was explored to produce opaque and semi-transparent modules based on four different PAL blends [134]. The most efficient modules, with an active area of 10.8 cm^2, were obtained with PTB7-Th:$PC_{71}BM$ and achieved PCEs of 5.9 % for opaque and 5.3 % for semi-transparent modules [134]. Blade coating was also used to deposit modules using the PAL (PTB7-Th:$PC_{71}BM$) and a CIL of MSAPBS with an impressive active area of 216 cm^2 demonstrated [135]. Accelerated blade motion was used as before [132] to accurately control the PAL film uniformity over large area and PCEs of 5.63 % and 4.50 % were reported for opaque and semitransparent modules, respectively. Notably, more recently, the same deposition technique was used to produce modules having an active area of 216 cm^2 for devices based on a donor:acceptor blend of NF3000-P:NF3000-N and using a CIL of TASiW-12, with a very impressive PCE of 9.50 % demonstrated [136]. These values are among the highest PCE ever reported for OPVs with an active area > 100 cm^2 [136]. In similar work by the same group, non-halogenated solvents were used to blade-coat PTB7-Th:$PC_{71}BM$ PAL films to produce modules with a total active area of 216 cm^2 (16 cells) and an average PCE of 5.12 % [137]. Non-halogenated solvents were also explored by other groups to blade-coat large area OPV modules [138, 139]. For example Zhang et al. [138] produced 16 cm^2 modules based on a PTB7-Th:$PC_{71}BM$ PAL, that reached a PCE of 7.5 %. Zhao et al. [140] also demonstrated blade-coated modules

with the PAL morphology optimized through a vacuum assisted annealing (VA) method. Modules with 3 cells, based on the PAL blend PBDB-TF:IT-4F, with a total active area of 12.6 cm^2, achieved an impressive PCE of 10.21 %. Blade-coating has also been used in the production of tandem OPV modules [141] with active areas of 1.3 cm^2 (3 cells) and 2.1 cm^2 (5 cells) and with PCEs of 5.2 % and 4.7 % respectively.

Slot-die coating has been studied for the upscaling of OPV devices [65, 66, 69, 142-146]. In 2014, Hong et al. [65] prepared modules based on a P3HT:PCBM PAL, slot-die coated from a CB:DCB mixturs, with an impressive total active area of 198 cm^2 and a PCE of 1.73 % demonstrtated. A mask was used for stripe patterning, and the modules consisted of 3 sub-modules connected in parallel; each sub-module was composed of 11 serially connected cells with 6 cm^2 active area per cell. Heo et al. [143, 144] studied the use of slot-die coating to prepare modules based on blends of $PC_{71}BM$ with the small molecule donors LGC-D023 [144], LGC-D073 [144] and BTR [143]. The most promising modules were based on LGC-D073:$PC_{71}BM$, had a total active area of 24 cm^2 and achieved a PCE of 5.50 % [144]. Modules, with 5 serially connected cells (total active area of 23.7 cm^2, 4.74 cm^2 per cell) were prepared by Chang et al. [145], where three different ETL/HTL combinations were tested, namely ZnO/MoO_3, PEI/MoO_3 and PEI/PEDOT:PSS. The ETL, PAL and HTL were all deposited by slot-die coating under ambient conditions using a stainless steel meniscus guide for stripe patterning, with the Ag top electrode thermally evaporated through a stripe patterned shadow mask. The most promising modules were obtained using the PEI/PEDOT:PSS combination, and achieved a certified PCE of 7.56 %. Lee et al. [146] prepared slot-die coated modules with a total active area of 30 cm^2, consisting of 5 cells connected in series, where the PAL consisted of a ternary blend of PTB7-Th:$PC_{71}BM$:COi8DFIC. Rigid modules including a slot-die-coated PAL achieved a PCE of 8.6 %. Flexible roll-to-roll coated modules fabricated using a commercial machine achieved a PCE of 9.6 %.

The use of spray-coating to produce large area OPV modules has been so far very limited. Zhang et al. [75] reported spray-coated modules based on the system PBTI3T:$PC_{71}BM$, with structures consisting of 6 series-connected single stripe cells (70 mm × 11 mm), each with an active area of 38.5 cm^2 and exhibiting a PCE of 5.27 %.

Other less common scalable deposition techniques have also been tested in the production of large area OPV modules. R2R reverse gravure coating was used by Vak et al. [147] to produce P3HT:PCBM based modules (5 series-connected strip cells) with a total area of

45 cm^2 and a PCE of 2.1 %. Inspired by an old Chinese calligraphy technique, Mao et al. [148] used a motor-driven, computer controlled Maobi coating system to deposit the PAL of large area solar modules (18 cm^2) containing 14 cells connected in series. Modules based on a PAL of PBDB-T:ITIC achieved a PCE of 6.3 %. Maobi coating was also used by the same authors to repair defects in blade-coated modules [37]. Modules based on the same PBDB-T:ITIC PAL system, consisting of 5 cells and a total active area of 21 cm^2 (4.2 cm^2 per cell), achieved a PCE of 5.1 %. Sun et al. [149] demonstrated the use of a water transfer printing method to produce a highly uniform PAL film on an OPV module with a total active area of 3.2 cm^2 and consisting of 4 cells. Modules with a PAL of PBDB-T-2F:IT-4F achieved a PCE of 8.1 %.

The use of novel donors [150-152] and acceptors [153, 154] and novel PAL blends [92, 155, 156], has also been explored by some authors. Badgujar et al. [150] prepared modules with 11 serially connected cells and a total active area of 78.5 cm^2, where the PAL consisted of a blend of $PC_{71}BM$ with newly synthesized oligomer donors based on benzodithiophene (BDT) units. The higher efficiency modules were made with the oligomer BDT2 and achieved a PCE of 7.45 %, due to reduced charge recombination and a well-constructed 3D morphology. Novel synthesized donor polymers TPD-n, n = 1-3 and TPD-3F were used by Liao et al. [152] to fabricate OPV modules with a total active area of 29.75 cm^2, corresponding to a GFF of ~37 %. The most efficient module (Figure 8) was based on TPD-3F:IT-4F and had a certified PCE of 10.08 % over an active area of 20.4 cm^2 as defined by an aperture mask; smaller cells (having an area of 0.04 cm^2). had a PCE of ~13 %. Lee et al. [153] synthesized a novel NFA T2-OEHRH, which was made of asymmetric side chains (octyl and 2-ethylhexyl) and an unfused bithiophene core and used it in OPV modules based on the D-bar-coated ternary PAL PTB7-Th:EH-IDTBR:T2-OEHRH. Modules consisting of 11 stripe cells connected in series, with a total aperture area of 55.5 cm^2 achieved a PCE of 9.32 % [153]. Very recently, Dong et al. [154] synthesized a novel NFA (DTY6) by extending the branched alkyl chains of BTP-4F (also known as Y6) to improve the solvent processing ability and suppress excessive molecular aggregation due to the steric hindrance effect of the long-branched alkyl chains. Modules with a total active area of 18 cm^2 and consisting of six ITO/PEDOT:PSS/PM6:DTY6/PNDIT-F3NBr/Ag cells (each of 5 × 0.6 cm^2) were monolithically connected in series and achieved an impressive PCE of 14.4 % (certified PCE of 13.98 %) [154]. Ternary blends have also been used to increase the efficiency of

OPV modules [92, 153, 156]. Huang et al. [156] prepared modules with 16 cell stripes connected in series (total active area of 216 cm^2) with the structure glass/ITO/PEDOT:PSS/PAL/CIL/Al where the PAL consisted of a ternary blend of PBDB-T:ITIC:$PC_{71}BM$, with different cathode interfacial layers used. Here, modules with a ZrOx cathode interfacial layer achieved an impressive (considering their large area) PCE of 7.7 %.

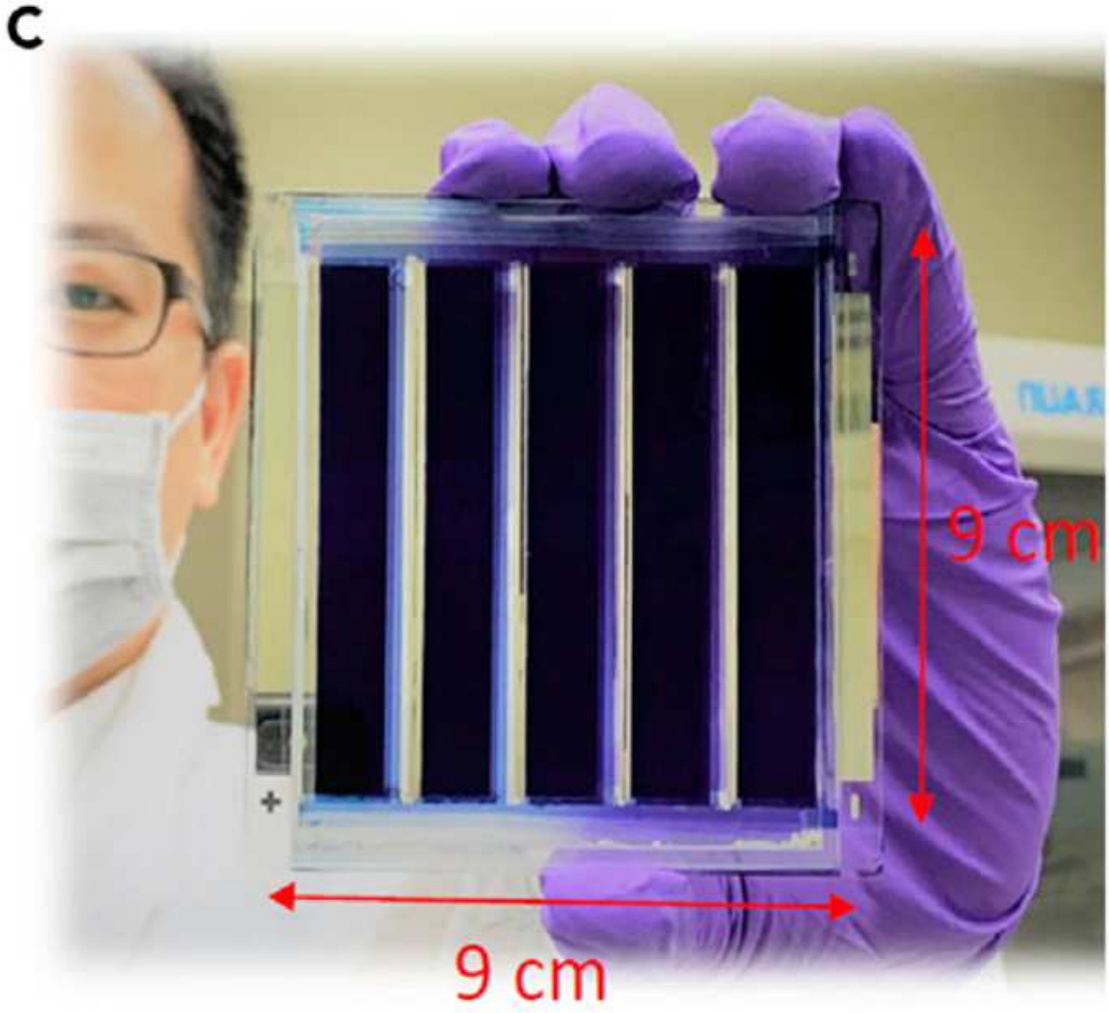

Figure 8. Photograph of a TPD-3F based OPV module (reproduced with permission from ref. [152]).

ITO-based OPV modules have also been investigated for indoor applications [157-161]. Devices based on P3HT, PCDTBT, and PTB7 blended with $PC_{71}BM$ were tested by Lee et al. [157]. PCDTBT-based devices achieved the highest PCE under a fluorescent lamp (300 lux), in contrast to AM 1.5G conditions where the PTB7-based devices performed

the best. A PCDTBT-based module with a total active area of 100 cm^2 delivered, under a 300 lux fluorescent lamp, a PCE of 11.2 % corresponding to a maximum power of 9.38 $\mu W \cdot cm^{-2}$. Modules (8 cells) based on a proprietary formulation, with an active area of 3.67 cm^2 achieved an output power of 43.4 $\mu W \cdot cm^{-2}$ as reported by Aoki et al. [158]. OPV modules consisting of 6 cells connected in series with a total active area of 9.5 cm^2 (1.6 cm^2 per cell) were prepared by Arai et al. [159] on glass and PET substrates using a PAL of BDT-2T-ID:PNP. Under a white LED illumination at 200 lux, the module (on a glass substrate) achieved an output power of 11.7 $\mu W \cdot cm^{-2}$, corresponding to a PCE ≈ 15 %, and the module on PET achieved an output power of 10.6 $\mu W \cdot cm^{-2}$. In related work, the same authors [160] studied similar OPV modules based on the PAL system 1DTP-ID:PNP, which could generate a power of 95.4 μW under a lamp producing 200 lux, corresponding to a PCE of ~17 % and a V_{OC} = 4.05 V. More recently, Park et al. [161] tested a novel polymer donor (PBDB-TSCl), blended with the NFA IT-4F in OPV modules with a total active area of 58.5 cm^2 composed of 10-stripe cells connected in series with the complete structure being glass/ITO/ZnO/PBDB-TSCl:IT-4F/MoOx/Ag. These modules demonstrated a PCE of 12.42 % under 1000 lux; a value much greater than the PCE of 6.53 % produced by reference modules based on PBDB-TF.

2.2.2. Vacuum-free (Evaporation-free) conditions

Some of the earliest (2009 and 2010) reports of OPV modules processed without vacuum deposition steps (except for the sputtered ITO substrate), were made by Krebs and co-workers [115, 162-164]. In 2009, these authors introduced one of the first industrial manufacturing processes in an ambient atmosphere (known as *ProcessOne*) that was used to create flexible ITO-based OPV modules [163]. *ProcessOne* uses a roll of PET substrate with a sputtered ITO layer and involves several steps, including the deposition by screen printing of a silver back electrode under ambient conditions. *ProcesseOne* modules with areas up to 360 cm^2 were reported by the DTU group in 2010 [115], but the corresponding PCEs were low (< 2 %).

After these early vacuum-free studies, several others have addressed the upscaling of OPV modules using vacuum-free processing [103, 107, 147, 165-177] with strategies used to deposit the top electrodes including spray coating [165, 172], screen-printing [103, 147, 166, 170, 176], rotary screen printing [169, 174], inkjet printing [166, 173], blade-coating [107, 167, 175, 177] and gravure printing [168]. However, despite all these

studies, only a few reported modules displayed PCEs close to or higher than 5.0 % [171, 175, 176].

In 2016, Berny et al. [103] reported modules, produced under ambient conditions, based on a PBTZT-stat-BDTT-8:$PC_{61}BM$ PAL blend with screen-printed top Ag-grid electrodes. Modules composed of 9 serially connected cells patterned using a high precision laser, had a total active area of 114.5 cm^2 and a GFF of 95 %. These devices displayed an average PCE of 4.3 % and were assembled in solar trees at the Milan Expo in 2015, as illustrated in Figure 9.

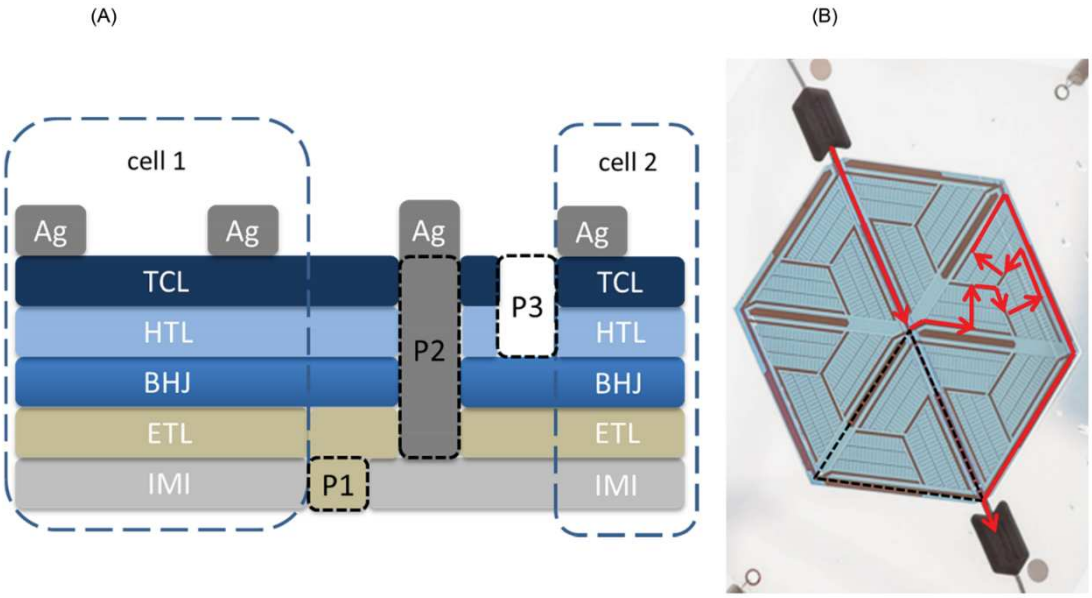

(C)

Figure 9. (A) Schematic of the module layout. The interconnect P2 is made by laser scribing. The distance between two cells (beginning of P1 to end of P3) is 1 mm; (B) Close-up of a small module installed in an EXPO tree. One of the small modules consists of six submodules, each in a triangular shape (dashed line), which are all connected in parallel. One triangular module is made of nine cells, all connected in series. The red arrow symbolizes the current pathway for one distinct triangular submodule from the anode to the cathode; (C) large scale deployment of OPV modules in solar trees at the Milan Expo 2015. (Reproduced with permission from ref. [103]).

Laser patterning (fs) was used by Lucera et al. [171] to produce, semi-transparent blade-coated modules (on rigid glass/FTO) and slot-die coated modules (on flexible PET/IMI), based on a PBTZT-stat-BDTT-8:$PC_{61}BM$ PAL. The flexible PET/IMI-based modules consisted of 19 individual cells, with a total active area of 68.76 cm^2 (3.61 cm^2 per cell) and achieved a PCE of 4.3%. The rigid glass/FTO-based modules consisted of 30 individual cells, with a total active area of 197.40 cm^2 (6.58 cm^2 per cell) and reached a PCE of 4.8 %. Glass-based modules, with GFF > 94 % and transparency > 10 %, were demonstrated in a BIPV insulating glass window.

Fully blade-coated modules, including AgNW top electrodes and consisted of 12 individual cells monolithically connected in series with a total area of 64.0 cm^2 were developed by Strohm et al. [175]. As a PAL, two donor:acceptor combinations were explored (P3HT:PCBM and P3HT:IDTBR) and for modules based on the IDTBR acceptor, both halogenated and non-halogenated solvents were used for the PAL

deposition. Laser patterning allowed monolithic interconnection of cells, producing narrow interconnect areas with high precision and good reproducibility, achieving GFF values of ~93 % for all modules (total active area of 59.52 cm^2). PCBM-based modules delivered a maximum PCE of 2.4 % and IDTBR-based modules delivered maximum PCEs of 5.0 % and 4.7 % when processed from CB and from o-methylanisole (oMA) respectively.

Han et al. [176] fabricated inverted structure ITO/ZnO/PAL/HTLs/Ag OPV modules by *ProcessOne*, with devices incorporating screen-printed top Ag electrodes. Modules using bilayer HTLs (WO_3/HTL) with 10 cells connected in series and having a total active area of 80 cm^2 achieved an impressive PCE of 5.25 %.

3. Upscaling of ITO-free cells and modules

OPVs have evolved around ITO as the front electrode, because of its high transparency, low sheet resistance (8–12 $\Omega \cdot \square^{-1}$ on glass substrates) and industry proven reliability. However, ITO presents several problems:

i) ITO is expensive due to the scarcity of indium and due to the vacuum sputtering processing needed in its preparation. Some life cycle analysis studies have concluded that ITO has a substantially negative impact on the EPBT of OPVs [178-182];

ii) ITO is brittle and not suitable for highly flexible substrates;

iii) ITO processing, especially at higher conductivity, requires high temperature annealing, which is incompatible with plastic-based flexible substrates, such as polyethylene naphthalate (PEN) and polyethylene terephthalate (PET).

iv) ITO has a relatively high sheet resistance (typically > 40 $\Omega \cdot \square^{-1}$ on plastic substrates and > 8 $\Omega \cdot \square^{-1}$ on glass substrates) which is problematic when fabricating large-area OPVs.

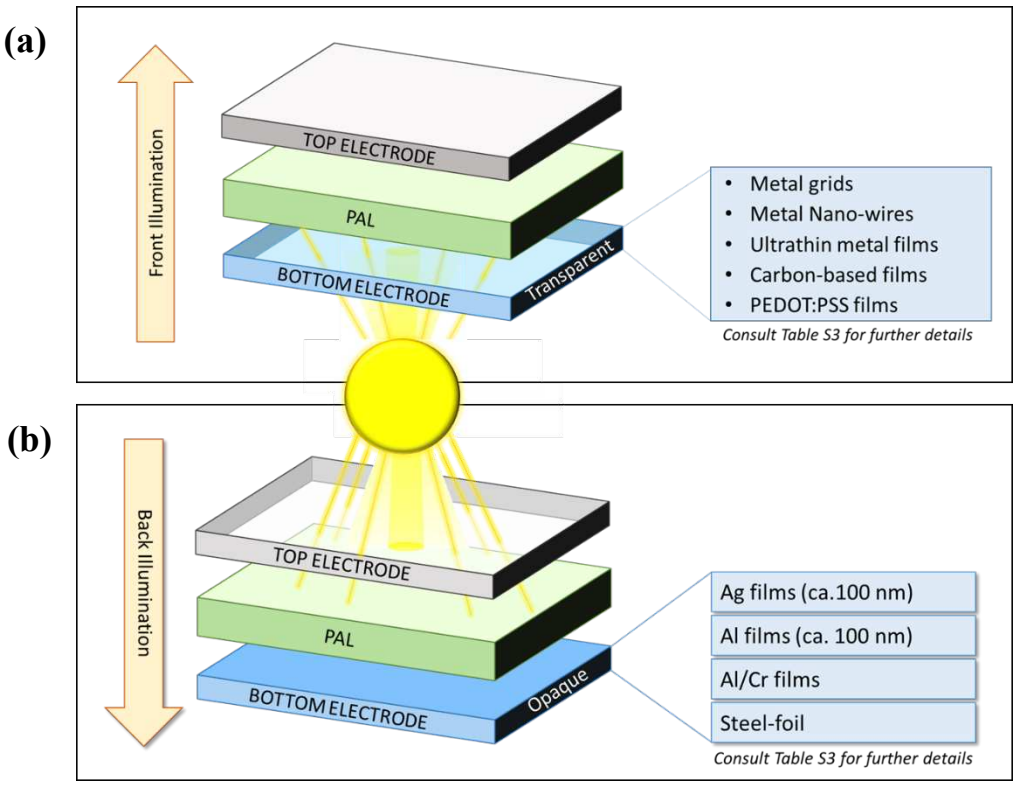

Figure 10. (a) Transparent bottom electrodes with front illumination; (b) Opaque bottom electrodes with back illumination.

All these shortcomings make the replacement of ITO an important and desirable goal on the pathway to commercially and technically viable OPVs [183-185]. Several strategies have been followed to replace the ITO bottom electrodes either with other transparent conducting electrodes (TCEs) or with opaque electrodes (back illumination). These strategies are summarized in Figure 10 and include the use of current collecting metal grids, metal nanowires, ultrathin metal films, carbon-based electrodes and conducting polymer based electrodes as transparent electrodes, as well as the use of thick metal films as opaque electrodes. Although some recent literature reviews have addressed work to develop ITO-free OPVs [186-190], their focus was not on large area cells and modules.

The most relevant ITO-free large area OPV cells and modules are described along this section and their performances are indicated in Table S3 and represented in Figure 11.

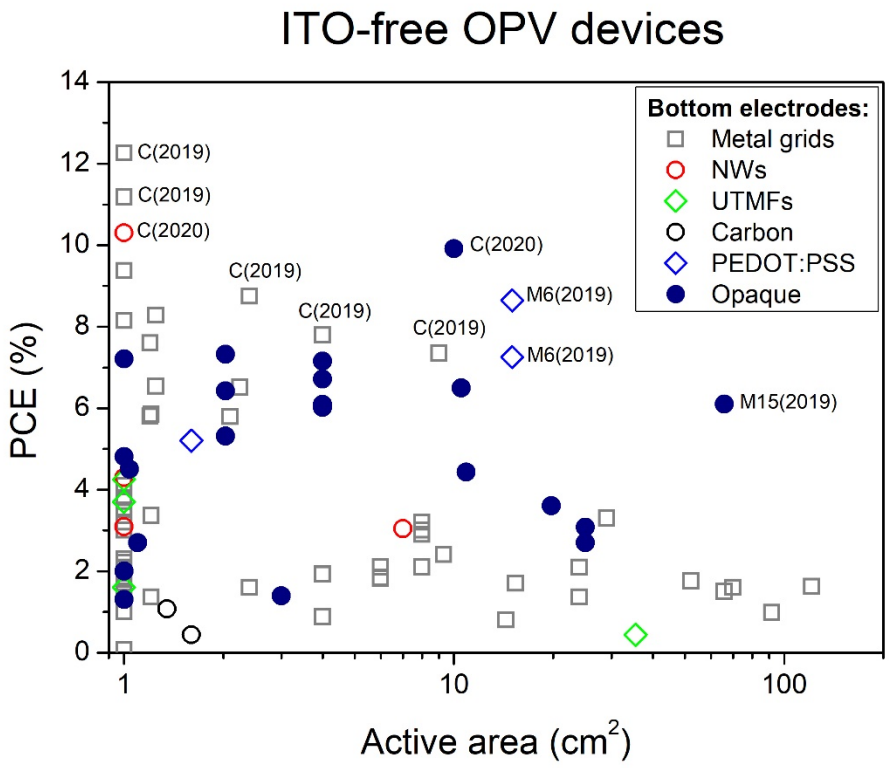

Figure 11. Performance of large area (≥ 1 cm^2) ITO-free devices, cells (C) and modules (Mx, where x is the number of cells), under AM 1.5G conditions. The most promising devices have been reported very recently, as indicated inside brackets.

3.1. Upscaling using metal-based TCEs as bottom (front) electrodes

Metal-based TCEs, have been extensively investigated as potential substitutes for ITO in OPV devices and some reviews on this topic have been published [191, 192], although these were not focused on large area OPVs. Silver (Ag), copper (Cu) and gold (Au) are (in this order), the most highly conductive metals and their use in metal-based TCEs for large area OPV cells and modules has been extensively explored in different forms, including as current collecting metal grids, ultrathin metal films, metal nanowires among others, and is reviewed in this sub-section.

3.1.1. Metal grids (meshes) as transparent bottom electrodes

Metal grids can be either positioned above the substrate or embedded into the substrate. A printed grid, with raised topography above the substrate, has the advantage that it only requires one single printing step. As a disadvantage, these electrodes may suffer from high surface roughness, resulting in the possibility of electrical short-circuits between the TCEs and the top electrode. As a way to attenuate this effect, such grids needs to be very thin, however very thin grids needs a certain width to guarantee a good electrical conductivity which leads to a loss in transparency.

An embedded grid has the advantages of creating both a smooth substrate topography and allowing the use of thicker metal grids with a very high aspect ratio (height/width). This results in grids that both have very high conductivity and optical transparency. The disadvantages of this approach are that grid fabrication requires at least two distinct processing steps (thermal imprinting and filling with metal) and an associated lower production speed.

Metal grids can have different geometries, including circular, linear and hexagonal (honeycomb). The ideal geometry of a current-collecting grid should provide an optimal balance between transparency and conductivity. A higher transparency can be obtained by using thinner lines and a larger pitch size (distance between lines). By contrast, a higher conductivity can be achieved using thicker lines and a smaller pitch size.

In 2005 Cheknane et al. [193] determined the best theoretical compromise between shadowing effects and series resistance effects, caused by a using a metallic grid having a circular geometry. Later, the same author [194] compared circular and linear geometries and concluded that devices with a circular grid should achieve a higher FF and PCE. Similar studies on the best compromise between transparency and conductivity were

performed for linear grids by Tvingstedt et al. [195] and later by Galagan et al. [196]. In practice, linear and honeycomb grids have been far more popular than the circular grids. A honeycomb pattern has an important advantage over a linear pattern, as line breaks have less impact in overall current collection, since charges can be redirected through alternative paths along the grid.

In one of the first reports on the use of metal grids in OPVs, Kang et al. [197] demonstrated the fabrication via a R2R compatible Nano-Imprint Lithography (NIL) technique of nano-patterned metal-grid TCEs composed of Ag, Au and Cu having a thickness of 40 nm. Small cells fabricated using these grids as bottom electrodes achieved a PCE similar to reference ITO-based cells.

Silver, being the most highly conductive metal, has been by far the most studied metal for TCE applications. In 2007, Tvingstedt et al. [195] demonstrated a soft lithographic method for depositing linear grid Ag electrodes. The best theoretical compromise between transparency and conductivity was determined as a function of pitch size. Silver grid-covered substrates were coated with the highly conductive polymer DEG-PEDOT:PSS to reduce surface roughness and associated risk of short circuits. The small cells fabricated achieved a PCE comparable to ITO-based devices.

Frederik Krebs at DTU and his co-workers have been a leading group in the development of high throughput R2R mass-production methods for large area OPV cells and modules. These authors have developed an extensive and important body of work on the R2R upscaling of OPVs based on Ag-grid TCEs. Part of this work focused on the standard P3HT:PCBM PAL system [198-209] and addressed issues such as: (i) printing/deposition of the silver grid bottom (front) electrodes using techniques such as thermal imprinting, inkjet printing, flexographic printing and photonic sintering [198-200]; (ii) the printing of the top (back) electrodes using techniques such as flatbed screen printing, rotary screen printing, inkjet printing and flexographic printing [201-203]; (iii) the fabrication of tandem devices where the entire layer stack was prepared by printing or coating, i.e. without vacuum [204]; (iv) the optimization of the slot-die coated PAL morphology with additives [205] and (v) round-robin inter-laboratory device reproducibility [206].

In 2013, Krebs et al. [208] introduced a new candidate for the replacement of ITO-based substrates; the flextrode. Flextrode substrates, or flextrodes, are made of a highly conducting Ag grid flexographically printed on a PET substrate and have the structure

PET/Ag-grid/PEDOT:PSS/ZnO (see Figure 12). Flextrodes exhibit a sheet resistance of ~ 10 $\Omega \cdot \square^{-1}$ and an optical transmittance over the visible region of ~60 %, with their electrical and optical properties being studied in detail [210]. Since their introduction, flextrodes have been used by Krebs and co-workers in a large number of upscaling studies and currently, flextrodes are commercialized by the company InfinityPV, a spin-off from DTU [211].

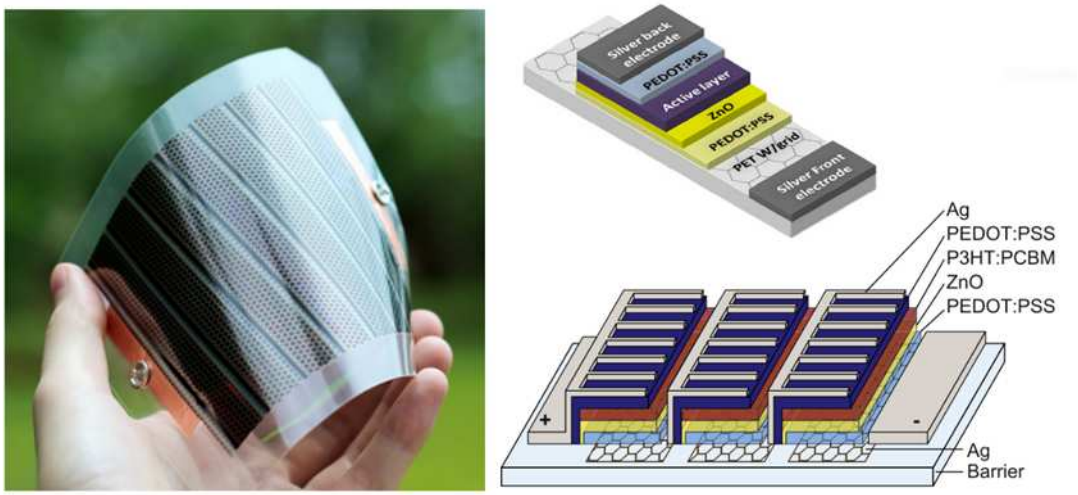

Figure 12. Examples of Flextrode-based OPV devices (re-adapted with permission from refs. [201, 207]).

Using a flextrode bottom electrode and on screen printed top Ag-grid electrodes, Krebs et al. [207] described the all-solution processing of ITO-free OPV modules, and named this process as *IOne*, as opposed to the ITO-based *ProcessOne* as described in Section 2.

Krebs and co-workers have also applied high throughput R2R mass-production methods to fabricate OPV devices based on PAL systems other than the classical P3HT:PCBM [209, 212-221] and addressed issues such as: (i) use of new polymer donors [209, 212-216] and new small molecule donors [217] with PCBM; (ii) testing of fullerene-free systems [218, 219]; (iii) PAL morphology optimization with additives [220] and (iv) tandem devices [214, 221].

Upscaling work on ITO-free OPV devices based on Ag-grid bottom electrodes has also been explored by other groups [78, 92, 101, 222-231], either using a P3HT:PCBM PAL [78, 222-225] or other PALs [78, 92, 101, 225-231]. Most of this work focused on the optimization of the Ag-grid electrodes including grid geometry (honeycomb, linear)

[222], the height and width of grid lines and busbars [223], grid pitch [228] and the properties of PEDOT [224, 229]. Other work was more focused on the use of new PALs in Ag-grid based OPVs [92, 230, 231], including fullerene-free systems [231].

Jin et al. [228] prepared fully printed Ag-grid/PEDOT:PSS TCEs with different grid pitches (GP = 1, 2 and 4 mm). All these TCEs exhibited a high optical transmittance (T_{550nm} ~ 90 %), low surface roughness (rmsr ~1 nm), high flexibility (bending radius of ~1 mm) with R_{sheet} varying between ~4 $\Omega \cdot \square^{-1}$ (GP = 1 mm) and ~20 $\Omega \cdot \square^{-1}$ (GP = 4 mm). Flexible OPVs based on TCE-GP of 1 mm with an active area of 2.10 cm^2 and based on a PTB7:$PC_{71}BM$ PAL, exhibited a relatively high PCE of 5.79 %; a value higher than reference devices with same size based on ITO (3.85 %) [228]. Lu et al used the additives 5 % DMSO and 0.1% fluoro-surfactant Capstone® FS-31, v/v [229] to improve the conductivity and the wettability of PEDOT:PSS on a PET substrate. Devices based on a PTB7-Th:$PC_{71}BM$ PAL with active area of 2.25 cm^2 and with different Ag patterns exhibited very similar PCEs (max of 6.51 %) suggesting that it is the cover ratio rather than the shape of the patterns that has stronger influence on device performance. Zhang et al. [92] reported cells with Ag-grid bottom electrodes and a ternary PAL blend of PTB7-Th:*p*-DTS($FBTTH_2$)$_2$):$PC_{71}BM$, with active area of 1.25 cm^2 and achieved an impressive PCE of 8.28 %. This is one of the highest efficiencies reported so far for OPV devices based on Ag-grid bottom electrodes with an active area ≥ 1 cm^2. OPV cells based on the ternary PAL blend PAL PffBT4T-2OD:$PC_{61}BM$:$PC_{71}BM$, with active area ~1.2 cm^2 and the structure PET/Ag-mesh/PEDOT:PSS/ZnO/PAL/top-electrode were reported by Czolk et al. [101]. Here, a mixture of AgNWs:PEDOT:PSS and evaporated MoOx/Ag were tested as top electrodes with corresponding average PCEs reported of 5.8 % and 7.6 % respectively. Helgesen et al. [230] (2015) upscaled the synthesis of the polymer PBDTTTz-4 from milligram to gram scale by applying continuous flow synthesis. This was then blended with PCBM and used in roll coated cells and modules with Ag-grid/PEDOT:PSS bottom electrodes. Modules, consisting of 16 cells connected in series with a total active area of 29 cm^2 exhibited an average PCE of 3.3 % [230]. Fan et al. [231] reported fullerene-free cells based on a PAL of PM6:IDIC and with Ag-grid bottom electrodes. Devices with an active area of 1.25 cm^2 exhibited a PCE of 6.54 %.

OPV studies based on TCEs with other metal grids, such as Cu grids or multi-metal grids are much rarer. However TCEs based on Cu meshes have been studied due to their very low cost. For instance, copper nanoparticle inks have been reported as being six times

cheaper than Ag nanoparticle inks, and this could further reduce the fabrication cost of OPV devices. Cu is well suited for OPV applications due to its much lower cost and similar work function to ITO (ca. 4.7 eV). Although Cu grids have been tested in small area (< 1 cm^2) OPVs [232-234], no reports are known of its application in larger areas (> 1 cm^2).

Multi-metal grids have been also explored [235-238]. Choi et al. [235] developed embedded Cu/Au metal grids consisting of an Au grid-layer on top of an electroplated copper grid-layer on a flexible SU8 polymer substrate. Using this, OPVs cells based on a P3HT:ICBA PAL with an active area of 9.3 cm^2 exhibited a PCE of ~ 2.4 %.

Sputtered tri-layer Mo/Al/Mo (MAM) grids have been explored as bottom TCEs in large area OPV devices [236, 237]. Galagan et al. [236] studied the relationship between the resistance of MAM grids, the size of the OPV cells (active areas from 2.4 to 14.4 cm^2) and their PCE using P3HT:PCBM based devices. Here, an observed PCE drop (1.6 % to 0.8 %) was observed when scaling up devices from 2.4 to 14.4 cm^2 and was found to depend both on the metal-grid sheet resistance (R_S) and on the light intensity. Interestingly, for a R_S of 9.64 $\Omega \cdot \square^{-1}$, a PCE drop of 75 % was found at 1 Sun illumination, with this reducing to only 25 % at 0.13 Sun, indicating that for indoor applications, scaling up the OPV cell dimensions has a much less effect on PCE. Mo/Al/Mo metal grids have also been used by Eggenhuisen et al. [237] to produce modules with a total active area of 92 cm^2. However, these modules achieved a very low PCE of 0.98 %.

More recently, Han et al. [238] reported Ag/Cu grid TCEs having a honeycomb structure and very low sheet resistance <1 $\Omega \cdot \square^{-1}$ with high average transparency (84 %). The grids developed were 3 μm in width and 3 μm in depth and were almost completely embedded in the PET substrate and only covered ~3% of the substrate (see Figure 13). Such grids were surface planarized using highly conductive PEDOT:PSS (E100) and then tested in large area OPV cells. The highest efficiency cells, (having an active area of 1.0 cm^2) utilised a PAL of NF3000-P:NF3000-N and a CIL of ZnO/zirconium-acetylacetonate (ZrAcac) and achieved a very impressive PCE of 12.26 % (certificated PCE of 11.45%). This is currently a performance record for large area ITO-free devices. Such TCEs were also tested in larger area devices with an impressive PCE of 8.75, 7.79 and 7.35 % attained for active areas of 2.4, 4 and 9 cm^2 respectively.

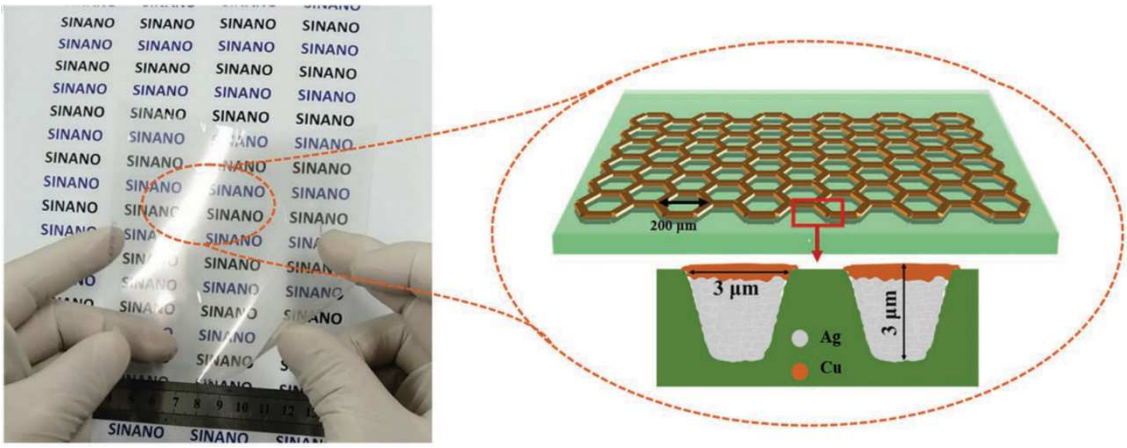

Figure 13. Photograph and schematic of a large-area PET/Ag/Cu electrode (reprinted with permission from ref. [238]).

3.1.2. Metal nanowires as transparent bottom electrodes

Metal nanowires (NWs), and particularly silver and copper nanowires (AgNWs and CuNWs), have been investigated as promising alternatives for ITO-based electrodes. TCEs based on AgNWs that were around 8.7 µm long and 100 nm diameter, were first demonstrated in 2008, in a seminal work by Peumans and co-workers [239], and their scalability has been demonstrated by the same authors in 2010 [240]. Since then, a significant number of studies have addressed the use of transparent AgNWs-based bottom electrodes in OPVs, although the majority of these studies were limited to small area devices (< 1 cm^2) [241-246] and are the subject of previous reviews [191, 247, 248]. The reports of large area OPVs based on AgNWs bottom electrodes are still very scarce in literature [102, 249-252].

The DTU group [249] rotary screen printed AgNW-based TCEs covered with ZnO, displaying a transmittance ≈ 84% over the spectral range 550-800 nm and had a R_S of 10-20 $\Omega \cdot \square^{-1}$. OPV cells based on these bottom TCEs with active area of 1.0 cm^2 and structure PET/AgNW/ZnO/PAL/PEDOT:PSS/Ag-grid were fabricated using different polymer:PCBM PALs. The highest efficiency devices were based on a PAL blend of PBDTTTz-4:PCBM and achieved a PCE of 3.30 % [249]. Fully inkjet printed OPV cells, with AgNW bottom and top electrodes and with active area of 1.0 cm^2 were demonstrated by Maisch et al. [250] who achieved a PCE of 4.3 % based on a PV2000:PC_{71}BM PAL. Zhao et al. [102] used AgNW-based TCEs, deposited on PET substrates using slot-die printing to produce OPV cells having the structure PET/AgNWs/ZnO/PAL/MoOx/Ag

with an active area of 7 cm^2, where the PAL was a PPDT2FBT:$PC_{71}BM$ blend. These cells achieved a PCE of 3.04 % when the PAL was coated on substrate at 40 °C. Very recently, Sun et al. [252] reported all-solution processed OPV cells with the structure AgNWs@PI/ZnO/PBDB-T-2F:IDIC:Y6/HXMoO3/PEDOT:PSS/AgNWs having an active area of 1.0 cm^2 which reached a PCE of 10.3 %. This represents one of the highest efficiencies ever reported for OPV devices based on AgNWs bottom electrodes.

Although AgNW-based bottom electrodes exhibit a good balance between conductivity and transmittance and are amenable to R2R processing, some stability issues have been reported. The electrical conductivity of AgNWs degrades under simultaneous presence of high humidity and high temperature [253], under electrical stress [253, 254] and under UV-light exposure [255]. Another disadvantage of AgNWs lies in the occurrence of short circuits (shunting) due to inter-electrode penetration [241].

Despite several reports on the application of copper nanowires (CuNWs) in TCEs [256, 257], the few literature studies that report their use as bottom electrodes in OPVs are limited to small area devices [258, 259]. No literature studies are known on large area (≥ 1 cm^2) OPV devices with CuNW-based electrodes.

3.1.3. Ultrathin metal films (UTMFs) as transparent bottom electrodes

Ultrathin metal films (UTMFs) are continuous metallic films, typically with thickness < 10 nm, that have a high transmittance and exhibit a low sheet resistance. UTMFs possess high compatibility with organic semiconductor materials and are very flexible due to their low thickness and high mechanical ductility. UTMFs are scalable to large areas and, compared to metallic grids, have the advantage that they do not require any patterning processes. However, the growth of UTMFs follows the Volmer–Weber mechanism, resulting in a rough and discontinuous morphology with poor optoelectronic properties due to poor adhesion to substrates. Different strategies have been developed for preparing ultra-smooth UTMFs with superior transmittance and conductivity by successfully suppressing the Volmer–Weber mechanism. Addressing these strategies is outside the scope of this review and interested readers are referred to a recent comprehensive review on this topic [260].

In 2012, the DTU group [261] demonstrated fully solution processed semi-transparent Ag-based UTMF electrodes (thickness < 20 nm) spin-coated on flexible PET substrates from diluted Ag-inks. These electrodes had a sheet resistance as low as 5 $\Omega \cdot \square^{-1}$ and

transmittance of ~30 % at 550 nm and were tested in OPVs devices based on a P3HT:PCBM PAL. Devices with an active area of 1 cm^2 and R2R processed modules with an active area of 35.5 cm^2 exhibited PCEs of ~ 1.6 % and ~ 0.44 % respectively [261]. Stec et al. [262] produced 8 nm thick Cu, Ag, Au, and Cu/Ag UTMF bilayer electrodes on flexible chemically surface modified PET and PEN substrates. OPV devices employing 8 nm Ag and Au electrodes, based on the PAL PCDTBT:$PC_{71}BM$ and with an active area of 1 cm^2, achieved PCEs of 3.7 % (Ag) and 4.25 % (Au) comparable to the PCE of 4.10 % for ITO-based reference devices. The UTMFs however were reported to more resistant to repeated bending.

3.2. Upscaling using carbon-based TCEs as bottom electrodes

Studies on the application of carbon-based transparent conducting electrodes (TCEs) in large area OPV cells and modules have focused on the use of carbon nanotube (CNT)-based and graphene-based electrodes, and these are briefly reviewed in this sub-section.

3.2.1. Carbon Nanotubes (CNT)-based TCEs

Carbon nanotubes (CNTs) have some outstanding properties such as high electrical conductivity and excellent mechanical and thermal properties that make them attractive for electrode applications in OPV devices. However, most of these properties are along their axial direction, i.e. highly anisotropic, which makes their industrial application very challenging.

The first application of CNT-based bottom TCE as a replacement of the ITO electrode in OPVs, was reported in 2005 by Du Pasquier et al. [263] in a small area device that achieved a PCE of ~1 %. Since then, a considerable number of studies have tested the use of CNTs as bottom TCE in OPVs and these studies have been discussed in a large number of reviews broadly related with the use of CNTs in thin film TCEs and the application of these TCEs in OPV devices [264-272].

While some progress has been made regarding the application of CNT-based TCEs in OPVs [273], this research topic is still on its infancy, due to the complexities involved, and no literature studies are known on large area (> 1 cm^2) OPVs using CNT-based TCEs.

3.2.2. Graphene-based TCEs

Graphene combines a good optical transmittance, electrical conductivity, chemical stability and flexibility making it a very attractive material for electrode applications [274,

275]. The first example application of graphene-based bottom TCE in small area OPVs was reported by Peumans and co-workers in 2008 [276]. Since then, the application of graphene in TCEs and of these TCEs as bottom electrode in OPV devices has been extensively investigated as described in several literature reviews [270, 271, 277-286]. However, despite all the progress achieved, the majority of the most important studies focus on small area OPV devices [287-290]. Reports of OPV devices based on graphene bottom electrodes and with large active area (≥ 1 cm^2) are still very scarce in the literature [291, 292] and these are briefly described below.

Konios et al. [291] developed a laser-based patterning technique, compatible with plastic substrates, for the production of reduced graphene oxide micromesh (rGOMM) electrodes over large areas. This technique was used to increase the transparency of reduced graphene oxide (rGO) films from ~20 % to up to ~85 %, with only a minor increase in the respective sheet resistance value. These rGOMM electrodes were tested in OPV cells with area of 1.35 cm^2, based on PCDTBT:$PC_{71}BM$ active layers, and exhibited an average PCE of 1.07 % compared with 1.38% for a similar ITO-based reference device.

More recently, La Notte et al. [292] prepared a 4-layer (4L) graphene electrode doped with $SOCl_2$ by chemical vapor deposition (CVD) and transferred it to glass. This was then used it as cathode in OPV devices having an inverted structure. The 4L-graphene electrode had a transmittance value of 88.1 % at 550 nm and a sheet resistance R_s of 30 $\Omega \cdot \square^{-1}$. Devices were prepared with the structure: Glass/graphene/PEDOT:PSS/ZnO/PEIE/PffBT4T-2OD:$PC_{71}BM$/V_2O_5/Ag. A mini-module composed of 3 cells, based on the 4L-graphene electrode, and with total active area of 1.6 cm^2 exhibited a PCE of 0.44% (Figure 14).

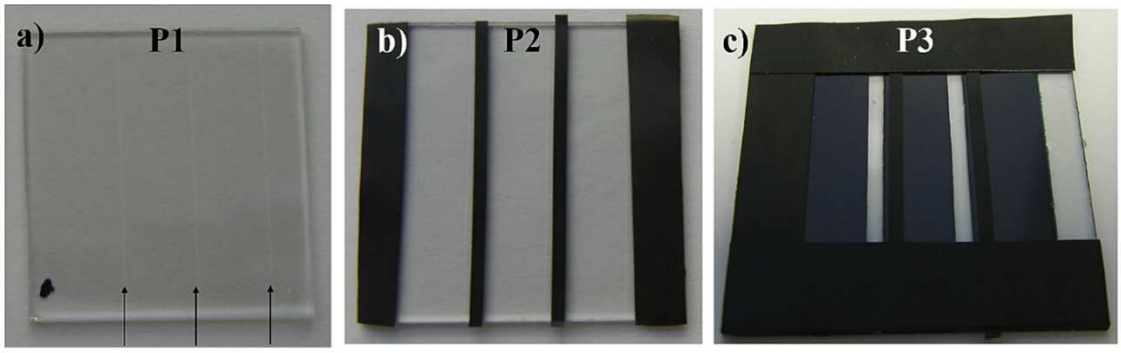

Figure 14. Photo of the graphene sample at each patterning step: a) P1 by laser scribing, b) P2 by shadow mask and c) P3 by shadow mask. (reproduced with permission from ref. [292]).

3.3. Upscaling using conducting polymer TCEs as bottom electrodes

PEDOT:PSS is an electrically conductive complex of poly(3,4-ethylenedioxythiophene) (PEDOT) and poly(4-styrenesulfonate) (PSS) where the PSS works as a dispersion agent in aqueous medium [293]. PEDOT:PSS electrodes have been tested as potential substitute for the ITO electrode in OPVs [294].

In 2004, Aernouts et al. [295] made the first reports of the use of a highly conductive PEDOT:PSS anode as a potential substitute for ITO in OPV devices. Other studies have then followed using small area devices [296-300]. Due to the relatively large optical absorption coefficient of PEDOT:PSS, PEDOT:PSS films need to have a thickness below 100 nm to maintain a high transmittance. This significantly raises the sheet resistance of the electrodes limiting the application potential of pure PEDOT:PSS-based devices.

In a 2019 study, Wang et al. [301] prepared TCEs based on high conductivity PEDOT:PSS PH 1000 on ultrathin (100 μm-thick) flexible glass substrates, with optimized TCEs exhibiting a R_S of ~30 $\Omega \cdot \square^{-1}$ and a transmittance of ~ 77 % at 550 nm, with a broad transparency window observed between 300 – 800 nm. OPV cells with active area 1.6 cm^2 and with the structure glass/PEDOT:PSS PH1000/MoOx/BQR:$PC_{71}BM$/Ca/Al achieved a PCE of 5.2 % (compared to 8.0 % for devices with small area of 0.2 cm^2). Also in 2019, Meng et al. [68] produced flexible modules composed of 6 cells with a total active area of 15 cm^2 having the structure PET/hc-PEDOT:PSS/ZnO/PAL/MoO_3/Ag, where the high conductivity (hc-) PEDOT:PSS, the ZnO and the PAL were slot-die-coated. Modules prepared with the PAL blends PTB7-Th:$PC_{71}BM$ and PBDB-T:ITIC achieved average/maximum PCEs of 7.25/7.58 % and 8.64/8.90 % respectively. These represent the highest efficiency values reported so far for large area OPVs based on PEDOT:PSS bottom electrodes.

3.4. Upscaling using opaque bottom electrodes with top (backside) illumination

A different strategy for the replacement of ITO as the bottom electrode consists in using opaque bottom electrodes and illuminating the devices from the top (backside).

In 2009 Frederik Krebs [302] reported on the use of opaque bottom electrodes made of Cu(50 μm)/Ti (100 nm) in large area modules illuminated from top. This strategy has since been followed by others [36, 100, 303-316] and the list of opaque electrodes tested

includes mostly thick (typically ~100 nm) silver [36, 100, 303-310] and aluminium films [311-313] among others [314-316].

In 2015, Huang et al. [100] reported top-illuminated single cells with an active area of 1 cm^2 and with a thick (100 nm) opaque Ag bottom electrode exhibiting a PCE of 7.21 %, based on a PBDTT-F-TT:$PC_{71}BM$ PAL. The cells had the inverted architecture glass/thick-Ag/FPI-PEIE/PAL/MoO_3/UTMF-Ag/TeO_2, where "MoO_3/UTMF-Ag/TeO_2" is a UTMF-based microcavity semi-transparent top-electrode that allows for efficient light in-coupling. This PCE was considerably higher than the PCE of reference ITO-based inverted cells (5.70 %). In the same year, Zuo et al. [304] reported OPV cells with an active area of 4 cm^2 using an opaque 100 nm thick Ag film (on glass or PET) as bottom electrode, and ultrathin thickness-gradient Ag TCE as top electrode. Devices based on a PTB7-Th:$PC_{71}BM$ PAL achieved PCEs of 7.15 % and 7.09 % on glass and PET substrates respectively. Later, the same authors [305] produced similar cells with opaque Ag bottom electrodes which were also based on a PTB7-Th:$PC_{71}BM$ PAL, but where the ultrathin thickness-gradient Ag top electrode was replaced by a triangular shaped Ag-grid. The 4 cm^2 cells on glass substrates achieved a PCE of 6.93 %. Mao et al. [36] reported 10.5 cm^2 active area flexible tandem cells using an opaque Ag film (80 nm) as bottom electrode. Cells using two different PALs, namely PAL1 = P3HT:ICBA and PAL2 = PTB7-Th:$PC_{61}BM$, yielded maximum PCE values of 6.50 %. Compared to single junction cells, tandem cells are less susceptible to parasitic area upscaling effects and exhibit a superior tolerance to defects. Producing tandem cells, the authors demonstrated that a toy electric car could be powered to run under sunlight [317] (Figure 15). Opaque Ag films covered with TiOx were used by Lin et al. [307, 308] to produce OPV cells with an active area of 2.03 cm^2. Cells based on a blade-coated PTB7-Th:ITIC PAL achieved a PCE of 7.60 % [307] and cells based on a blade-coated all-polymer PAL (PTB7-Th:PNDI-T10) achieved a maximum PCE of 6.65 % [308]. Very recently, Jiang et al. [310] demonstrated the growth of a very smooth Ag layer (rms = 1.06 nm) with a thickness of 70 nm (opaque) on top of a chemically reactive hydrogen molybdenum bronze ($HxMoO_3$) surface. Top-illuminated 10 cm^2 NFA-based OPV cells with structure glass/$HxMoO_3$/opaque Ag (70 nm)/PAL/$HxMoO_3$/ultrathin Ag (8 nm)/MoO_3, where the PAL consisted of PM6:IT-4F, achieved an impressive PCE of 10.24% [310].

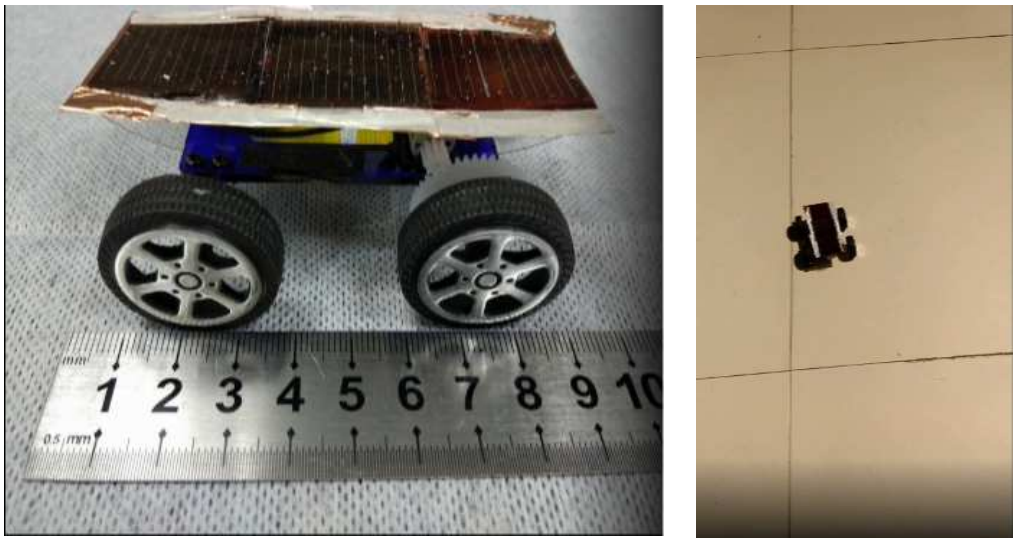

Figure 15. Frames from a movie showing a toy electric car being powered to run under sunlight. It uses a flexible tandem OPV with structure PES/Ag/PEI/PAL1/m-PEDOT:PSS/PEI/PAL2/ hc-PEDOT:PSS/Ag-grid. The movie, from the work of Mao et al. [36], can be found in the URL at ref. [317].

Using an opaque Al film (100 nm thick) as bottom electrode, Ibraikulov et al. [313] produced modules of 15 monolithic cells connected in series, based on a blade-coated PAL of PF2:$PC_{71}BM$, with an impressive total active area of 66 cm^2 (GFF = 69 %) that achieved a PCE of 6.1 %.

4. Encapsulation and stability testing of large area devices

OPV devices will only become a commercial success if they can have both a high power conversion efficiency and exhibit long-term stability at a reasonable price. After rapid recent improvements observed in PCE, Increasing the operational lifetime of OPV devices has become particularly important for practical applications.

Important advances in the stability of OPV devices have been made recently. Du et al. [318] reported small area OPV cells exhibiting a PCE of ~8 % along with an extrapolated operational lifetime approaching 10 years. Xu et al. [319] demonstrated small area OPV cells with a PCE of 10 % combined with an extrapolated potential lifetime of 22 years, based on an estimated absorbed optical energy dose. Despite these significant improvements on the lifetime of small area OPVs, the lifetime of large area OPVs, which indirectly determine the EPBT is still poor compared to the 25 years that inorganic silicon-based solar cells can last. Therefore, significant improvements still need to be made in terms of stability to make OPV technology attractive for mass production and commercialization.

The factors that contribute to the reduction in operational efficiency of OPV cells and modules over time are several and have been clearly identified [320-329]. Degradation factors that are common to all OPV devices include: photochemical and photophysical degradation of the active layer materials and interfaces [330-332]; morphological degradation [333, 334] due to high thermal stress under operation; as well as a series of degradation events that can be initiated by the ingress of H_2O and O_2 in poorly sealed devices [335-337]. Additionally, there are some degradation factors specific to OPV modules, including electrical stress [338] and degradation at the cell interconnections. A detailed description of all these degradation factors and corresponding mechanisms is beyond the scope of this review, and the interested readers are directed to some existing reviews on this topic [320-329].

Some strategies to improve the stability of OPV cells and modules have focused on improving the intrinsic stability of the materials and interfaces. For example, chemical modification of polymer donors, either modification of backbone or side chains, has proved effective to improve the stability of OPV devices [212, 339, 340]. An increase in the polymer molecular weight [341-343] and in polymer regioregularity [333] have also been shown to produce more stable devices. NFA–based OPVs, have been demonstrated

to exhibit, in general, considerably higher thermal and photochemical stability than the corresponding fullerene based OPVs [82, 218, 344-347]. Also, among NFAs, end-group and side-chain modifications have shown to strongly influence both device photo-stability and morphological stability [318]. Therefore, in outdoor conditions and especially in tropical regions where high stability at elevated temperature is crucially important, replacing fullerene by NFAs is a promising strategy to extend the device lifetime up to the commercial requirements. Ternary blending of the PAL through the addition of compatibilizers with light harvesting properties [94, 348-351] has proved to be a powerful strategy to improve the morphological stability of the PAL with an associated increase in the lifetime of OPVs which is often also with associated enhancements in PCE. Replacement of the PEDOT:PSS HTL either by thin films of solution-processed molybdenum oxide (MoOx) [352] or by a thin V_2O_5 layer [353]; the plasma treatment of interfacial layers [354]; the replacement of the front and back electrodes [251, 355]; as well as the choice of more favourable device architectures [355-358] has also been used successfully to improve the OPVs lifetime. UV-blocking filters that can attenuate most UV photons below 400 nm have also proved successful in extending lifetime [359]. Other strategies have focused on preventing the ingress of H_2O and O_2 through encapsulation of the devices (extrinsic stability) [339, 358, 360-367]. However, most of these strategies have either been applied only to small area devices (< 1 cm^2) or, when applied to larger areas, have resulted in devices with relatively modest lifetimes (<< 1 year).

In this section we present and discuss the most relevant stability studies performed on large area (≥ 1 cm^2) OPV cells and modules. It should be noted that the vast majority of these studies focus on devices based on P3HT:$PC_{61}BM$ blends, chosen primarily because of the commercial availability of P3HT and $PC_{61}BM$ in the quantities required for large scale production and at a reasonable price. Also, for these reasons, the majority of such studies focus on mitigating extrinsic degradation factors (H_2O and O_2) through the development of different encapsulation strategies, rather than on improving the intrinsic stability of the devices. Although the P3HT:$PC_{61}BM$ system has promising stability, the corresponding devices exhibit a PCE well below the commercial requirements (maximum small area PCE ~ 5 %) and therefore, the interest in this system is currently purely academic.

4.1.Stability testing and encapsulation

OPV devices typically suffer an initial period of faster reduction in their PCE, known as the "burn-in" period, after which a much slower and typically linear reduction of PCE occurs with time (Figure 16(a)). Two different lifetime parameters, namely T_{80} and T_{s80}, are typically used to quantify the operational lifetime of OPV devices [358, 368, 369]. The T_{80} lifetime is the time it takes for the PCE of the cell or module to decrease to 80 % of its very initial value. The T_{s80} lifetime is defined as the time needed for the PCE of the device to decrease to 80 % of its value at the end of the burn-in period. Interestingly, recent studies have shown that NFA–based OPVs may not have a burn-in period [347].

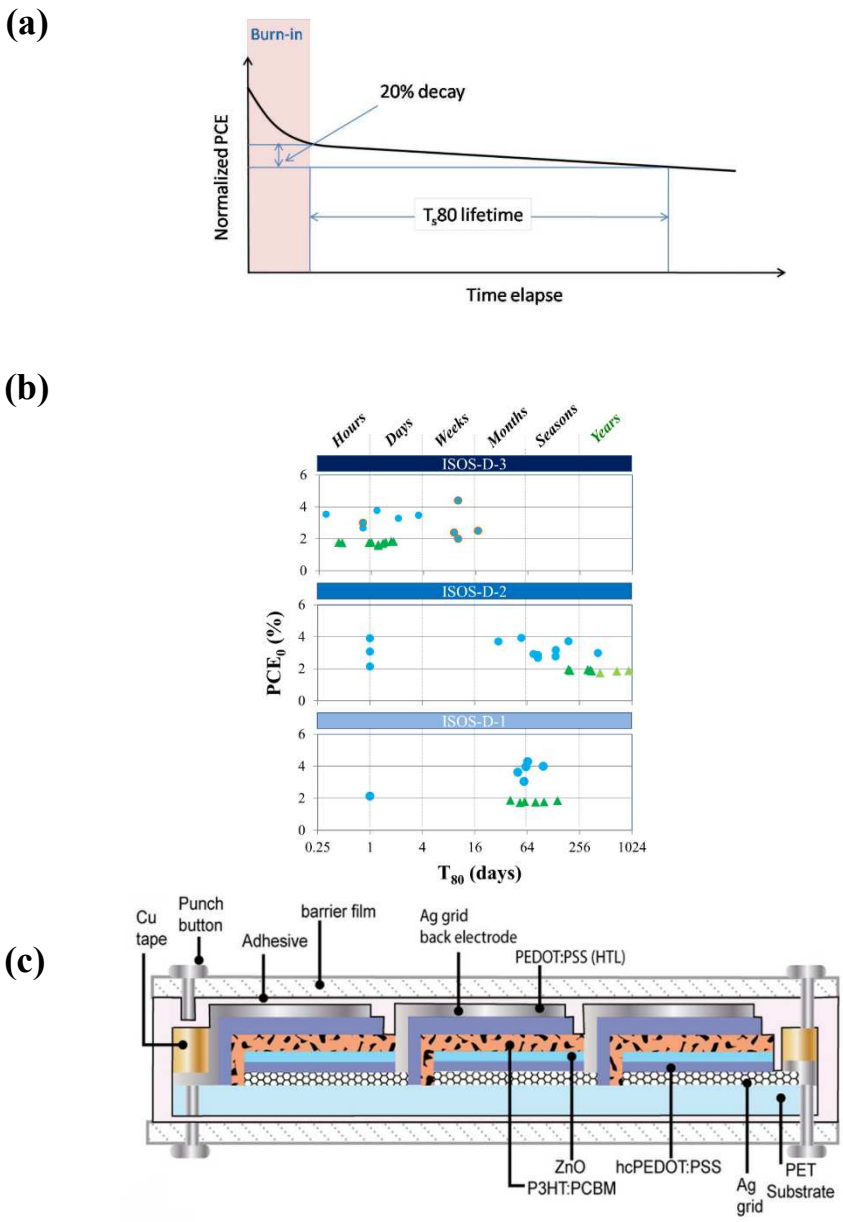

Figure 16. (a) Typical degradation behaviour of an OPV device (reproduced with permission from ref. [368]); (b) Lifetime diagram for intercomparison of lifetime of different OPV devices.

X axes present logarithmic function with base 4, which is associated with the time unites shown above the plot. Y axes represent the PCE of the device at the T_0 point, from where T_{80} was calculated (readapted with permission from ref. [370]); (c) Encapsulation scheme of the ITO-free IOne modules (from ref. [371]).

Until 2010 there were no specific standards for OPV lifetime testing and the standard IEC61646, originally created for amorphous silicon thin film solar cells was often used. However, as the degradation mechanisms of silicon based PVs and OPVs are different, an International Summit on Organic solar cell Stability (ISOS) in 2011 established a set of guidelines to allow ready comparison of data obtained by different laboratories [372]. Five main testing protocols were created with each protocol containing three levels of complexity, named levels 1, 2 and 3, corresponding respectively to "Basic", "Intermediate" and "Advanced". The five protocols created were: i) Dark tests (ISOS-D-1; ISOS-D-2 and ISOS-D-3); ii) Outdoor tests (ISOS-O-1; ISOS-O-2 and ISOS-O-3); iii) Laboratory weathering tests (ISOS-L-1; ISOS-L-2 and ISOS-L-3); iv) Thermal cycling tests (ISOS-T-1; ISOS-T-2 and ISOS-T-3) and v) Solar-thermal-humidity cycling tests (ISOS-LT-1; ISOS-LT-2 and ISOS-LT-3). More details about these testing protocols can be found in the literature [372]. ISOS-T and ISOS-LT tests are rarely used due to their complexity and low stability of most OPVs under such harsh conditions. In the following discussion, particular emphasis is placed on the results from outdoor stability tests (ISOS-O) as these most closely represent operation under real conditions.

A novel OPV lifetime diagram (entitled o-diagram), see Figure 16(b), was proposed by Krebs and co-workers for comparing lifetimes of different OPV technologies and/or different test conditions [370]. O-diagrams plot the initial device performance versus the T_{80} values in a Log4 scale (units of days); base 4 is used since it allows the scale to be associated with common time units (hours, days, months, seasons, years).

OPVs degrade in ambient air mostly because of moisture and oxygen, and therefore OPV cells are usually fabricated inside a glove box and are encapsulated before exposure to ambient air. The most common encapsulation method sandwiches the OPV device between two or more barrier films whose edges are glued together with a sealant. In the encapsulation of OPVs, barrier films and sealants with low water vapour transmission rate (WVTR ~ 10^{-6} $gm^{-2}day^{-1}$) and low oxygen transmission rate (OTR ~ 10^{-3} $cm^3m^{-2}day^{-1}$) need to be used to improve lifetime [364] and a certain distance between edge sealing and the OPV edge should be left to avoid O_2 and H_2O edge ingress. Although sealants

can be pressure sensitive, hot-melt or UV curable epoxy-based adhesives, a study suggests that UV curable epoxy-based adhesives are the most effective [373].

Rigid glass panels are the most hermetic barriers films known for OPVs, where OPV cells and modules can be sandwiched in between two panels [374]. Large area rigid glass-glass encapsulation can be used for example in building integrated OPV (BiOPV) products, such as glass facades [375]. In the most common encapsulation method, large area devices are laminated between films of cross-linkable ethylene vinyl acetate (EVA) in vacuum, under compression and up to 150°C, which requires the PAL to be stable for ~2 hours at 150 ºC to ensure glass sealing [103, 376]. However, recent progress in laser assisted glass sealing will likely soon make this compression method obsolete, as it can guarantee the hermetic glass sealing at a process temperature < 80 ºC. Although glass encapsulation using laser-assisted glass-frit sealing has been much studied to seal other related photovoltaic technologies, such as large area dye sensitized (DSSC) [377] and perovskite (PSC) [378] solar cells, no studies are currently known in literature on the use of this technology to glass seal large area OPVs. Furthermore, the use of ultrathin flexible glass substrates on OPVs, compatible with R2R processing, is still very limited [379, 380]. Despite encapsulation being known to play a decisive role in increasing the stability of OPV devices [381], limited information is usually provided about the encapsulation procedures. An analysis of literature data on rigid (front and back glass) and flexible (mostly PET foils) encapsulated devices have shown that device lifetime is mostly limited by the quality of the edge sealing and not by the water vapor or oxygen permeability of the barrier films (glass and PET) [382]. Solving the problem of efficient edge sealing has been highlighted as a crucial step towards improving the lifetime of devices [374, 382, 383].

Several other materials have been tested as effective encapsulation barrier layers to inhibit atmosphere-induced degradation. These include graphene oxide based barrier films [384], ultra-thin AlOx layers deposited by ALD [385], multilayer stacks of MgF_2/MoO_3 [386], ZnO/UV-resin [387], among others. However, all of these strategies [384-387] have been so far limited to small area devices (< 1 cm^2).

4.2.Stability of large area cells and modules

This sub-section reviews the most relevant studies on the stability performed of large area OPV devices, giving emphasis to outdoor stability studies (ISOS-O) and laboratory

weathering tests (ISOS-L). As mentioned above, these studies mostly focus on the P3HT:$PC_{61}BM$ PAL system and on different encapsulation strategies to mitigate the deleterious action of extrinsic degradation factors (H_2O and O_2). Table S4 summarizes the most important results obtained applying ISOS-O and ISOS-L protocols where, as a benchmark for stability, only tests and lifetimes with duration > 1 year are indicated.

One of the earliest demonstrations of the encapsulation of large area OPV devices was made by Krebs et al. [388] in 2004. Devices based on MEH-PPV with an area of 100 cm^2 were laminated using PET, however the lamination had a negative effect on the lifetime. In 2006, Krebs [389] encapsulated a cell based on P3HT:PCBM with active area of 10 cm^2 using a thick glass substrate and an aluminium backplate using a glass fibre reinforced thermosetting epoxy (prepreg), requiring a thermosetting time of 12 h. Typical devices achieved a PCE of 0.48 % immediately after encapsulation, which dropped to 0.31 % after ~1 year under ambient conditions.

In 2008, flexible P3HT:PCBM based modules with an initial PCE > 1 % and packaged with transparent barrier films were tested at the Konarka rooftop testing setup in Lowell (USA) [390] and exhibited no performance losses after a 14 month testing period.

Gevorgyan et al. [391] used *ProcessOne* to produce modules with 16 serially connected cells employing an inverted structure ITO/ZnOx/P3HT:PCBM/PEDOT:PSS/Ag-paste and with a total active area of ~35.5 cm^2. The modules were encapsulated using a UV filter/barrier (Amcor) with a pressure sensitive adhesive (467 MPF, 3M) and demonstrated initial PCE values between 0.7 % and 1.4 %. Their outdoor stability was then tested in 6 laboratories in 4 countries (Germany, Israel, Australia and Denmark). In addition to the encapsulation, the device terminals were protected against H_2O and O_2 diffusion which proved to be crucially important. The most stable modules had well sealed terminals and demonstrated a T_{80} > 416 days contrary to modules with unprotected device terminals which exhibited T_{80} < 21 days.

Sapkota et al. [316] used UV curing epoxy glue together with glass plates or flexible barrier films to encapsulate backside illuminated OPV cells having an active area of 1.1 cm^2 and with the inverted geometry Cr/Al/Cr/P3HT:PCBM/PEDOT:PSS/metal-grid. Devices encapsulated between two glass plates were able to maintain 90 % of their initial PCE (2.7 %) after > 12000 h following continuous illumination at 1000 W/m^2 (similar to

AM1.5 G but with low UV content) and at an ambient temperature of ca. 50 ºC and ca. 6 % RH.

Fully printed *IOne* modules with active areas of 70 – 100 cm^2 and PET/Ag-grid/PEDOT:PSS/ZnO/P3HT:PCBM/ PEDOT:PSS/Ag-grid structure were tested by Krebs and co-workers [392] for outdoor stability assessment over 1 year, with devices located in Denmark (ISOS-O-3) and the Netherlands (ISOS-O-1). Modules with different PET substrate thickness (45 μm; 125 μm) were laminated between two sheets of food packaging barrier using a UV curable adhesive and with different edge sealing margins (<< 1 cm and > 1 cm). The best modules, in both countries, had a PET substrate thickness of 125 μm and an edge sealing margin >1 cm, and exhibited T_{80} > 1 year. Large area (100 cm^2), R2R processed P3HT:PCBM based OPV modules that were manually laminated between barrier foils using a UV-curable adhesive were tested by Angmo et al. [371] for their stability. The encapsulation was performed feeding the "barrier / adhesive / module / adhesive / barrier" through the nip pressure of a R2R coater to achieve homogenous distribution of the adhesive and thereafter curing the adhesive under UV light. Before encapsulation, the module terminal contacts/busbars were covered with a copper tape and metal snap fasteners that were punched through over them after encapsulation (Figure 16(c)). Impressive values of T_{80} > 2 years were obtained, under protocols ISOS-O-3 and ISOS-D-2. The results suggested that O_2 permeation may be responsible for degradation mainly under outdoor conditions, whereas WVTR has a larger impact under dark conditions.

Weerasinghe et al. [393], tested the outdoor stability (ISOS-O-2) of fully-printed OPV modules (having an active area ~50 cm^2), comprising of 5 individual cells connected in series with a PET/ITO/ZnO/P3HT:PCBM/PEDOT:PSS/Ag configuration. Various encapsulation architectures (partial, perforated and ; complete) were tested using commercially available flexible barrier films and adhesives. Completely encapsulated modules showed no evidence of PCE loss after 13 months of outdoor exposure and a T_{80} of at least 3 years was anticipated. No absolute values of PCE were reported.

Other stability studies of large area OPV cells and modules have been performed testing different experimental variables such as: i) single-junction *versus* tandem devices [394]; ii) different encapsulation protocols (complete; partial) [170]; iii) different encapsulation barrier foils [209]; iv) different adhesives (UV-curable; pressure-sensitive) [207]; v) the effect of edge sealing [374, 383]; vi) the lifetime reproducibility among different

laboratories [370] and vii) combined application of different stress factors on the adhesion of OPV interfaces in large area R2R devices [395]. However, in all of these studies the reported values of T_{80} were << 1 year.

The vast majority of the stability tests reviewed above for large area devices were based on a P3HT:PCBM PAL and therefore, despite some encouraging stability results obtained (T_{80} > 1 year), their initial PCE values were rather low (typically < 3 %). Therefore, demonstrating OPV devices with simultaneously high PCE (> 10 %), large area (>> 100 cm^2) and high stability (T_{80} > 10 years) – the ultimate goal of the OPV field – has still not been reached. However, some recent studies suggest that real progress is being made in this regard. For example a recent study by Chang et al. [145] explored carefully encapsulated modules based on a PV2000:PCBM PAL having a total active area of 23.7 cm^2 and an initial PCE of 7.56 %; here is was shown that modules were able to maintain 91.7 % of their initial PCE value after 1000h under AM 1.5G light-soaking. Furthermore, Distler et al. [125] fabricated PM6:Y6-based modules with areas of 26 and 204 cm^2 respectively having PCEs of 12.6 % and 11.7 %; again no significant degradation was observed during the in-house characterisation measurements and certification process, which lasted several days and included extended AM1.5G irradiation at 1000 W/m^2.

5. Conclusions and future directions

The field of organic photovoltaics has witnessed a rapid development in very recent years, mainly due to the development of new polymer donors and NFAs. To date, the PCE of ITO-based single cells with active area ≥ 1.0 cm^2 has reached over 15 %, with the PCE of ITO-based modules having active areas ≥ 10 cm^2 and ≥ 100 cm^2 has reached over 14 % and 12 % respectively. These are very encouraging results, with this progress all being made in the last year. These devices were prepared using vacuum processing steps, however the PCE of devices prepared using vacuum-free techniques still lags far behind. Although vacuum processing increases the complexity and cost of device fabrication, it is not incompatible with upscaling. Therefore, unless the efficiency gap between vacuum and vacuum-free processed devices can be reduced considerably in the future, it is likely that vacuum-processing will form an integral part of any future OPV device manufacture process.

The most successful ITO-free strategy, particularly for larger area devices ≥ 10 cm^2, has consisted in the use of highly conductive thick metal films (~100 nm) as opaque bottom electrodes in back illuminated devices; here PCEs of 10.24 % and 6.1 % in devices with active areas of 10 cm^2 and 66 cm^2 respectively are among the most impressive efficiencies reported so far. To create ITO-free devices with a bottom TCE, most research has been concentrated on the development of silver grids. Here metal grids suffer from the inherent limitation that high conductivity and high transparency are difficult to combine in a single material and a trade-off has to be met between these two properties. However, recent studies using hexagonal Ag/Cu grids reported PCEs > 12 % in 1.0 cm^2 cells; a value that currently represents a record PCE for large area ITO-free devices. Although the use of high conductivity PEDOT:PSS as bottom electrode has received far less attention, some recent reports suggest this to be a promising strategy; here a PCE of 8.90 % was reported in devices having an active area of 15 cm^2.

Despite these impressive very recent developments, the large majority of upscaling studies performed so far (particularly to very large areas of > 100 cm^2) have been performed based using the standard P3HT:PCBM blend system due to the higher availability and lower price of these materials compared to other donor:acceptor pairs. However, the P3HT:PCBM system typically exhibits low PCE (≤ 4 %) even in small area (a few mm^2) devices. It is therefore difficult to judge the real effect of upscaling on PCE using a system that intrinsically exhibits low performance. More systematic upscaling

studies are needed using donor:acceptor pairs that demonstrate high performances (> 10 %) in small area devices, with special focus on systems containing NFAs.

Long-term device stability is also needed for commercial applications and requires improvements in both intrinsic and extrinsic stability. Here, the replacement of fullerenes by NFAs seems a promising strategy as these materials appear to have higher intrinsic stability and should result in an increase in device lifetime. In parallel, more effort should be placed in developing new encapsulation strategies to enhance the extrinsic stability of devices. Encapsulation studies have so far been relatively scarce and mostly rely on the use of epoxy-based adhesives as sealants. Surprisingly, glass frit sealing technology which has been intensively studied for encapsulating large area dye sensitized solar cells (DSSCs) and perovskite solar cells, has still not been tested in large area OPVs. Notably for BIPV applications in which OPV devices are embedded in glass requires devices to be stable for at least 2 hours at 120 ºC during the lamination process. However, this demanding requirement is partially lifted due to recent advances in laser assisted glass frit sealing, as encapsulation can now be performed in a few minutes at temperatures as low as 80 ºC. As far as we are aware, these new advances in laser assisted glass frit sealing have not been tested in large area OPVs.

The development of flexible OPV technologies remains a highly attractive goal. Previously this mainly meant depositing devices on PET or PEN substrates. However, ultra-thin flexible glass is becoming increasingly popular amongst a range of related technologies, and its implementation in OPVs devices also looks to be a very attractive prospect.

The ultimate objective of these developments is to combine high efficiency performance and high stability in large area modules, with the 10-10 target, i.e. 10 % efficiency and 10 years stability being a key goal. Outdoor operational lifetime studies of OPV modules now report lifetimes of several years. Despite the fact that there is still a way to go to reach the 10-10 target, this represents an encouraging result considering that 10 years ago, typical device lifetimes were in the range of a few days to weeks.

Acknowledgements

G. Bernardo and T. Lopes thank the Portuguese Foundation for Science and Technology (FCT) for the financial support of their work contracts through the Scientific Employment Stimulus - Individual Call – (CEEC_IND/02039/2018), and the Scientific Employment Support Program (Norma Transitória DL 57/2017), respectively. This work was financially supported by: Base Funding UIDB/00511/2020 of the Laboratory for Process Engineering, Environment, Biotechnology and Energy – LEPABE - funded by national funds through the FCT/MCTES (PIDDAC); and Project HopeH_2 POCI-01-0145-FEDER-030760, funded by FEDER funds through COMPETE2020 – Programa Operacional Competitividade e Internacionalização (POCI) and by national funds (PIDDAC) through FCT/MCTES.

D. G. Lidzey thanks the UKRI for part funding via research grants EP/S009213/1, EP/S000763/1 and ST/R002754/1.

6. References

1. Tang, C.W., *2-Layer Organic Photovoltaic Cell.* Applied Physics Letters, 1986. **48**(2): p. 183-185.
2. Sariciftci, N.S., et al., *Photoinduced Electron-Transfer From a Conducting Polymer To Buckminsterfullerene.* Science, 1992. **258**(5087): p. 1474-1476.
3. Yu, G., et al., *Polymer Photovoltaic Cells: Enhanced Efficiencies via a Network of Internal Donor-Acceptor Heterojunctions.* Science, 1995. **270**(5243): p. 1789-1791.
4. Gaspar, H., et al., *Recent Developments in the Optimization of the Bulk Heterojunction Morphology of Polymer: Fullerene Solar Cells.* Materials, 2018. **11**(12).
5. Ganesamoorthy, R., G. Sathiyan, and P. Sakthivel, *Review: Fullerene based acceptors for efficient bulk heterojunction organic solar cell applications.* Solar Energy Materials and Solar Cells, 2017. **161**: p. 102-148.
6. Cheng, P., et al., *Next-generation organic photovoltaics based on non-fullerene acceptors.* Nature Photonics, 2018. **12**(3): p. 131-142.
7. Zhang, J.Q., et al., *Material insights and challenges for non-fullerene organic solar cells based on small molecular acceptors.* Nature Energy, 2018. **3**(9): p. 720-731.
8. Yan, C.Q., et al., *Non-fullerene acceptors for organic solar cells.* Nature Reviews Materials, 2018. **3**(3).
9. Hou, J.H., et al., *Organic solar cells based on non-fullerene acceptors.* Nature Materials, 2018. **17**(2): p. 119-128.
10. Wadsworth, A., et al., *Critical review of the molecular design progress in non-fullerene electron acceptors towards commercially viable organic solar cells.* Chemical Society Reviews, 2019. **48**(6): p. 1596-1625.
11. Gurney, R.S., D.G. Lidzey, and T. Wang, *A review of non-fullerene polymer solar cells: from device physics to morphology control.* Reports on Progress in Physics, 2019. **82**(3).
12. Ma, L.J., et al., *Recent advances in non-fullerene organic solar cells: from lab to fab.* Chemical Communications, 2020. **56**(92): p. 14337-14352.
13. *Best Research-Cell Efficiency Chart*. 2020, National Renewable Energy Laboratory.
14. Zheng, Z., et al., *PBDB-T and its derivatives: A family of polymer donors enables over 17% efficiency in organic photovoltaics.* Materials Today, 2020. **35**: p. 115-130.
15. An, C., Z. Zheng, and J. Hou, *Recent progress in wide bandgap conjugated polymer donors for high-performance nonfullerene organic photovoltaics.* Chemical Communications, 2020. **56**(35): p. 4750-4760.
16. Gedefaw, D., X. Pan, and M.R. Andersson, *Recent Advances in the Synthesis of Electron Donor Conjugated Terpolymers for Solar Cell Applications.* Frontiers in Materials, 2020. **7**.
17. Zheng, B., L.J. Huo, and Y.F. Li, *Benzodithiophenedione-based polymers: recent advances in organic photovoltaics.* Npg Asia Materials, 2020. **12**(1).
18. Duan, C.H. and L.M. Ding, *The new era for organic solar cells: polymer donors.* Science Bulletin, 2020. **65**(17): p. 1422-1424.
19. Kini, G.P., S.J. Jeon, and D.K. Moon, *Design Principles and Synergistic Effects of Chlorination on a Conjugated Backbone for Efficient Organic Photovoltaics: A Critical Review.* Advanced Materials, 2020. **32**(11).
20. Yao, H.F., et al., *Recent Progress in Chlorinated Organic Photovoltaic Materials.* Accounts of Chemical Research, 2020. **53**(4): p. 822-832.
21. Zhao, Q.Q., J.F. Qu, and F. He, *Chlorination: An Effective Strategy for High-Performance Organic Solar Cells.* Advanced Science, 2020. **7**(14).
22. Lin, Y.Z., et al., *An Electron Acceptor Challenging Fullerenes for Efficient Polymer Solar Cells.* Advanced Materials, 2015. **27**(7): p. 1170-1174.
23. Yuan, J., et al., *Single-Junction Organic Solar Cell with over 15% Efficiency Using Fused-Ring Acceptor with Electron-Deficient Core.* Joule, 2019. **3**(4): p. 1140-1151.

24. Ryu, H.S., et al., *Recent progress in indoor organic photovoltaics.* Nanoscale, 2020. **12**(10): p. 5792-5804.
25. Mainville, M. and M. Leclerc, *Recent Progress on Indoor Organic Photovoltaics: From Molecular Design to Production Scale.* Acs Energy Letters, 2020. **5**(4): p. 1186-1197.
26. Mathews, I., et al., *Technology and Market Perspective for Indoor Photovoltaic Cells.* Joule, 2019. **3**(6): p. 1415-1426.
27. Chen, F.C., *Emerging Organic and Organic/Inorganic Hybrid Photovoltaic Devices for Specialty Applications: Low-Level-Lighting Energy Conversion and Biomedical Treatment.* Advanced Optical Materials, 2019. **7**(1).
28. Biswas, S. and H. Kim, *Solar Cells for Indoor Applications: Progress and Development.* Polymers, 2020. **12**(6).
29. Zhang, Y., C. Duan, and L. Ding, *Indoor organic photovoltaics.* Science Bulletin, 2020.
30. Cui, Y., L. Hong, and J.H. Hou, *Organic Photovoltaic Cells for Indoor Applications: Opportunities and Challenges.* Acs Applied Materials & Interfaces, 2020. **12**(35): p. 38815-38828.
31. Hou, X.Y., et al., *Indoor application of emerging photovoltaics-progress, challenges and perspectives.* Journal of Materials Chemistry A, 2020. **8**(41): p. 21503-21525.
32. Lee, H.K.H., et al., *Organic photovoltaic cells - promising indoor light harvesters for self-sustainable electronics.* Journal of Materials Chemistry A, 2018. **6**(14): p. 5618-5626.
33. Ma, L.K., et al., *High-Efficiency Indoor Organic Photovoltaics with a Band-Aligned Interlayer.* Joule, 2020. **4**(7): p. 1486-1500.
34. *Champion Photovoltaic Module Efficiency Chart*. 2019, National Renewable Energy Laboratory.
35. Carle, J.E., et al., *Overcoming the Scaling Lag for Polymer Solar Cells.* Joule, 2017. **1**(2): p. 274-289.
36. Mao, L., et al., *Flexible large-area organic tandem solar cells with high defect tolerance and device yield.* Journal of Materials Chemistry A, 2017. **5**(7): p. 3186-3192.
37. Mao, L., et al., *Patching defects in the active layer of large-area organic solar cells.* Journal of Materials Chemistry A, 2018. **6**(14): p. 5817-5824.
38. Zhan, Z., et al., *Inkjet-printed optoelectronics.* Nanoscale, 2017. **9**(3): p. 965-993.
39. Peng, X.J., et al., *Perovskite and Organic Solar Cells Fabricated by Inkjet Printing: Progress and Prospects.* Advanced Functional Materials, 2017. **27**(41).
40. Reale, A., et al., *Spray Coating for Polymer Solar Cells: An Up-to-Date Overview.* Energy Technology, 2015. **3**(4): p. 385-406.
41. Aziz, F. and A.F. Ismail, *Spray coating methods for polymer solar cells fabrication: A review.* Materials Science in Semiconductor Processing, 2015. **39**: p. 416-425.
42. Wang, G., et al., *Large-Area Organic Solar Cells: Material Requirements, Modular Designs, and Printing Methods.* Advanced Materials, 2019. **31**(45): p. 1805089.
43. Gertsen, A.S., et al., *Scalable fabrication of organic solar cells based on non-fullerene acceptors.* Flexible and Printed Electronics, 2019.
44. Søndergaard, R.R., M. Hösel, and F.C. Krebs, *Roll-to-Roll fabrication of large area functional organic materials.* Journal of Polymer Science Part B: Polymer Physics, 2013. **51**(1): p. 16-34.
45. Sondergaard, R., et al., *Roll-to-roll fabrication of polymer solar cells.* Materials Today, 2012. **15**(1-2): p. 36-49.
46. Krebs, F.C., *Fabrication and processing of polymer solar cells: A review of printing and coating techniques.* Solar Energy Materials and Solar Cells, 2009. **93**(4): p. 394-412.
47. Youn, H., H.J. Park, and L.J. Guo, *Organic Photovoltaic Cells: From Performance Improvement to Manufacturing Processes.* Small, 2015. **11**(19): p. 2228-2246.
48. Hösel, M., H.F. Dam, and F.C. Krebs, *Development of Lab-to-Fab Production Equipment Across Several Length Scales for Printed Energy Technologies, Including Solar Cells.* Energy Technology, 2015. **3**(4): p. 293-304.

49. Burgués-Ceballos, I., et al., *Towards industrialization of polymer solar cells: material processing for upscaling.* Journal of Materials Chemistry A, 2014. **2**(42): p. 17711-17722.
50. Lee, J., et al., *Green-solvent-processable organic semiconductors and future directions for advanced organic electronics.* Journal of Materials Chemistry A, 2020. **8**(41): p. 21455-21473.
51. Zhang, S., et al., *Green-solvent-processable organic solar cells.* Materials Today, 2016. **19**(9): p. 533-543.
52. Ma, Z.W., et al., *Green-solvent-processable strategies for achieving large-scale manufacture of organic photovoltaics.* Journal of Materials Chemistry A, 2019. **7**(40): p. 22826-22847.
53. Xu, X.P., et al., *Highly efficient non-fullerene organic solar cells enabled by a delayed processing method using a non-halogenated solvent.* Energy & Environmental Science, 2020. **13**(11): p. 4381-4388.
54. Brabec, C.J., et al., *Material Strategies to Accelerate OPV Technology Toward a GW Technology.* Advanced Energy Materials, 2020: p. 2001864.
55. Park, S., et al., *Progress in Materials, Solution Processes, and Long-Term Stability for Large-Area Organic Photovoltaics.* Advanced Materials.
56. Kang, H., et al., *Bulk-Heterojunction Organic Solar Cells: Five Core Technologies for Their Commercialization.* Advanced Materials, 2016. **28**(36): p. 7821-7861.
57. Jorgensen, M., et al., *The state of organic solar cells-A meta analysis.* Solar Energy Materials and Solar Cells, 2013. **119**: p. 84-93.
58. Po, R., et al., *From lab to fab: how must the polymer solar cell materials design change? - an industrial perspective.* Energy & Environmental Science, 2014. **7**(3): p. 925-943.
59. Doggart, P., N. Bristow, and J. Kettle, *Optimisation of the material properties of indium tin oxide layers for use in organic photovoltaics.* Journal of Applied Physics, 2014. **116**(10).
60. Zhao, W.C., et al., *Environmentally Friendly Solvent-Processed Organic Solar Cells that are Highly Efficient and Adaptable for the Blade-Coating Method.* Advanced Materials, 2018. **30**(4).
61. Dong, S., et al., *High-Performance Large-Area Organic Solar Cells Enabled by Sequential Bilayer Processing via Nonhalogenated Solvents.* Advanced Energy Materials, 2019. **9**(1): p. 1802832.
62. Sun, R., et al., *A universal layer-by-layer solution-processing approach for efficient non-fullerene organic solar cells.* Energy & Environmental Science, 2019. **12**(1): p. 384-395.
63. Sun, R., et al., *A Layer-by-Layer Architecture for Printable Organic Solar Cells Overcoming the Scaling Lag of Module Efficiency.* Joule, 2020. **4**(2): p. 407-419.
64. Kim, S., et al., *A Versatile Self-Organization Printing Method for Simplified Tandem Organic Photovoltaics.* Advanced Functional Materials, 2016. **26**(21): p. 3563-3569.
65. Hong, S., et al., *Effect of solvent on large-area polymer–fullerene solar cells fabricated by a slot-die coating method.* Solar Energy Materials and Solar Cells, 2014. **126**: p. 107-112.
66. Huang, Y.-C., et al., *A universal roll-to-roll slot-die coating approach towards high-efficiency organic photovoltaics.* Progress in Photovoltaics: Research and Applications, 2017. **25**(11): p. 928-935.
67. Zhao, Y., et al., *A Sequential Slot-Die Coated Ternary System Enables Efficient Flexible Organic Solar Cells.* Solar Rrl, 2019. **3**(3).
68. Meng, X.C., et al., *A General Approach for Lab-to-Manufacturing Translation on Flexible Organic Solar Cells.* Advanced Materials, 2019. **31**(41).

69. Wu, Q., et al., *Slot-die printed non-fullerene organic solar cells with the highest efficiency of 12.9% for low-cost PV-driven water splitting.* Nano Energy, 2019. **61**: p. 559-566.
70. Park, S.-Y., et al., *Spray-coated organic solar cells with large-area of 12.25cm2.* Solar Energy Materials and Solar Cells, 2011. **95**(3): p. 852-855.
71. Kang, J.-W., et al., *Fully spray-coated inverted organic solar cells.* Solar Energy Materials and Solar Cells, 2012. **103**: p. 76-79.
72. Wu, F., et al., *Morphology construction of vertical phase separation for large-area polymer solar cells.* Organic Electronics, 2015. **26**: p. 48-54.
73. Scarratt, N.W., et al., *Polymer-based solar cells having an active area of 1.6 cm(2) fabricated via spray coating.* Apl Materials, 2015. **3**(12).
74. Huang, Y.-C., et al., *Correlation between Hierarchical Structure and Processing Control of Large-area Spray-coated Polymer Solar Cells toward High Performance.* Scientific Reports, 2016. **6**: p. 20062.
75. Zhang, T., et al., *Fabricating high performance polymer photovoltaic modules by creating large-scale uniform films.* Organic Electronics, 2016. **32**: p. 126-133.
76. Cai, C., et al., *Polymer solar cells spray coated with non-halogenated solvents.* Solar Energy Materials and Solar Cells, 2017. **161**: p. 52-61.
77. Eggenhuisen, T.M., et al. *Organic photovoltaic cells with all inkjet printed layers and freedom of form*. in *2014 IEEE 40th Photovoltaic Specialist Conference (PVSC)*. 2014.
78. Eggenhuisen, T.M., et al., *High efficiency, fully inkjet printed organic solar cells with freedom of design.* Journal of Materials Chemistry A, 2015. **3**(14): p. 7255-7262.
79. Corzo, D., et al., *Digital Inkjet Printing of High-Efficiency Large-Area Nonfullerene Organic Solar Cells.* Advanced Materials Technologies, 2019. **4**(7).
80. Kang, Q., et al., *Printable MoOx Anode Interlayers for Organic Solar Cells.* Advanced Materials, 2018. **30**(35): p. 1801718.
81. Ben Dkhil, S., et al., *Square-Centimeter-Sized High-Efficiency Polymer Solar Cells: How the Processing Atmosphere and Film Quality Influence Performance at Large Scale.* Advanced Energy Materials, 2016. **6**(13).
82. Zhao, W.C., et al., *Fullerene-Free Polymer Solar Cells with over 11% Efficiency and Excellent Thermal Stability.* Advanced Materials, 2016. **28**(23): p. 4734-4739.
83. Cui, Y., et al., *Over 16% efficiency organic photovoltaic cells enabled by a chlorinated acceptor with increased open-circuit voltages.* Nature Communications, 2019. **10**.
84. Cui, Y., et al., *Single-Junction Organic Photovoltaic Cells with Approaching 18% Efficiency.* Advanced Materials, 2020. **32**(19): p. 1908205.
85. Cui, Y., et al., *Wide-gap non-fullerene acceptor enabling high-performance organic photovoltaic cells for indoor applications.* Nature Energy, 2019. **4**(9): p. 768-775.
86. Yun, J.H., et al., *Development of Highly Crystalline Donor–Acceptor-Type Random Polymers for High Performance Large-Area Organic Solar Cells.* Macromolecules, 2017. **50**(19): p. 7567-7576.
87. Shin, I., et al., *High-Performance and Uniform 1 cm2 Polymer Solar Cells with D1-A-D2-A-Type Random Terpolymers.* Advanced Energy Materials, 2018. **8**(7): p. 1701405.
88. Zhang, S., et al., *Over 14% Efficiency in Polymer Solar Cells Enabled by a Chlorinated Polymer Donor.* Advanced Materials, 2018. **30**(20): p. 1800868.
89. Fan, B., et al., *Fine-tuning of the chemical structure of photoactive materials for highly efficient organic photovoltaics.* Nature Energy, 2018. **3**(12): p. 1051-1058.
90. Cui, Y., et al., *Achieving Over 15% Efficiency in Organic Photovoltaic Cells via Copolymer Design.* Advanced Materials, 2019. **31**(14): p. 1808356.
91. Cui, C., et al., *High-Performance Organic Solar Cells Based on a Small Molecule with Alkylthio-Thienyl-Conjugated Side Chains without Extra Treatments.* Advanced Materials, 2015. **27**(45): p. 7469-7475.

92. Zhang, J., et al., *Enhancing Performance of Large-Area Organic Solar Cells with Thick Film via Ternary Strategy.* Small, 2017. **13**(21): p. 1700388.
93. Liu, S.Q., et al., *Printable and Large-Area Organic Solar Cells Enabled by a Ternary Pseudo-Planar Heterojunction Strategy.* Advanced Functional Materials.
94. Baran, D., et al., *Reducing the effciency-stability-cost gap of organic photovoltaics with highly effcient and stable small molecule acceptor ternary solar cells.* Nature Materials, 2017. **16**(3): p. 363-+.
95. Fan, B., et al., *Surpassing the 10% efficiency milestone for 1-cm2 all-polymer solar cells.* Nature Communications, 2019. **10**(1): p. 4100.
96. Xiao, X., K. Lee, and S.R. Forrest, *Scalability of multi-junction organic solar cells for large area organic solar modules.* Applied Physics Letters, 2015. **106**(21).
97. Kang, Q., et al., *A Printable Organic Cathode Interlayer Enables over 13% Efficiency for 1-cm(2) Organic Solar Cells.* Joule, 2019. **3**(1): p. 227-239.
98. Ji, G., et al., *12.88% efficiency in doctor-blade coated organic solar cells through optimizing the surface morphology of a ZnO cathode buffer layer.* Journal of Materials Chemistry A, 2019. **7**(1): p. 212-220.
99. Bai, Y.M., et al., *Novel cathode buffer layer of Al(acac)(3)enables efficient, large area and stable semi-transparent organic solar cells.* Materials Chemistry Frontiers, 2020. **4**(7): p. 2072-2080.
100. Huang, J., et al., *10.4% Power Conversion Efficiency of ITO-Free Organic Photovoltaics Through Enhanced Light Trapping Configuration.* Advanced Energy Materials, 2015. **5**(15).
101. Czolk, J., et al., *Highly Efficient, Mechanically Flexible, Semi-Transparent Organic Solar Cells Doctor Bladed from Non-Halogenated Solvents.* Advanced Materials Technologies, 2016. **1**(9).
102. Zhao, Y.F., et al., *Large-area, flexible polymer solar cell based on silver nanowires as transparent electrode by roll-to-roll printing.* Chinese Journal of Polymer Science, 2017. **35**(2): p. 261-268.
103. Berny, S., et al., *Solar Trees: First Large-Scale Demonstration of Fully Solution Coated, Semitransparent, Flexible Organic Photovoltaic Modules.* Advanced Science, 2016. **3**(5).
104. Steim, R., et al., *Organic photovoltaics for low light applications.* Solar Energy Materials and Solar Cells, 2011. **95**(12): p. 3256-3261.
105. Cui, Y., et al., *1 cm(2) Organic Photovoltaic Cells for Indoor Application with over 20% Efficiency.* Advanced Materials, 2019. **31**(42).
106. Salinas, J.-F., et al., *On the use of Woods metal for fabricating and testing polymeric organic solar cells: An easy and fast method.* Solar Energy Materials and Solar Cells, 2011. **95**(2): p. 595-601.
107. Pérez-Gutiérrez, E., et al., *Organic solar cells all made by blade and slot–die coating techniques.* Solar Energy, 2017. **146**: p. 79-84.
108. Barreiro-Argüelles, D., et al., *Stability study in organic solar cells based on PTB7:PC71BM and the scaling effect of the active layer.* Solar Energy, 2018. **163**: p. 510-518.
109. Liu, Y., et al., *All polymer photovoltaics: From small inverted devices to large roll-to-roll coated and printed solar cells.* Solar Energy Materials and Solar Cells, 2013. **112**: p. 157-162.
110. Angmo, D., et al., *Inkjet Printing of Back Electrodes for Inverted Polymer Solar Cells.* Advanced Energy Materials, 2013. **3**(9): p. 1230-1237.
111. Booth, H., *Laser Processing in Industrial Solar Module Manufacturing.* Journal of Laser Micro Nanoengineering, 2010. **5**(3): p. 183-191.
112. Sugioka, K. and Y. Cheng, *Ultrafast lasers-reliable tools for advanced materials processing.* Light-Science & Applications, 2014. **3**.

113. Sugioka, K., *Progress in ultrafast laser processing and future prospects.* Nanophotonics, 2017. **6**(2): p. 393-413.
114. Phillips, K.C., et al., *Ultrafast laser processing of materials: a review.* Advances in Optics and Photonics, 2015. **7**(4): p. 684-712.
115. Krebs, F.C., T. Tromholt, and M. Jørgensen, *Upscaling of polymer solar cell fabrication using full roll-to-roll processing.* Nanoscale, 2010. **2**(6): p. 873-886.
116. Lucera, L., et al., *Guidelines for Closing the Efficiency Gap between Hero Solar Cells and Roll-To-Roll Printed Modules.* Energy Technology, 2015. **3**(4): p. 373-384.
117. Krebs, F.C., et al., *Large area plastic solar cell modules.* Materials Science and Engineering: B, 2007. **138**(2): p. 106-111.
118. Tipnis, R., et al., *Large-area organic photovoltaic module—Fabrication and performance.* Solar Energy Materials and Solar Cells, 2009. **93**(4): p. 442-446.
119. Kubis, P., et al., *Patterning of organic photovoltaic modules by ultrafast laser.* Progress in Photovoltaics, 2015. **23**(2): p. 238-246.
120. Li, N., et al., *Towards large-scale production of solution-processed organic tandem modules based on ternary composites: Design of the intermediate layer, device optimization and laser based module processing.* Solar Energy Materials and Solar Cells, 2014. **120**: p. 701-708.
121. Kubis, P., et al., *High precision processing of flexible P3HT/PCBM modules with geometric fill factor over 95%.* Organic Electronics, 2014. **15**(10): p. 2256-2263.
122. Lucera, L., et al., *Highly efficient, large area, roll coated flexible and rigid OPV modules with geometric fill factors up to 98.5% processed with commercially available materials.* Energy & Environmental Science, 2016. **9**(1): p. 89-94.
123. Moorhouse, C., et al., *Laser Patterning of smart Nanomaterials for Reel-to-Reel production of Organic Photovoltaic (OPV) Devices.* Journal of Laser Micro Nanoengineering, 2015. **10**(2): p. 195-201.
124. Röttinger, S., et al., *Laser patterning of vacuum processed small molecular weight organic photovoltaics.* Solar Energy Materials and Solar Cells, 2016. **154**: p. 35-41.
125. Distler, A., C.J. Brabec, and H.-J. Egelhaaf, *Organic photovoltaic modules with new world record efficiencies.* Progress in Photovoltaics: Research and Applications, 2020. **n/a**(n/a).
126. Etxebarria, I., et al., *Surface treatment patterning of organic photovoltaic films for low-cost modules.* Organic Electronics, 2013. **14**(1): p. 430-435.
127. Tait, J.G., et al., *Electrical properties of patterned photoactive layers in organic photovoltaic modules.* Solar Energy Materials and Solar Cells, 2016. **144**: p. 493-499.
128. Agrawal, N., et al., *Efficient up-scaling of organic solar cells.* Solar Energy Materials and Solar Cells, 2016. **157**: p. 960-965.
129. Lee, J., et al., *Seamless polymer solar cell module architecture built upon self-aligned alternating interfacial layers.* Energy & Environmental Science, 2013. **6**(4): p. 1152-1157.
130. Hong, S., et al., *A series connection architecture for large-area organic photovoltaic modules with a 7.5% module efficiency.* Nature Communications, 2016. **7**: p. 10279.
131. Dong, S., et al., *Efficient organic-inorganic hybrid cathode interfacial layer enabled by polymeric dopant and its application in large-area polymer solar cells.* Science China-Chemistry, 2019. **62**(1): p. 67-73.
132. Tsai, P.-T., et al., *Large-area organic solar cells by accelerated blade coating.* Organic Electronics, 2015. **22**: p. 166-172.
133. Tsai, P.T., et al., *Toward Long-Term Stable and Efficient Large-Area Organic Solar Cells.* Chemsuschem, 2017. **10**(13): p. 2778-2787.
134. Wong, Y.Q., et al., *Efficient semitransparent organic solar cells with good color perception and good color rendering by blade coating.* Organic Electronics, 2017. **43**: p. 196-206.

135. Huang, K.-M., et al., *Highly efficient and stable organic solar cell modules processed by blade coating with 5.6% module efficiency and active area of 216 cm2.* Progress in Photovoltaics: Research and Applications, 2019. **27**(0): p. 264.
136. Tsai, C.Y., et al., *Large area organic photovoltaic modules fabricated on a 30 cm by 20 cm substrate with a power conversion efficiency of 9.5%.* Solar Energy Materials and Solar Cells, 2020. **218**.
137. Chen, S.-H., et al., *Large-area blade-coated organic solar cells processed from halogen-free solvent.* Organic Electronics, 2019. **75**: p. 105376.
138. Zhang, K., et al., *Efficient Large Area Organic Solar Cells Processed by Blade-Coating With Single-Component Green Solvent.* Solar RRL, 2018. **2**(1): p. 1700169.
139. Lim, S.-L., et al., *Efficient, large area organic photovoltaic modules with active layers processed with non-halogenated solvents in air.* Organic Electronics, 2017. **43**: p. 55-63.
140. Zhao, W.C., et al., *Vacuum-assisted annealing method for high efficiency printable large-area polymer solar cell modules.* Journal of Materials Chemistry C, 2019. **7**(11): p. 3206-3211.
141. Hanisch, J., et al., *Efficient polymer tandem modules and solar cells by doctor blading.* Journal of Materials Chemistry A, 2016. **4**(13): p. 4771-4775.
142. Kutsarov, D.I., et al., *Fabrication of air-stable, large-area, PCDTBT:PC70BM polymer solar cell modules using a custom built slot-die coater.* Solar Energy Materials and Solar Cells, 2017. **161**: p. 388-396.
143. Heo, Y.J., et al., *Small-Molecule Organic Photovoltaic Modules Fabricated via Halogen-Free Solvent System with Roll-to-Roll Compatible Scalable Printing Method.* Acs Applied Materials & Interfaces, 2017. **9**(45): p. 39519-39525.
144. Heo, Y.J., et al., *Printed Large-Area Photovoltaic Modules Based on Small Molecules with Different Alkyl Terminal Chains.* Acs Applied Energy Materials, 2019. **2**(12): p. 8885-8893.
145. Chang, Y.-M., et al., *All solution and ambient processable organic photovoltaic modules fabricated by slot-die coating and achieved a certified 7.56% power conversion efficiency.* Solar Energy Materials and Solar Cells, 2019. **202**: p. 110064.
146. Lee, J., et al., *Slot-Die and Roll-to-Roll Processed Single Junction Organic Photovoltaic Cells with the Highest Efficiency.* Advanced Energy Materials, 2019. **9**(36).
147. Vak, D., et al., *Reverse gravure coating for roll-to-roll production of organic photovoltaics.* Solar Energy Materials and Solar Cells, 2016. **149**: p. 154-161.
148. Mao, L., et al., *Writable and patternable organic solar cells and modules inspired by an old Chinese calligraphy tradition.* Materials Horizons, 2018. **5**(1): p. 123-130.
149. Sun, L.L., X.S. Jiang, and Y.H. Zhou, *Efficient nonfullerene organic solar cells with active layers fabricated by water transfer printing.* Journal of Energy Chemistry, 2019. **37**: p. 220-224.
150. Badgujar, S., et al., *High-Performance Small Molecule via Tailoring Intermolecular Interactions and its Application in Large-Area Organic Photovoltaic Modules.* Advanced Energy Materials, 2016. **6**(12).
151. Rasool, S., et al., *Room Temperature Processed Highly Efficient Large-Area Polymer Solar Cells Achieved with Molecular Engineering of Copolymers.* Advanced Energy Materials, 2019. **9**(21).
152. Liao, C.-Y., et al., *Processing Strategies for an Organic Photovoltaic Module with over 10% Efficiency.* Joule, 2020. **4**(1): p. 189-206.
153. Lee, T., et al., *Non-halogenated solvent-processed ternary-blend solar cells via alkyl-side-chain engineering of a non-fullerene acceptor and their application in large-area devices.* Journal of Materials Chemistry A, 2020. **8**(20): p. 10318-10330.
154. Dong, S., et al., *Single-Component Non-halogen Solvent-Processed High-Performance Organic Solar Cell Module with Efficiency over 14%.* Joule, 2020. **4**(9): p. 2004-2016.

155. Zhang, T., et al., *Efficient Non-Fullerene Organic Photovoltaic Modules Incorporating As-Cast and Thickness-Insensitive Photoactive Layers.* Advanced Energy Materials, 2018. **8**(25): p. 1801387.
156. Huang, K.M., et al., *Nonfullerene Polymer Solar Cell with Large Active Area of 216 cm(2) and High Power Conversion Efficiency of 7.7%.* Solar Rrl, 2019. **3**(8).
157. Lee, H.K.H., et al., *Is organic photovoltaics promising for indoor applications?* Applied Physics Letters, 2016. **108**(25).
158. Aoki, Y., *Photovoltaic performance of Organic Photovoltaics for indoor energy harvester.* Organic Electronics, 2017. **48**: p. 194-197.
159. Arai, R., et al., *High-Performance Organic Energy-Harvesting Devices and Modules for Self-Sustainable Power Generation under Ambient Indoor Lighting Environments.* Acs Applied Materials & Interfaces, 2019. **11**(9): p. 9259-9264.
160. Arai, R., et al., *Organic energy-harvesting devices achieving power conversion efficiencies over 20% under ambient indoor lighting.* Journal of Materials Chemistry A, 2019. **7**(35): p. 20187-20192.
161. Park, S., et al., *High-Performance and Stable Nonfullerene Acceptor-Based Organic Solar Cells for Indoor to Outdoor Light.* ACS Energy Letters, 2020. **5**(1): p. 170-179.
162. Krebs, F.C., *Polymer solar cell modules prepared using roll-to-roll methods: Knife-over-edge coating, slot-die coating and screen printing.* Solar Energy Materials and Solar Cells, 2009. **93**(4): p. 465-475.
163. Krebs, F.C., S.A. Gevorgyan, and J. Alstrup, *A roll-to-roll process to flexible polymer solar cells: model studies, manufacture and operational stability studies.* Journal of Materials Chemistry, 2009. **19**(30): p. 5442-5451.
164. Krebs, F.C., et al., *A round robin study of flexible large-area roll-to-roll processed polymer solar cell modules.* Solar Energy Materials and Solar Cells, 2009. **93**(11): p. 1968-1977.
165. Lewis, J.E., et al., *Over 30% transparency large area inverted organic solar array by spray.* Solar Energy Materials and Solar Cells, 2011. **95**(10): p. 2816-2822.
166. Galagan, Y., et al., *Roll-to-Roll Slot-Die Coated Organic Photovoltaic (OPV) Modules with High Geometrical Fill Factors.* Energy Technology, 2015. **3**(8): p. 834-842.
167. Guo, F., et al., *Nanowire Interconnects for Printed Large-Area Semitransparent Organic Photovoltaic Modules.* Advanced Energy Materials, 2015. **5**(12): p. 1401779.
168. Kapnopoulos, C., et al., *Fully gravure printed organic photovoltaic modules: A straightforward process with a high potential for large scale production.* Solar Energy Materials and Solar Cells, 2016. **144**: p. 724-731.
169. Park, S.-H., et al., *Large area roll-to-roll sputtering of transparent ITO/Ag/ITO cathodes for flexible inverted organic solar cell modules.* Organic Electronics, 2016. **30**: p. 112-121.
170. Weerasinghe, H.C., et al., *A stability study of roll-to-roll processed organic photovoltaic modules containing a polymeric electron-selective layer.* Solar Energy Materials and Solar Cells, 2016. **152**: p. 133-140.
171. Lucera, L., et al., *Printed semi-transparent large area organic photovoltaic modules with power conversion efficiencies of close to 5 %.* Organic Electronics, 2017. **45**: p. 209-214.
172. Huang, Y.C., et al., *All-Spray-Coated Inverted Semitransparent Organic Solar Cells and Modules.* Ieee Journal of Photovoltaics, 2018. **8**(1): p. 144-150.
173. Maisch, P., et al., *Shy Organic Photovoltaics: Digitally Printed Organic Solar Modules With Hidden Interconnects.* Solar RRL, 2018. **2**(7): p. 1800005.
174. Apilo, P., et al., *Fully Roll-to-Roll Printed P3HT/Indene-C60-Bisadduct Modules with High Open-Circuit Voltage and Efficiency.* Solar RRL, 2018. **2**(3): p. 1700160.

175. Strohm, S., et al., *P3HT: non-fullerene acceptor based large area, semi-transparent PV modules with power conversion efficiencies of 5%, processed by industrially scalable methods.* Energy & Environmental Science, 2018. **11**(8): p. 2225-2234.
176. Han, Y.W., et al., *Evaporation-Free Nonfullerene Flexible Organic Solar Cell Modules Manufactured by An All-Solution Process.* Advanced Energy Materials, 2019. **9**(42): p. 1902065.
177. Kubis, P., et al., *All sub-nanosecond laser monolithic interconnection of OPV modules.* Progress in Photovoltaics, 2019. **27**(6): p. 479-490.
178. Espinosa, N., et al., *A life cycle analysis of polymer solar cell modules prepared using roll-to-roll methods under ambient conditions.* Solar Energy Materials and Solar Cells, 2011. **95**(5): p. 1293-1302.
179. Emmott, C.J.M., A. Urbina, and J. Nelson, *Environmental and economic assessment of ITO-free electrodes for organic solar cells.* Solar Energy Materials and Solar Cells, 2012. **97**: p. 14-21.
180. Espinosa, N., R. Garcia-Valverde, and F.C. Krebs, *Life-cycle analysis of product integrated polymer solar cells.* Energy & Environmental Science, 2011. **4**(5): p. 1547-1557.
181. Espinosa, N., et al., *Life cycle assessment of ITO-free flexible polymer solar cells prepared by roll-to-roll coating and printing.* Solar Energy Materials and Solar Cells, 2012. **97**: p. 3-13.
182. Azzopardi, B., et al., *Economic assessment of solar electricity production from organic-based photovoltaic modules in a domestic environment.* Energy & Environmental Science, 2011. **4**(10): p. 3741-3753.
183. Inganas, O., *Organic Photovoltaics Avoiding indium.* Nature Photonics, 2011. **5**(4): p. 201-202.
184. Hösel, M., et al., *High-Volume Processed, ITO-Free Superstrates and Substrates for Roll-to-Roll Development of Organic Electronics.* Advanced Science, 2014. **1**(1): p. 1400002.
185. Kulkarni, G.U., et al., *Towards low cost materials and methods for transparent electrodes.* Current Opinion in Chemical Engineering, 2015. **8**: p. 60-68.
186. Lu, S.D., et al., *Recent Development in ITO-free Flexible Polymer Solar Cells.* Polymers, 2018. **10**(1).
187. Guo, W., et al., *Recent Development of Transparent Conducting Oxide-Free Flexible Thin-Film Solar Cells.* Advanced Functional Materials, 2016. **26**(48): p. 8855-8884.
188. Zhang, Y.K., et al., *Solution-Processed Transparent Electrodes for Emerging Thin-Film Solar Cells.* Chemical Reviews, 2020. **120**(4): p. 2049-2122.
189. Li, Y.W., et al., *Flexible and Semitransparent Organic Solar Cells.* Advanced Energy Materials, 2018. **8**(7).
190. Azani, M.R., A. Hassanpour, and T. Torres, *Benefits, Problems, and Solutions of Silver Nanowire Transparent Conductive Electrodes in Indium Tin Oxide (ITO)-Free Flexible Solar Cells.* Advanced Energy Materials, 2020. **10**(48).
191. Zilberberg, K. and T. Riedl, *Metal-nanostructures - a modern and powerful platform to create transparent electrodes for thin-film photovoltaics.* Journal of Materials Chemistry A, 2016. **4**(38): p. 14481-14508.
192. Yun, J., *Ultrathin Metal films for Transparent Electrodes of Flexible Optoelectronic Devices.* Advanced Functional Materials, 2017. **27**(18).
193. Cheknane, A., et al., *Minimization of the effect of the collecting grid in a solar cell based silicon.* Solar Energy Materials and Solar Cells, 2005. **87**(1): p. 557-565.
194. Cheknane, A., *Optimal design of electrode grids dimensions for ITO-free organic photovoltaic devices.* Progress in Photovoltaics, 2011. **19**(2): p. 155-159.
195. Tvingstedt, K. and O. Inganäs, *Electrode Grids for ITO Free Organic Photovoltaic Devices.* Advanced Materials, 2007. **19**(19): p. 2893-2897.

196. Galagan, Y., et al., *Current Collecting Grids for ITO-Free Solar Cells.* Advanced Energy Materials, 2012. **2**(1): p. 103-110.
197. Kang, M.-G., et al., *Organic Solar Cells Using Nanoimprinted Transparent Metal Electrodes.* Advanced Materials, 2008. **20**(23): p. 4408-4413.
198. Yu, J.-S., et al., *Silver front electrode grids for ITO-free all printed polymer solar cells with embedded and raised topographies, prepared by thermal imprint, flexographic and inkjet roll-to-roll processes.* Nanoscale, 2012. **4**(19): p. 6032-6040.
199. Angmo, D., et al., *Roll-to-Roll Inkjet Printing and Photonic Sintering of Electrodes for ITO Free Polymer Solar Cell Modules and Facile Product Integration.* Advanced Energy Materials, 2013. **3**(2): p. 172-175.
200. Gupta, R., et al., *Solution processed large area fabrication of Ag patterns as electrodes for flexible heaters, electrochromics and organic solar cells.* Journal of Materials Chemistry A, 2014. **2**(28): p. 10930-10937.
201. Carlé, J.E., et al., *A laboratory scale approach to polymer solar cells using one coating/printing machine, flexible substrates, no ITO, no vacuum and no spincoating.* Solar Energy Materials and Solar Cells, 2013. **108**: p. 126-128.
202. Hösel, M., et al., *Comparison of Fast Roll-to-Roll Flexographic, Inkjet, Flatbed, and Rotary Screen Printing of Metal Back Electrodes for Polymer Solar Cells.* Advanced Engineering Materials, 2013. **15**(10): p. 995-1001.
203. Dam, H.F., et al., *Roll and roll-to-roll process scaling through development of a compact flexo unit for printing of back electrodes.* Solar Energy Materials and Solar Cells, 2015. **140**: p. 187-192.
204. Andersen, T.R., et al., *A rational method for developing and testing stable flexible indium- and vacuum-free multilayer tandem polymer solar cells comprising up to twelve roll processed layers.* Solar Energy Materials and Solar Cells, 2014. **120**: p. 735-743.
205. Zawacka, N.K., et al., *The influence of additives on the morphology and stability of roll-to-roll processed polymer solar cells studied through ex situ and in situ X-ray scattering.* Journal of Materials Chemistry A, 2014. **2**(43): p. 18644-18654.
206. Larsen-Olsen, T.T., et al., *A round robin study of polymer solar cells and small modules across China.* Solar Energy Materials and Solar Cells, 2013. **117**: p. 382-389.
207. Angmo, D., et al., *Scalability and stability of very thin, roll-to-roll processed, large area, indium-tin-oxide free polymer solar cell modules.* Organic Electronics, 2013. **14**(3): p. 984-994.
208. Hösel, M., et al., *Fast Inline Roll-to-Roll Printing for Indium-Tin-Oxide-Free Polymer Solar Cells Using Automatic Registration.* Energy Technology, 2013. **1**(1): p. 102-107.
209. Carle, J.E., et al., *Upscaling from single cells to modules - fabrication of vacuum- and ITO-free polymer solar cells on flexible substrates with long lifetime.* Journal of Materials Chemistry C, 2014. **2**(7): p. 1290-1297.
210. Kato, Y., et al., *Electrical and optical properties of transparent flexible electrodes: Effects of UV ozone and oxygen plasma treatments.* Organic Electronics, 2014. **15**(3): p. 721-728.
211. InfinityPV. *Flextrodes*. [2020-03-16]; Available from: https://infinitypv.com/products/materials/flextrode.
212. Carle, J.E., et al., *A comparative study of fluorine substituents for enhanced stability of flexible and ITO-free high-performance polymer solar cells.* Journal of Polymer Science Part B-Polymer Physics, 2014. **52**(13): p. 893-899.
213. Chen, M.-R., et al., *Solvent-resistant small molecule solar cells by roll-to-roll fabrication via introduction of azide cross-linkable group.* Synthetic Metals, 2014. **195**: p. 299-305.
214. Andersen, T.R., et al., *Medium area, flexible single and tandem junction solar cells based on roll coated semi-random copolymers.* Journal of Materials Chemistry C, 2014. **2**(44): p. 9412-9415.

215. Brandt, R.G., et al., *An isoindigo containing donor–acceptor polymer: synthesis and photovoltaic properties of all-solution-processed ITO- and vacuum-free large area roll-coated single junction and tandem solar cells.* Journal of Materials Chemistry C, 2015. **3**(8): p. 1633-1639.
216. Helgesen, M., J.E. Carlé, and F.C. Krebs, *Slot-Die Coating of a High Performance Copolymer in a Readily Scalable Roll Process for Polymer Solar Cells.* Advanced Energy Materials, 2013. **3**(12): p. 1664-1669.
217. Liu, W.Q., et al., *Roll-coating fabrication of flexible large area small molecule solar cells with power conversion efficiency exceeding 1%.* Journal of Materials Chemistry A, 2014. **2**(46): p. 19809-19814.
218. Cheng, P., et al., *Roll-Coated Fabrication of Fullerene-Free Organic Solar Cells with Improved Stability.* Advanced Science, 2015. **2**(6).
219. Liu, K., et al., *Roll-coating fabrication of flexible organic solar cells: comparison of fullerene and fullerene-free systems.* Journal of Materials Chemistry A, 2016. **4**(3): p. 1044-1051.
220. Cheng, P., et al., *Comparison of additive amount used in spin-coated and roll-coated organic solar cells.* Journal of Materials Chemistry A, 2014. **2**(45): p. 19542-19549.
221. Andersen, T.R., et al., *Scalable, ambient atmosphere roll-to-roll manufacture of encapsulated large area, flexible organic tandem solar cell modules.* Energy & Environmental Science, 2014. **7**(9): p. 2925-2933.
222. Galagan, Y., et al., *ITO-free flexible organic solar cells with printed current collecting grids.* Solar Energy Materials and Solar Cells, 2011. **95**(5): p. 1339-1343.
223. Galagan, Y., et al., *Evaluation of ink-jet printed current collecting grids and busbars for ITO-free organic solar cells.* Solar Energy Materials and Solar Cells, 2012. **104**: p. 32-38.
224. Li, Y., et al., *Ambient stable large-area flexible organic solar cells using silver grid hybrid with vapor phase polymerized poly(3,4-Ethylenedioxythiophene) cathode.* Solar Energy Materials and Solar Cells, 2015. **143**: p. 354-359.
225. Mao, L., et al., *Flexible silver grid/PEDOT:PSS hybrid electrodes for large area inverted polymer solar cells.* Nano Energy, 2014. **10**: p. 259-267.
226. Li, Y., et al., *ITO-free photovoltaic cell utilizing a high-resolution silver grid current collecting layer.* Solar Energy Materials and Solar Cells, 2013. **113**: p. 85-89.
227. Andersen, T.R., et al., *Fully roll-to-roll prepared organic solar cells in normal geometry with a sputter-coated aluminium top-electrode.* Solar Energy Materials and Solar Cells, 2016. **149**: p. 103-109.
228. Jin, W.Y., et al., *Ultra-Smooth, Fully Solution-Processed Large-Area Transparent Conducting Electrodes for Organic Devices.* Scientific Reports, 2016. **6**.
229. Lu, S., et al., *Large area flexible polymer solar cells with high efficiency enabled by imprinted Ag grid and modified buffer layer.* Acta Materialia, 2017. **130**: p. 208-214.
230. Helgesen, M., et al., *Making Ends Meet: Flow Synthesis as the Answer to Reproducible High-Performance Conjugated Polymers on the Scale that Roll-to-Roll Processing Demands.* Advanced Energy Materials, 2015. **5**(9): p. 1401996.
231. Fan, Q.P., et al., *High-Performance As-Cast Nonfullerene Polymer Solar Cells with Thicker Active Layer and Large Area Exceeding 11% Power Conversion Efficiency.* Advanced Materials, 2018. **30**(6).
232. Kang, M.G., et al., *Transparent Cu nanowire mesh electrode on flexible substrates fabricated by transfer printing and its application in organic solar cells.* Solar Energy Materials and Solar Cells, 2010. **94**(6): p. 1179-1184.
233. Zhou, W.X., et al., *Copper Mesh Templated by Breath-Figure Polymer Films as Flexible Transparent Electrodes for Organic Photovoltaic Devices.* Acs Applied Materials & Interfaces, 2016. **8**(17): p. 11122-11127.
234. Georgiou, E., et al., *Printed Copper Nanoparticle Metal Grids for Cost-Effective ITO-Free Solution Processed Solar Cells.* Solar Rrl, 2018. **2**(3).

235. Choi, S., et al., *ITO-free large-area flexible organic solar cells with an embedded metal grid.* Organic Electronics, 2015. **17**: p. 349-354.
236. Galagan, Y., et al., *Scaling Up ITO-Free Solar Cells.* Advanced Energy Materials, 2014. **4**(2): p. 1300498.
237. Eggenhuisen, T.M., et al., *Digital fabrication of organic solar cells by Inkjet printing using non-halogenated solvents.* Solar Energy Materials and Solar Cells, 2015. **134**: p. 364-372.
238. Han, Y.F., et al., *Efficiency above 12% for 1 cm(2) Flexible Organic Solar Cells with Ag/Cu Grid Transparent Conducting Electrode.* Advanced Science, 2019. **6**(22).
239. Lee, J.Y., et al., *Solution-processed metal nanowire mesh transparent electrodes.* Nano Letters, 2008. **8**(2): p. 689-692.
240. Hu, L., et al., *Scalable Coating and Properties of Transparent, Flexible, Silver Nanowire Electrodes.* ACS Nano, 2010. **4**(5): p. 2955-2963.
241. Gaynor, W., et al., *Smooth Nanowire/Polymer Composite Transparent Electrodes.* Advanced Materials, 2011. **23**(26): p. 2905-2910.
242. Leem, D.-S., et al., *Efficient Organic Solar Cells with Solution-Processed Silver Nanowire Electrodes.* Advanced Materials, 2011. **23**(38): p. 4371-4375.
243. Yang, L., et al., *Solution-Processed Flexible Polymer Solar Cells with Silver Nanowire Electrodes.* ACS Applied Materials & Interfaces, 2011. **3**(10): p. 4075-4084.
244. Yu, Z.B., et al., *Silver Nanowire-Polymer Composite Electrodes for Efficient Polymer Solar Cells.* Advanced Materials, 2011. **23**(38): p. 4453-+.
245. Song, M., et al., *Highly Efficient and Bendable Organic Solar Cells with Solution-Processed Silver Nanowire Electrodes.* Advanced Functional Materials, 2013. **23**(34): p. 4177-4184.
246. Krantz, J., et al., *Solution-Processed Metallic Nanowire Electrodes as Indium Tin Oxide Replacement for Thin-Film Solar Cells.* Advanced Functional Materials, 2011. **21**(24): p. 4784-4787.
247. Basarir, F., et al., *Recent progresses on solution-processed silver nanowire based transparent conducting electrodes for organic solar cells.* Materials Today Chemistry, 2017. **3**: p. 60-72.
248. Langley, D., et al., *Flexible transparent conductive materials based on silver nanowire networks: a review.* Nanotechnology, 2013. **24**(45).
249. Angmo, D., et al., *Roll-to-Roll Printed Silver Nanowire Semitransparent Electrodes for Fully Ambient Solution-Processed Tandem Polymer Solar Cells.* Advanced Functional Materials, 2015. **25**(28): p. 4539-4547.
250. Maisch, P., et al., *Inkjet printed silver nanowire percolation networks as electrodes for highly efficient semitransparent organic solar cells.* Organic Electronics, 2016. **38**: p. 139-143.
251. Benatto, G.A.D., et al., *Roll-to-roll printed silver nanowires for increased stability of flexible ITO-free organic solar cell modules.* Nanoscale, 2016. **8**(1): p. 318-326.
252. Sun, L.L., et al., *Flexible All-Solution-Processed Organic Solar Cells with High-Performance Nonfullerene Active Layers.* Advanced Materials, 2020. **32**(14).
253. Mayousse, C., et al., *Stability of silver nanowire based electrodes under environmental and electrical stresses.* Nanoscale, 2015. **7**(5): p. 2107-2115.
254. Khaligh, H.H. and I.A. Goldthorpe, *Failure of silver nanowire transparent electrodes under current flow.* Nanoscale Research Letters, 2013. **8**.
255. Lin, C.C., D.X. Lin, and S.H. Lin, *Degradation problem in silver nanowire transparent electrodes caused by ultraviolet exposure.* Nanotechnology, 2020. **31**(21).
256. Rathmell, A.R. and B.J. Wiley, *The Synthesis and Coating of Long, Thin Copper Nanowires to Make Flexible, Transparent Conducting Films on Plastic Substrates.* Advanced Materials, 2011. **23**(41): p. 4798-+.

257. Guo, H.Z., et al., *Copper Nanowires as Fully Transparent Conductive Electrodes.* Scientific Reports, 2013. **3**.
258. Sachse, C., et al., *ITO-Free, Small-Molecule Organic Solar Cells on Spray-Coated Copper-Nanowire-Based Transparent Electrodes.* Advanced Energy Materials, 2014. **4**(2).
259. Chen, J.Y., et al., *Solution-processed copper nanowire flexible transparent electrodes with PEDOT:PSS as binder, protector and oxide-layer scavenger for polymer solar cells.* Nano Research, 2015. **8**(3): p. 1017-1025.
260. Bi, Y.G., et al., *Ultrathin Metal Films as the Transparent Electrode in ITO-Free Organic Optoelectronic Devices.* Advanced Optical Materials, 2019. **7**(6).
261. Angmo, D., M. Hösel, and F.C. Krebs, *All solution processing of ITO-free organic solar cell modules directly on barrier foil.* Solar Energy Materials and Solar Cells, 2012. **107**: p. 329-336.
262. Stec, H.M. and R.A. Hatton, *Widely Applicable Coinage Metal Window Electrodes on Flexible Polyester Substrates Applied to Organic Photovoltaics.* ACS Applied Materials & Interfaces, 2012. **4**(11): p. 6013-6020.
263. Du Pasquier, A., et al., *Conducting and transparent single-wall carbon nanotube electrodes for polymer-fullerene solar cells.* Applied Physics Letters, 2005. **87**(20): p. 203511.
264. Jeon, I., et al., *Single-Walled Carbon Nanotubes in Emerging Solar Cells: Synthesis and Electrode Applications.* Advanced Energy Materials, 2019. **9**(23).
265. Khan, D., et al., *A Review of the Challenges and Possibilities of Using Carbon Nanotubes in Organic Solar Cells.* Science of Advanced Materials, 2018. **10**(6): p. 747-760.
266. Obaidullah, M., V. Esat, and C. Sabah, *Single- and multi-walled carbon nanotubes for solar cell applications.* International Journal of Modern Physics B, 2018. **32**(21).
267. Jeon, I., Y. Matsuo, and S. Maruyama, *Single-Walled Carbon Nanotubes in Solar Cells.* Topics in Current Chemistry, 2018. **376**(1).
268. Yu, L.P., C. Shearer, and J. Shapter, *Recent Development of Carbon Nanotube Transparent Conductive Films.* Chemical Reviews, 2016. **116**(22): p. 13413-13453.
269. Zhou, Y. and R. Azumi, *Carbon nanotube based transparent conductive films: progress, challenges, and perspectives.* Science and Technology of Advanced Materials, 2016. **17**(1): p. 493-516.
270. Du, J.H., et al., *25th Anniversary Article: Carbon Nanotube- and Graphene- Based Transparent Conductive Films for Optoelectronic Devices.* Advanced Materials, 2014. **26**(13): p. 1958-1991.
271. Lee, K.T., et al., *Graphene- and Carbon-Nanotube-Based Transparent Electrodes for Semitransparent Solar Cells.* Materials, 2018. **11**(9).
272. Shastry, T.A. and M.C. Hersam, *Carbon Nanotubes in Thin-Film Solar Cells.* Advanced Energy Materials, 2017. **7**(10).
273. Tenent, R.C., et al., *Ultrasmooth, Large-Area, High-Uniformity, Conductive Transparent Single-Walled-Carbon-Nanotube Films for Photovoltaics Produced by Ultrasonic Spraying.* Advanced Materials, 2009. **21**(31): p. 3210-3216.
274. Yin, Z.Y., et al., *Graphene-Based Materials for Solar Cell Applications.* Advanced Energy Materials, 2014. **4**(1).
275. Mustonen, P., D.M.A. Mackenzie, and H. Lipsanen, *Review of fabrication methods of large-area transparent graphene electrodes for industry.* Frontiers of Optoelectronics, 2020. **13**(2): p. 91-113.
276. Wu, J., et al., *Organic solar cells with solution-processed graphene transparent electrodes.* Applied Physics Letters, 2008. **92**(26): p. 263302.
277. Tiwari, S., A. Purabgola, and B. Kandasubramanian, *Functionalised graphene as flexible electrodes for polymer photovoltaics.* Journal of Alloys and Compounds, 2020. **825**.
278. Chen, Y., et al., *Graphene as a Transparent and Conductive Electrode for Organic Optoelectronic Devices.* Advanced Electronic Materials, 2019. **5**(10): p. 1900247.

279. Tan, R.K.L., et al., *Graphene as a flexible electrode: review of fabrication approaches.* Journal of Materials Chemistry A, 2017. **5**(34): p. 17777-17803.
280. Garg, R., et al., *Deposition Methods of Graphene as Electrode Material for Organic Solar Cells.* Advanced Energy Materials, 2017. **7**(10).
281. Jo, J.W., J.U. Lee, and W.H. Jo, *Graphene-based electrodes for flexible electronics.* Polymer International, 2015. **64**(12): p. 1676-1684.
282. Manzano-Ramirez, A., et al., *A Review on the Efficiency of Graphene-Based BHJ Organic Solar Cells.* Journal of Nanomaterials, 2015.
283. Huang, X., et al., *Graphene-Based Electrodes.* Advanced Materials, 2012. **24**(45): p. 5979-6004.
284. He, M., et al., *Graphene-based transparent flexible electrodes for polymer solar cells.* Journal of Materials Chemistry, 2012. **22**(46): p. 24254-24264.
285. De Arco, L.G., et al., *Continuous, Highly Flexible, and Transparent Graphene Films by Chemical Vapor Deposition for Organic Photovoltaics.* Acs Nano, 2010. **4**(5): p. 2865-2873.
286. Backes, C., et al., *Production and processing of graphene and related materials.* 2d Materials, 2020. **7**(2).
287. Wang, Y., et al., *Interface Engineering of Layer-by-Layer Stacked Graphene Anodes for High-Performance Organic Solar Cells.* Advanced Materials, 2011. **23**(13): p. 1514-1518.
288. Park, H., et al., *Flexible Graphene Electrode-Based Organic Photovoltaics with Record-High Efficiency.* Nano Letters, 2014. **14**(9): p. 5148-5154.
289. Song, Y., et al., *Visibly-Transparent Organic Solar Cells on Flexible Substrates with All-Graphene Electrodes.* Advanced Energy Materials, 2016. **6**(20): p. 1600847.
290. Liu, Z., et al., *Neutral-Color Semitransparent Organic Solar Cells with All-Graphene Electrodes.* ACS Nano, 2015. **9**(12): p. 12026-12034.
291. Konios, D., et al., *Reduced Graphene Oxide Micromesh Electrodes for Large Area, Flexible, Organic Photovoltaic Devices.* Advanced Functional Materials, 2015. **25**(15): p. 2213-2221.
292. La Notte, L., et al., *Sprayed organic photovoltaic cells and mini-modules based on chemical vapor deposited graphene as transparent conductive electrode.* Carbon, 2018. **129**: p. 878-883.
293. Jiang, Y., T. Liu, and Y. Zhou, *Recent Advances of Synthesis, Properties, Film Fabrication Methods, Modifications of Poly(3,4-ethylenedioxythiophene), and Applications in Solution-Processed Photovoltaics.* Advanced Functional Materials. **n/a**(n/a): p. 2006213.
294. Hu, L., et al., *Research Progress on Polymer Solar Cells Based on PEDOT:PSS Electrodes.* Polymers, 2020. **12**(1).
295. Aernouts, T., et al., *Printable anodes for flexible organic solar cell modules.* Thin Solid Films, 2004. **451**: p. 22-25.
296. Chang, Y.M., L. Wang, and W.F. Su, *Polymer solar cells with poly(3,4-ethylenedioxythiophene) as transparent anode.* Organic Electronics, 2008. **9**(6): p. 968-973.
297. Hau, S.K., et al., *Indium tin oxide-free semi-transparent inverted polymer solar cells using conducting polymer as both bottom and top electrodes.* Organic Electronics, 2009. **10**(7): p. 1401-1407.
298. Kim, Y.H., et al., *Highly Conductive PEDOT:PSS Electrode with Optimized Solvent and Thermal Post-Treatment for ITO-Free Organic Solar Cells.* Advanced Functional Materials, 2011. **21**(6): p. 1076-1081.
299. Jung, S., et al., *All-Inkjet-Printed, All-Air-Processed Solar Cells.* Advanced Energy Materials, 2014. **4**(14).

300. Tan, L.C., et al., *High conductive PEDOT via post-treatment by halobenzoic for high-efficiency ITO-free and transporting layer-free organic solar cells.* Organic Electronics, 2016. **33**: p. 316-323.
301. Wang, X., et al., *Flexible ITO-Free Organic Photovoltaics on Ultra-Thin Flexible Glass Substrates with High Efficiency and Improved Stability.* Solar RRL, 2019. **3**(4): p. 1800286.
302. Krebs, F.C., *Roll-to-roll fabrication of monolithic large-area polymer solar cells free from indium-tin-oxide.* Solar Energy Materials and Solar Cells, 2009. **93**(9): p. 1636-1641.
303. Angmo, D., et al., *All-Solution-Processed, Ambient Method for ITO-Free, Roll-Coated Tandem Polymer Solar Cells using Solution-Processed Metal Films.* Energy Technology, 2014. **2**(7): p. 651-659.
304. Zuo, L.J., et al., *Toward Highly Efficient Large-Area ITO-Free Organic Solar Cells with a Conductance-Gradient Transparent Electrode.* Advanced Materials, 2015. **27**(43): p. 6983-+.
305. Zuo, L., et al., *Design of charge transporting grids for efficient ITO-free flexible up-scaled organic photovoltaics.* Materials Chemistry Frontiers, 2017. **1**(2): p. 304-309.
306. Koppitz, M., et al., *Organic Solar Modules: Fully Doctor Bladed on Glass in Air.* Energy Technology, 2017. **5**(7): p. 1105-1111.
307. Lin, Y., et al., *Printed Nonfullerene Organic Solar Cells with the Highest Efficiency of 9.5%.* Advanced Energy Materials, 2018. **8**(13): p. 1701942.
308. Lin, Y., et al., *Energy-effectively printed all-polymer solar cells exceeding 8.61% efficiency.* Nano Energy, 2018. **46**: p. 428-435.
309. Liu, A., et al., *Manipulate Micrometer Surface and Nanometer Bulk Phase Separation Structures in the Active Layer of Organic Solar Cells via Synergy of Ultrasonic and High-Pressure Gas Spraying.* ACS Applied Materials & Interfaces, 2019. **11**(11): p. 10777-10784.
310. Jiang, X., et al., *10 cm2 nonfullerene solar cells with efficiency over 10% using HxMoO3-assisted growth of silver electrodes with a low threshold thickness of 4 nm.* Journal of Materials Chemistry A, 2020. **8**(1): p. 69-76.
311. Jin, H., et al., *Efficient, Large Area ITO-and-PEDOT-free Organic Solar Cell Sub-modules.* Advanced Materials, 2012. **24**(19): p. 2572-2577.
312. Hambsch, M., et al., *Improved stability of non-ITO stacked electrodes for large area flexible organic solar cells.* Solar Energy Materials and Solar Cells, 2014. **130**: p. 182-190.
313. Ibraikulov, O.A., et al., *ITO-Free Organic Photovoltaic Modules Based on Fluorinated Polymers Deposited from Non-Halogenated Solution: A Major Step Toward Large-Scale Module Production.* Solar Rrl.
314. Manceau, M., et al., *ITO-free flexible polymer solar cells: From small model devices to roll-to-roll processed large modules.* Organic Electronics, 2011. **12**(4): p. 566-574.
315. Galagan, Y., et al., *Large area ITO-free organic solar cells on steel substrate.* Organic Electronics, 2012. **13**(12): p. 3310-3314.
316. Sapkota, S.B., et al., *Promising long-term stability of encapsulated ITO-free bulk-heterojunction organic solar cells under different aging conditions.* Solar Energy Materials and Solar Cells, 2014. **130**: p. 144-150.
317. Mao, L., et al. *Movie of sunlight powering a toy electric car with OPV*. 2017; Available from: http://www.rsc.org/suppdata/c6/ta/c6ta10106b/c6ta10106b2.mp4.
318. Du, X., et al., *Efficient Polymer Solar Cells Based on Non-fullerene Acceptors with Potential Device Lifetime Approaching 10 Years.* Joule, 2019. **3**(1): p. 215-226.
319. Xu, X., et al., *Interface-enhanced organic solar cells with extrapolated T-80 lifetimes of over 20 years.* Science Bulletin, 2020. **65**(3): p. 208-216.

320. Grossiord, N., et al., *Degradation mechanisms in organic photovoltaic devices.* Organic Electronics, 2012. **13**(3): p. 432-456.
321. Cheng, P. and X. Zhan, *Stability of organic solar cells: challenges and strategies.* Chemical Society Reviews, 2016. **45**(9): p. 2544-2582.
322. Jørgensen, M., K. Norrman, and F.C. Krebs, *Stability/degradation of polymer solar cells.* Solar Energy Materials and Solar Cells, 2008. **92**(7): p. 686-714.
323. Rafique, S., et al., *Fundamentals of bulk heterojunction organic solar cells: An overview of stability/degradation issues and strategies for improvement.* Renewable & Sustainable Energy Reviews, 2018. **84**: p. 43-53.
324. Cao, H.Q., et al., *Recent progress in degradation and stabilization of organic solar cells.* Journal of Power Sources, 2014. **264**: p. 168-183.
325. Fraga Domínguez, I., A. Distler, and L. Lüer, *Stability of Organic Solar Cells: The Influence of Nanostructured Carbon Materials.* Advanced Energy Materials, 2017. **7**(10): p. 1601320.
326. Speller, E.M., et al., *From fullerene acceptors to non-fullerene acceptors: prospects and challenges in the stability of organic solar cells.* Journal of Materials Chemistry A, 2019. **7**(41): p. 23361-23377.
327. Lee, E.K., et al., *Toward Environmentally Robust Organic Electronics: Approaches and Applications.* Advanced Materials, 2017. **29**(44).
328. Duan, L.P. and A. Uddin, *Progress in Stability of Organic Solar Cells.* Advanced Science, 2020. **7**(11).
329. Jorgensen, M., et al., *Stability of Polymer Solar Cells.* Advanced Materials, 2012. **24**(5): p. 580-612.
330. Wang, Y.W., et al., *Efficient and stable operation of nonfullerene organic solar cells: retaining a high built-in potential.* Journal of Materials Chemistry A, 2020. **8**(40): p. 21255-21264.
331. Wang, Y.M., et al., *Light-induced degradation of fullerenes in organic solar cells: a case study on TQ1:PC71BM.* Journal of Materials Chemistry A, 2018. **6**(25): p. 11884-11889.
332. Lee, H.K.H., et al., *The role of fullerenes in the environmental stability of polymer:fullerene solar cells.* Energy & Environmental Science, 2018. **11**(2): p. 417-428.
333. Huang, Y.-C., et al., *Mechanistic Insights into the Effect of Polymer Regioregularity on the Thermal Stability of Polymer Solar Cells.* ACS Applied Materials & Interfaces, 2019. **11**(43): p. 40310-40319.
334. Schaffer, C.J., et al., *A Direct Evidence of Morphological Degradation on a Nanometer Scale in Polymer Solar Cells.* Advanced Materials, 2013. **25**(46): p. 6760-6764.
335. Boldrighini, P., et al., *Optical calcium test for measurement of multiple permeation pathways in flexible organic optoelectronic encapsulation.* Review of Scientific Instruments, 2019. **90**(1): p. 014710.
336. Wang, X.Z., et al., *Degradation mechanisms in organic solar cells: Localized moisture encroachment and cathode reaction.* Solar Energy Materials and Solar Cells, 2012. **104**: p. 1-6.
337. Drakonakis, V.M., et al., *Investigating electrodes degradation in organic photovoltaics through reverse engineering under accelerated humidity lifetime conditions.* Solar Energy Materials and Solar Cells, 2014. **130**: p. 544-550.
338. Hösel, M., et al., *Failure Modes and Fast Repair Procedures in High Voltage Organic Solar Cell Installations.* Advanced Energy Materials, 2014. **4**(7): p. 1301625.
339. Gevorgyan, S.A., et al., *Improving, characterizing and predicting the lifetime of organic photovoltaics.* Journal of Physics D-Applied Physics, 2017. **50**(10).
340. Doumon, N.Y., et al., *Relating polymer chemical structure to the stability of polymer:fullerene solar cells.* Journal of Materials Chemistry C, 2017. **5**(26): p. 6611-6619.

341. Kong, J., et al., *Long-term stable polymer solar cells with significantly reduced burn-in loss.* Nature Communications, 2014. **5**.
342. Li, Z., et al., *Morphology optimization via molecular weight tuning of donor polymer enables all-polymer solar cells with simultaneously improved performance and stability.* Nano Energy, 2019. **64**: p. 103931.
343. Shi, M.M., et al., *The Intrinsic Role of Molecular Mass and Polydispersity Index in High-Performance Non-Fullerene Polymer Solar Cells.* Advanced Energy Materials, 2021. **11**: p. 2002709.
344. Li, S.X., et al., *An Unfused-Core-Based Nonfullerene Acceptor Enables High-Efficiency Organic Solar Cells with Excellent Morphological Stability at High Temperatures.* Advanced Materials, 2018. **30**(6).
345. Li, S., et al., *A spirobifluorene and diketopyrrolopyrrole moieties based non-fullerene acceptor for efficient and thermally stable polymer solar cells with high open-circuit voltage.* Energy & Environmental Science, 2016. **9**(2): p. 604-610.
346. Holliday, S., et al., *High-efficiency and air-stable P3HT-based polymer solar cells with a new non-fullerene acceptor.* Nature Communications, 2016. **7**(1): p. 11585.
347. Cha, H.J., et al., *An Efficient, "Burn in" Free Organic Solar Cell Employing a Nonfullerene Electron Acceptor.* Advanced Materials, 2017. **29**(33).
348. Kim, G.-U., et al., *Triad-type, multi-functional compatibilizers for enhancing efficiency, stability and mechanical robustness of polymer solar cells.* Journal of Materials Chemistry A, 2020. **8**(27): p. 13522-13531.
349. Yin, P., et al., *A small-molecule/fullerene acceptor alloy: a powerful tool to enhance the device efficiency and thermal stability of ternary polymer solar cells.* Journal of Materials Chemistry C, 2020. **8**(32): p. 11223-11238.
350. Gu, H., et al., *Simultaneous Performance and Stability Improvement of Ternary Polymer Solar Cells Enabled by Modulating the Molecular Packing of Acceptors.* Solar RRL, 2020. **4**(10): p. 2000374.
351. Luo, D., et al., *Enhanced efficiency and stability of nonfullerene ternary polymer solar cells based on a spontaneously assembled active layer: the role of a high mobility small molecular electron acceptor.* Journal of Materials Chemistry C, 2020. **8**(18): p. 6196-6202.
352. Garg, A., et al., *Improved lifetimes of organic solar cells with solution-processed molybdenum oxide anode-modifying layers.* Progress in Photovoltaics, 2015. **23**(8): p. 989-996.
353. Lima, F.A.S., et al., *Flexible ITO-free organic solar cells applying aqueous solution-processed V2O5 hole transport layer: An outdoor stability study.* Apl Materials, 2016. **4**(2).
354. Vilkman, M., et al., *Effect of the Electron Transport Layer on the Interfacial Energy Barriers and Lifetime of R2R Printed Organic Solar Cell Modules.* Acs Applied Energy Materials, 2018. **1**(11): p. 5977-5985.
355. Roth, B., et al., *Improving the Operational Stability of PBDTTTz-4 Polymer Solar Cells Modules by Electrode Modification.* Advanced Engineering Materials, 2016. **18**(4): p. 511-517.
356. Zimmermann, B., U. Wurfel, and M. Niggemann, *Longterm stability of efficient inverted P3HT:PCBM solar cells.* Solar Energy Materials and Solar Cells, 2009. **93**(4): p. 491-496.
357. Angmo, D., et al., *Low-cost upscaling compatibility of five different ITO-free architectures for polymer solar cells.* Journal of Applied Polymer Science, 2013. **130**(2): p. 944-954.
358. Corazza, M., F.C. Krebs, and S.A. Gevorgyan, *Predicting, categorizing and intercomparing the lifetime of OPVs for different ageing tests.* Solar Energy Materials and Solar Cells, 2014. **130**: p. 99-106.

359. Jeong, J., et al., *Significant Stability Enhancement in High-Efficiency Polymer:Fullerene Bulk Heterojunction Solar Cells by Blocking Ultraviolet Photons from Solar Light.* Advanced Science, 2016. **3**(4): p. 1500269.
360. Uddin, A., et al., *Encapsulation of Organic and Perovskite Solar Cells: A Review.* Coatings, 2019. **9**(2).
361. Steinmann, V. and L. Moro, *Encapsulation requirements to enable stable organic ultra-thin and stretchable devices.* Journal of Materials Research, 2018. **33**(13): p. 1925-1936.
362. Giannouli, M., et al., *Methods for Improving the Lifetime Performance of Organic Photovoltaics with Low-Costing Encapsulation.* Chemphyschem, 2015. **16**(6): p. 1134-1154.
363. Ahmad, J., et al., *Materials and methods for encapsulation of OPV: A review.* Renewable and Sustainable Energy Reviews, 2013. **27**: p. 104-117.
364. Cros, S., et al., *Definition of encapsulation barrier requirements: A method applied to organic solar cells.* Solar Energy Materials and Solar Cells, 2011. **95**: p. S65-S69.
365. Yu, D., et al., *Recent progress on thin-film encapsulation technologies for organic electronic devices.* Optics Communications, 2016. **362**: p. 43-49.
366. Corazza, M., F.C. Krebs, and S.A. Gevorgyan, *Lifetime of organic photovoltaics: Linking outdoor and indoor tests.* Solar Energy Materials and Solar Cells, 2015. **143**: p. 467-472.
367. Berger, P.R. and M. Kim, *Polymer solar cells: P3HT:PCBM and beyond.* Journal of Renewable and Sustainable Energy, 2018. **10**(1): p. 013508.
368. Zhang, Y., et al., *Current Status of Outdoor Lifetime Testing of Organic Photovoltaics.* Advanced Science, 2018. **5**(8): p. 1800434.
369. Gevorgyan, S.A., et al., *Baselines for Lifetime of Organic Solar Cells.* Advanced Energy Materials, 2016. **6**(22): p. 1600910.
370. Gevorgyan, S.A., et al., *Interlaboratory indoor ageing of roll-to-roll and spin coated organic photovoltaic devices: Testing the ISOS tests.* Polymer Degradation and Stability, 2014. **109**: p. 162-170.
371. Angmo, D. and F.C. Krebs, *Over 2 Years of Outdoor Operational and Storage Stability of ITO-Free, Fully Roll-to-Roll Fabricated Polymer Solar Cell Modules.* Energy Technology, 2015. **3**(7): p. 774-783.
372. Reese, M.O., et al., *Consensus stability testing protocols for organic photovoltaic materials and devices.* Solar Energy Materials and Solar Cells, 2011. **95**(5): p. 1253-1267.
373. Hosel, M., et al., *Comparison of UV-Curing, Hotmelt, and Pressure Sensitive Adhesive as Roll-to-Roll Encapsulation Methods for Polymer Solar Cells.* Advanced Engineering Materials, 2013. **15**(11): p. 1068-1075.
374. Yan, F., et al., *Semitransparent OPV modules pass environmental chamber test requirements.* Solar Energy Materials and Solar Cells, 2013. **114**: p. 214-218.
375. *The world's largest BiOPV installation completed in France using Heliatek's Solar Film Solution, HeliaSol*. 2020 [cited 2020; Available from: https://www.heliatek.com/blog/the-worlds-largest-biopv-installation-completed-in-france-using-heliateks-solar-film-solution-heliasol/.
376. Roberts, S. and N. Guariento, *Building integrated photovoltaics /a handbook*. 2009, Basel, Boston, Berlin: Springer Science & Business Media.
377. Ribeiro, F., et al., *Laser assisted glass frit sealing of dye-sensitized solar cells.* Solar Energy Materials and Solar Cells, 2012. **96**: p. 43-49.
378. Emami, S., et al., *Development of hermetic glass frit encapsulation for perovskite solar cells.* Journal of Physics D: Applied Physics, 2018. **52**(7): p. 074005.
379. Formica, N., et al., *An Indium Tin Oxide-Free Polymer Solar Cell on Flexible Glass.* Acs Applied Materials & Interfaces, 2015. **7**(8): p. 4541-4548.

380. Fukuda, K., K. Yu, and T. Someya, *The Future of Flexible Organic Solar Cells.* Advanced Energy Materials.
381. Planes, E., et al., *Encapsulation Effect on Performance and Stability of Organic Solar Cells.* Advanced Materials Interfaces.
382. Gevorgyan, S.A., et al., *Lifetime of Organic Photovoltaics: Status and Predictions.* Advanced Energy Materials, 2016. **6**(2): p. 1501208.
383. Tanenbaum, D.M., et al., *Edge sealing for low cost stability enhancement of roll-to-roll processed flexible polymer solar cell modules.* Solar Energy Materials and Solar Cells, 2012. **97**: p. 157-163.
384. Kim, T., et al., *Facile preparation of reduced graphene oxide-based gas barrier films for organic photovoltaic devices.* Energy & Environmental Science, 2014. **7**(10): p. 3403-3411.
385. Clark, M.D., et al., *Ultra-thin alumina layer encapsulation of bulk heterojunction organic photovoltaics for enhanced device lifetime.* Organic Electronics, 2014. **15**(1): p. 1-8.
386. Romero-Gomez, P., et al., *Enhanced stability in semi-transparent PTB7/PC71BM photovoltaic cells.* Solar Energy Materials and Solar Cells, 2015. **137**: p. 44-49.
387. Lee, H.J., et al., *Solution processed encapsulation for organic photovoltaics.* Solar Energy Materials and Solar Cells, 2013. **111**: p. 97-101.
388. Krebs, F.C., et al., *Production of large-area polymer solar cells by industrial silk screen printing, lifetime considerations and lamination with polyethyleneterephthalate.* Solar Energy Materials and Solar Cells, 2004. **83**(2-3): p. 293-300.
389. Krebs, F.C., *Encapsulation of polymer photovoltaic prototypes.* Solar Energy Materials and Solar Cells, 2006. **90**(20): p. 3633-3643.
390. Hauch, J.A., et al., *Flexible organic P3HT:PCBM bulk-heterojunction modules with more than 1 year outdoor lifetime.* Solar Energy Materials and Solar Cells, 2008. **92**(7): p. 727-731.
391. Gevorgyan, S.A., et al., *Interlaboratory outdoor stability studies of flexible roll-to-roll coated organic photovoltaic modules: Stability over 10,000h.* Solar Energy Materials and Solar Cells, 2013. **116**: p. 187-196.
392. Angmo, D., et al., *Outdoor Operational Stability of Indium-Free Flexible Polymer Solar Modules Over 1 Year Studied in India, Holland, and Denmark.* Advanced Engineering Materials, 2014. **16**(8): p. 976-987.
393. Weerasinghe, H.C., et al., *New barrier encapsulation and lifetime assessment of printed organic photovoltaic modules.* Solar Energy Materials and Solar Cells, 2016. **155**: p. 108-116.
394. Livi, F., et al., *Round-Robin Studies on Roll-Processed ITO-free Organic Tandem Solar Cells Combined with Inter-Laboratory Stability Studies.* Energy Technology, 2015. **3**(4): p. 423-427.
395. Corazza, M., et al., *Role of Stress Factors on the Adhesion of Interfaces in R2R Fabricated Organic Photovoltaics.* Advanced Energy Materials, 2016. **6**(11): p. 1501927.

Tables

Device structure	Photoactive Layer (PAL)	PAL deposition technique	PAL solvent	PAL thick (nm)	PAL atmos	Cell (C) or Module (M)	Total Active Area (cm^2)	Light source	Light intensity (lux)	P_{in} ($\mu W \cdot cm^{-2}$)	P_{out} ($\mu W \cdot cm^{-2}$)	PCE (%)	Year	Ref.
Glass/ITO/PEDOT:PSS/PAL/PFN-Br/Al	PBDB-TF:IO-4Cl	Spin-coated	Hal	100	Inert	C	1.0	LED (2700 K)	1000	----	78.8	26.1	2019	[85]
		Blade-coated		179			4.0				72.1	23.9		
Glass/ITO/PEDOT:PSS/PAL/PFN-Br/Al	PM6:IT-4F	Spin-coated	Hal	100	Inert	C	1.07	LED (2700 K)	1000	----	62.8	20.8	2019	[105]
	PM6:ITCC										66.5	22.0		
Glass/ITO/PEDOT:PSS/PAL/TASiW12/Al	NF3000	Blade-coated	Hal	147	Inert	M (16)	216	White LED (5500 K)	1000		38.4		2020	[136]
Glass/ITO/ZnO/TPD-n:IT-4F/MoO_3/Ag	TPD-3F:IT-4F	Blade-coated	----	----	----	C	20.4	FC	1000	----	40.2	21.8	2020	[152]
ITO/PEDOT:PSS/PAL/Al	PCDTBT:$PC_{71}BM$	Spin-coated	Hal	70	Inert	M(8)	100	fluorescent lamp	300	----	9.38	11.2	2016	[157]
Glass/ITO/ETL/PAL/PEDOT:PSS/Al	Merck formulation	Spin-coated	----	200	----	M(8)	3.67	fluorescent lamp	1000	----	43.4			[158]
Glass/ITO/ZnO/PAL/MoO_3/Ag	BDT-2T-ID:PNP	Spin-coated	Hal	150-200	----	M(6)	9.6	White LED	200	76.8	11.7	15	2019	[159]
PEN/ITO/ZnO/PAL/MoO_3/Ag											10.6			
PET/ITO/AZO/PAL/MoO_3/Ag	1DTP-ID:PNP	Spin-coated	Hal	150-190	----	M(6)	9.6	White LED	200	----	10.0	17	2019	[160]
glass/ITO/ZnO/PAL/MoOx/Ag	PBDB-TSCl:IT-4F	Spin-coated	Hal	----	----	M(10)	58.5	fluorescent lamp	1000	298.5	37.06	12.42	2020	[161]
									3700	1182.1	169.73	14.36		
	PBDB-TF:IT-4F								1000	298.5	19.48	6.53		
									5000	1607.5	172.69	10.74		

Table 1. Performance of ITO-based large area (≥ 1.0 cm^2) OPV devices (cells and modules), under indoor light.

Tables for Supporting Information

	Device structure	Photoactive Layer (PAL)	PAL deposition technique	PAL solvent	PAL atmosp	PAL thick (nm)	Active Area (cm^2)	PCE (%) avg/max AM 1.5G	Year	Ref.
	Glass/ITO/PEI/PAL/m-PEDOT:PSS/PEI/PAL/hc-PEDOT:PSS	P3HT:ICBA	Spin-coated	Hal		----	1.05	3.78	2017	[36]
	Glass/ITO/ZnO/PAL/MoO_3/Ag	PBDB-T:ITIC	Spin-coated	Hal		~100	1.6	7.2	2018	[37]
							8.0	6.0		
	Glass/ITO/Ag-grid/ZnO/PAL/MoO_3/Ag		Blade-coated; Spin-coated; Maobi coated				52	2.2		
	glass/ITO/PEDOT:PSS/PAL/PFN-Br/Al	PBTA-TF:IT-M	Blade-coated	Non-Hal	Amb	~100	1.0	10.6	2018	[60]
	ITO/PEDOT/PAL/PNDIT-F3N/Ag	PM6/IT-4F (bilayer)	Blade-coated	Non-Hal	Amb		1	11.0/11.4	2019	[61]
		PM6:IT-4F						10.1/10.6		
		PffBT4T-2OD/$PC_{71}BM$						7.8 / 8.0		
		PffBT4T-2OD:$PC_{71}BM$						2.8 / 3.0		
	Glass/ITO/PEDOT:PSS/PAL/PDINO/Al	J71/ITC6-IC (LbL)	Blade-coated	Hal	Amb		1.00	10.24/10.35	2019	[62]
		PTQ10/IDIC (LbL)						10.18/10.42		
		J71:ITC6-IC (BHJ)						9.20 / 8.96		
		PTQ10:IDIC (BHJ)						9.04 / 8.75		
	ITO/PEDOT:PSS/PAL/PNDIT-F3N-Br/Ag	PM6:Y6 (BHJ)	Blade-coated	Hal		120	1.0	13.71/14.01	2020	[63]
		PM6/Y6 (LbL)						15.03/15.23		
	ITO/PEI:PAL1/PEDOT:PSS/PEI:PAL2/MoOx/Ag	PTB7-Th:$PC_{71}BM$	Slot-die coated	Hal	Inert	~75 / ~105	1.0	8.8 / 9.1	2016	[64]
	glass/ITO/PEDOT:PSS/PAL/Al	P3HT:PCBM	Slot-die coated				1	2.82 / 3.12	2014	[65]
	PET/ITO/AZO/PEIE/PAL/MoO_3/Ag	PTB7:$PC_{71}BM$	Slot-die coated				2	5.30/5.70	2017	[66]
	PET/ITO/ZnO/PAL/MoOx/Ag	PTB7-Th:PCBM:p-DTS(FBTTH$_2$)$_2$	Slot-die coated	Non-Hal	Amb	200	1	7.11	2019	[67]
							2	6.80		
	PET/ITO/ZnO/PAL/MoO_3/Ag	PTB7-Th:$PC_{71}BM$	Slot-die coated				1.04	9.10	2019	[68]
		PBDB-T:ITIC						9.77		
	glass/ITO/PEDOT:PSS/PAL/PFN-Br/Al	PBDB-T-SF:IT-4F	Slot-die coated	Hal	Amb	102	1.0	10.95/11.19	2019	[69]
	Glass/ITO-Metal grid/PAL/LiF/Al	P3HT:PCBM	Spray-coated	Hal	Amb	250	12.25	2.11	2011	[70]
	ITO/ZnO/PAL/PEDOT:PSS/Ag	P3HT:PCBM	Spray-coated	Hal		~270	15.25	1.33	2012	[71]
	ITO/PEDOT:PSS/PAL/Ca/Al	PBDT-TFQ:$PC_{71}BM$	Spray-coated	Hal	Amb	~120	1	4.6	2015	[72]

							10.2	4.1		
	Glass/ITO/PEDOT:PSS/PAL/Ca/Al	PCDTBT:$PC_{71}BM$	Spray-coated	Hal	Amb	55	1.65	3.7	2015	[73]
	glass/ITO/PEDOT:PSS/PAL/Ca/Al	P3HT:PCBM	Spray-coated	Hal		~250	1	2.9 / 3.0	2016	[74]
	glass/ITO/PEDOT:PSS/PAL/LiF/Al	PBTI3T:$PC_{71}BM$	Spray-coated				1	5.99 / 6.10	2016	[75]
	glass/ITO/PEDOT:PSS/PAL/LiF/Al	TQ1:$PC_{61}BM$	Spray-coated	Hal	Amb	110	1.0	1.4/1.5	2017	[76]
				Non-Hal		120	1.0	1.3/1.4		
	Glass/ITO/ZnO/PAL/PEDOT:PSS/Ag	PV2000 ink (Polyera)	Spin-coated		Amb	260	1	4.9 / ---	2015	[78]
	glass/ITO/ZnO/PAL/MoO_3/Ag	P3HT:O-IDTBR	Inkjet Printed	Hal	Amb	343	2	6	2019	[79]
	glass/ITO/MoOx/PAL/PFN-Br/Al	PB3T:I-TM	Spin-coated	Hal	Inert		1.0	10.1	2018	[80]
	Glass/ITO/PEDOT:PSS/PAL/ZnO/Al	PTB7-Th:PC71BM	Spin-coated	Hal	Inert	105	1.0	7.84	2016	[81]
					Amb		2.05	7.06		
	Glass/ITO/ZnO/PAL/MoO_3/Al	PBDB-T:ITIC	Spin-coated	Hal	Inert	100	1.0	10.68 / 11.21 10.78 [(a)]	2016	[82]
	ITO/ZnO/PAL/MoO_3/Al	PBDB-TF:BTP-4Cl	Spin-coated	Hal	Inert	100	1.0	14.8 / 15.3	2019	[83]
							0.81	15.08 [(a)]		
	glass/ITO/PEDOT:PSS/PAL/PFN-Br/Al	PBDB-TF: BTP-ec7	Blade-coated	Hal	Inert	100	1	7.42 / 8.75	2020	[84]
		PBDB-TF: BTP-ec9						15.5 / 16.2		
		PBDB-TF: BTP-ec11						14.8 / 15.4		
	glass/ITO/PEDOT:PSS/PAL/PFN-Br/Al	PBDB-TF:IO-4Cl	Spin-coated	Hal	Inert	100	1	9.43 / 9.80	2019	[85]
		PBDB-TF:IT-4F						12.1 / 12.5		
	ITO/PEIE/PAL/MoO_3/Ag	PTAZDCB20:$PC_{71}BM$	Spin-coated	Hal	Inert	313	1.0	--- / 8.01	2017	[86]
	ITO/PEIE/PAL/MoO_3/Ag	PDT2fBTBT10:$PC_{71}BM$	Spin-coated	Hal	Inert	351	1.0	--- / 9.42	2017	[87]
	ITO/ZnO/PAL/MoO_3/Al	PBDB-T-2F:IT-4F	Spin-coated	Hal	Inert	100	1.0	10.93	2018	[88]
		PBDB-T-2Cl:IT-4F						11.51		
	ITO/PEDOT:PSS/PAL/PFNDI-Br/Ag	P2F-EHp:IT-2F	Spin-coated	Hal	Inert	100	1	12.25 [(a)]	2018	[89]
	ITO/ZnO/PAL/MoO_3/Al	PBDB-TF-PTO2:IT-4F	Blade-coated	Non-Hal	Inert	140	1.07	12.3 / 13.1	2019	[90]
			Spin-coated	Hal		100		13.3 / 13.7		
	glass/ITO/PEDOT:PSS/PAL/Ca/Al	BDTT-S-TR:$PC_{71}BM$	Spin-coated	Hal	Inert	300	1.00	6.90/7.08	2015	[91]
							1.44	6.49/6.68		
	PET/ITO/ZnO/PAL/MoOx/Ag	PTB7-Th:p-DTS($FBTTH_2$)$_2$):$PC_{71}BM$	Slot-die-coated	Non-Hal	Amb	200 - 270	5	5.75	2017	[92]
	ITO/PEDOT:PSS/PAL/PDINO/Al	PM6/ICBA:IT-4F (PPHJ)	Blade-coated	Hal	Amb	----	1.05	14.25	2020	[93]
		PM6:ICBA:IT-4F (BHJ)						13.73		
	ITO/ZnO/PAL/MoO_3/Ag	P3HT:IDTBR:IDFBR	Spin-coated	Hal	Inert	85	1.0	6.5	2017	[94]
	Custom-ITO/PEDOT:PSS/PAL/PFNDI-Br/Ag	PBTA-Si:PTzBI-Si:N2200	Spin-coated	Non-Hal	Inert	350	1.0	10.01	2019	[95]

	ITO/MoO3/SC2/CGL/SC1/CGL/SC2/CGL/SC1/BPhen/Ag		Evaporated	-------	Inert	----	1	8.3 / ---	2015	[96]
	ITO/PEDOT:PSS/PAL/NDI-N/Al	PBDB-T-2F:IT-4F	Blade-coated	Hal	Inert	----	1.0	13.2	2019	[97]
	ITO/ZnO/PAL/MoO_3/Al	PBDB-TF:IT-4F	Blade-coated	Hal	Inert	----	1.04	9.12 / 9.22	2019	[98]
	ITO/Al(acac)$_3$/PAL/MoO_3/Ag (15 nm) (ST)	PM6:Y6	Spin-coated	Hal	Inert		1.0	11.28	2020	[99]
	glass/ITO/FPI-PEIE/PAL/MoO_3/Ag	PBDTT-F-TT:$PC_{71}BM$	Spin-coated	Hal	Inert	96	1	5.70	2015	[100]
	glass/ITO/PEDOT:PSS/ZnO/PAL/MoOx/Ag	PffBT4T-2OD:$PC_{61}BM$:$PC_{71}BM$	Spin-coated				1	8.5/8.6	2016	[101]
	PET/ITO/ZnO/PAL/MoOx/Ag	PPDT2FBT:$PC_{71}BM$	Slot-die coated	Hal			7	3.54	2017	[102]
	Glass/ITO/PV-E002/PAL/PEDOT:PSS-388/PEDOT:PSS-PH1000/Ag	PBTZT-stat-BDTT-8:$PC_{61}BM$	Blade-coated	Non-Hal	Amb	250	1.0	7.2 / 7.5	2016	[103]
	PET/ITO/TiOx/PAL/PEDOT:PSS/Ag	P3HT:PCBM	Blade-coated	Non-Hal	Inert	250	1	--- / 2.7	2011	[104]
	glass/ITO/PEDOT:PSS/PAL/PFN-Br/Al	PBDB-TF:ITCC	Spin-coated	Hal	Inert	100	1	9.98/10.3	2019	[105]
		PBDB-TF:$PC_{71}BM$						8.21/8.43		
		PBDB-TF:IT-4F						11.9/12.2		
	glass/ITO/ZnO/PAL/MoOx/Ag evaporated	PBTZT-stat-BDTT-8:$PC_{61}BM$	Blade-coated				1.04	6.0	2017	[306]
W/O VACUUM	glass/ITO/PEDOT:PSS/ZnO/PAL/AgNWs:PEDOT:PSS	PffBT4T-2OD:$PC_{61}BM$:$PC_{71}BM$	Spin-coated				1	7.4/7.7	2016	[101]
	glass/ITO/PEDOT:PSS/PAL/Field's metal	P3HT:PCBM	Slot-die-coated	Hal	Amb	100-180	3	2.4	2017	[107]
	glass/ITO/PEDOT:PSS/PAL/PFN/Field's metal	PTB7:$PC_{71}BM$	Spin-coated	Hal	Inert	100-110	2.25	2.8/3.1	2018	[108]
	PET/ITO/ZnO/PAL/PEDOT:PSS/Ag-printed	PSBTBT:PDI-DTT	Slot-die coated	Hal	Amb	----	4.2	0.204	2013	[109]
	glass/ITO/ZnO/PAL/PEDOT:PSS/Ag-inkjet-printed	P3HT:PCBM	Spin-coated	Hal	Amb	200	1	1.96 / ---	2013	[110]
	glass/ITO/ZnO/PAL/PEDOT:PSS/Ag-screen-printed (grid)							1.41 / ---		

[(a)] Certified efficiencies

Table S1. Performance, under AM 1.5G, of ITO-based large area (≥ 1.0 cm^2) single cells with and without metal evaporated top electrodes

	Device Structure	PAL layer	PAL deposition technique	PAL solvent	PAL atmos	PAL thick	Nº cells per module	Total Active Area / Total area (cm^2)	GFF (%)	APCE[(a)] (%) avg/max	MP CE[(a)] (%) avg/ max	Year	Ref.
WITH VACUUM	Glass/ITO/ZnO/PAL/MoO_3/Ag	PBDB-T:ITIC	Blade-coating; Maobi coating	Hal	Inert		5	21		5.1		2018	[37]
	glass/ITO/PEDOT:PSS/PAL/Al	P3HT:PCBM	Slot-die coated	Hal	Amb	----	33	198 / ---	----	----	1.73	2014	[65]
	PET/ITO/AZO/PEIE/PAL/MoO_3/Ag	PTB7:$PC_{71}BM$	Slot-die coated	Non-Hal	Amb	70	20	20	----	4.12/4.34	----	2017	[66]
	glass/ITO/PEDOT:PSS/PAL/PFN-Br/Al	PBDB-T-SF:IT-4F	Slot-die coated	Hal	Amb	102	2	2.0		8.98 / 9.01		2019	[69]
	glass/ITO/PEDOT:PSS/PAL/LiF/Al	PBTI3T:$PC_{71}BM$	Spray-coating	Hal	Amb		6	38.5 / ---	----	5.03 / 5.27	----	2016	[75]
	PET/ITO/ZnO/PAL/MoOx/Ag	PTB7-Th:p-DTS(FBTTH$_2$)$_2$):$PC_{71}BM$	Slot-die-coated	Non-Hal	Amb		2	10 /		5.82		2017	[92]
							4	20 /		5.18			
	ITO/PAL/Al	MEH-PPV/C_{60}	Screen-printing / thermal evaporation	Hal / ---	Amb / ---	--- / 200	91	655 /	----	0.0002	----	2007	[117]
	ITO/HTL/PAL/Ca/Al	P3HT:PCBM	Spin-coated	Hal	Inert	----	54	108 / 231	47	3.4 (b)	1.1 (b)	2009	[118]
	ITO/AZO/PAL/PEDOT:PSS/Ag	P3HT:PCBM	Blade-coated	Hal	Amb	100	10	1.15 /	83	1.38		2013	[119]
	Glass/ITO/PAL1/IML/PAL2/Ag (tandem)	P3HT:Si-PCPDTBT:PCBM	Blade-coated	Hal	Amb	130 / 200	10	1.1 / ---	85	3.3	----	2014	[120]
	PET/IMI/Al-doped ZnO (AZO)/PAL/PEDOT:PSS/Ag	P3HT:PCBM	Slot-die coated	Non-Hal	Amb	150 – 200	14	35.0	> 95	3.07		2014	[121]
	Glass/FTO/ZnO/PAL/PEDOT:PSS/Ag	PBTZT-stat-BDTT-8:PCBM	Blade-coated	Non-Hal	Amb	220	14	35/35.5	98.5	4.5 / 5.3	----	2016	[122]
	PET/IMI/ZnO/PAL/PEDOT:PSS/Ag		Slot-die coated							4.0 / 4.2	----		
	Glass/ITO/PAL/Ag	HDR14:C_{60}	Evaporated	-------	-----	30	6	64 / 68	94	4.3		2016	[124]
	glass/ITO/ZnO/PAL/MoOx/Ag	PM6:Y6:$PC_{61}BM$	Blade-coated	Hal	Amb	100 – 110	12	25.0/26.2	> 95	13.19 (b)	12.6	2020	[125]
							33	194.8/204.0		12.28 (b)	11.7		
	glass/ITO/ZnO/PAL/MoO_3/Ag	PBDTTT-C:$PC_{71}BM$	Spin-coated	Hal		87 – 118	7	50.4 / ---		5.4	----	2016	[128]
	Glass/ITO/PEI/MoOx/PAL/Al - Glass/ITO/PEI/PAL/MoOx/Al	PCDTBT:$PC_{71}BM$	Spin-coated	Hal		70		10.7 / 11.1	96	4.24		2013	[129]
	ITO/ZnO/PAL/MoO_3/Ag	PTB7-Th:$PC_{71}BM$	Slot-die coated	Hal	Amb	125	3	4.15	90	8.1	7.5 (b)	2016	[130]
								8.30		7.7	7.0		

								12.45		7.4	6.7		
								16.60		7.5	6.7		
Glass/ITO/NDI-PFNBr@ZnO/PAL/MoO_3/Ag	PTB7-Th:$PC_{71}BM$	Blade-coated	Hal	Amb		4	16 /		8.05		2019	[131]
						13	93 /		4.49			
Glass/ITO/ZnO/PAL/MoO_3/Ag						4	16 /		7.11			
Glass/ITO/PEDOT:PSS/PAL/Al	POD2T-DTBT:$PC_{71}BM$	Blade-coated	Hal	Amb	98	10	108 /	~	3.64		2015	[132]
	P3HT:$PC_{61}BM$				221		~180	60	2.66			
ITO/PEDOT:PSS/PAL/LiF/Al	P3HT:PCBM	Blade-coated	Hal		200	3	10.8 / ---	----	2		2017	[133]
ITO/PEDOT:PSS/PAL/LiF/Al (opaque)	PTB7-Th:$PC_{71}BM$	Blade-coated	Hal	Amb	110	3	10.8 /	----	5.9	----	2017	[134]
ITO/PEDOT:PSS/PAL/LiF/Al/Ag (ST)									5.3			
ITO/PEDOT:PSS/PAL/LiF/Al (opaque)	PBDTTT-CT:$PC_{71}BM$		Non-Hal		100				4.2			
ITO/PEDOT:PSS/PAL/LiF/Al/Ag (ST)									3.8			
ITO/PEDOT:PSS/PAL/LiF/Al (opaque)	PCDTBT:$PC_{71}BM$		Hal		80				2.9			
ITO/PEDOT:PSS/PAL/LiF/Al/Ag (ST)									1.9			
ITO/PEDOT:PSS/PAL/LiF/Al (opaque)	P3HT:PCBM				200				2.7			
ITO/PEDOT:PSS/PAL/LiF/Al/Ag (ST)									2.1			
Glass/ITO/PEDOT:PSS/PAL/MSAPBS/Al	PTB7-Th:$PC_{71}BM$	Blade-coated	Hal	Amb	----	16	216 /		5.6 [(b)]		2018	[135]
Glass/ITO/PEDOT:PSS/PAL/TASiW12/Al	NF3000-P:NF3000-N	Blade-coated	Hal	Inert	100	3	10.8 / ---		9.80		2020	[136]
					147	16	216 / ---		9.50			
glass/ITO/PEDOT:PSS/PAL/LiF/Al	PBDTTT-EFT:$PC_{71}BM$	Blade-coated	Hal	Inert	----	16	216 / ---	----	5.16 / 5.20	----	2019	[137]
glass/ITO/PEDOT:PSS/PAL/LiF/Al			Non-Hal						5.00 / 5.03			
glass/ITO/PEDOT:PSS/PAL/ZrAcac/Al			Non-Hal						5.12 / 5.27			
				Amb					3.21 / 3.67			
Glass/ITO/ZnO/PAL/MoO_3/Ag	PTB7-Th:$PC_{71}BM$	Blade-coated	Non-Hal	Amb	230	4	16 /		7.5		2017	[138]
Glass/ITO/PEDOT:PSS/PAL/Al	POD2T-DTBT:$PC_{71}BM$	Blade-coated	Non-Hal	Amb	----	3	9.6 / ---		4.17	----	2017	[139]
					----	5	8.0 / ---		4.30			
			Hal		110	3	9.6 / ---		4.07			
					110	5	8.0 / ---		4.20			
					85	8	24.0 / ---		3.93			
	PDTBT-alt-TT:$PC_{71}BM$				----	3	9.6 / ---		5.49			
					----	5	8.0 / ---		5.87			
					----	8	24.0 / ---		5.58			
ITO/PEDOT:PSS/PAL/PFN-Br/Al	PBDB-TF:IT-4F	Blade-coated	Hal	Amb	100	3	12.6 / 21	60	10.21		2019	[140]
Glass/ITO/PEDOT:PSS/PAL-1/ZnO-NPs/PEDOT:PSS/Nafion/PAL-2/LiF/Al	PAL-1: PCDTBT:$PC_{71}BM$	Blade-coated	Hal	Amb	125-140 /	3	1.3 / ---		5.2		2016	[141]
						5	2.1 / ---		4.7			

		PAL-2: Si-PCPDTBT:$PC_{71}BM$				75-105							
	glass/ITO/ZnO/PAL/MoO_3/Al	PCDTBT:$PC_{71}BM$	Slot-die coated	Hal	Amb		6	35.2 /		3.18		2017	[142]
	Glass/ITO/PEDOT:PSS/PAL/Ca/Al	BTR:$PC_{71}BM$	Slot-die-coated	Non-Hal	Amb	----	4	10 /		4.40 / 4.83		2017	[143]
	ITO/PEDOT:PSS/PAL/BCP/Ag	LGC-D073:$PC_{71}BM$	Slot-die coated	Hal	Amb	----	4	24	50	4.17 / 5.50		2019	[144]
		LGC-D023:$PC_{71}BM$								3.90 / 4.53			
	glass/ITO/PEI/PAL/PEDOT:PSS/Ag	PV2000:PCBM	Slot-die coated	Non-Hal	Amb		5	23.7 / ---	----	7.56 [(b)]		2019	[145]
	glass/ITO/ZnO/PAL/MoO_3/Ag	PTB7-Th:$PC_{71}BM$:COi8DFIC	Slot-die-coated	Hal	Amb		5	30 /		8.6		2019	[146]
	PET/ITO/ZnO/PAL/MoO_3/Ag		R2R							9.6			
	PET/TCO/ZnO/PAL/MoO_3/Ag	P3HT:PCBM	Reverse Gravure-coating	Hal	Amb		5	45 / ---		2.1		2016	[147]
	glass/ITO/ZnO/PAL/MoO_3/Ag	PBDB-T:ITIC	Maobi coating	Hal	Amb		14	18		6.3		2018	[148]
	glass/ITO/ZnO/PAL/MoO_3/Ag	PBDB-T-2F:IT-4F	water transfer printing	Hal	Amb	100	4	3.2		8.1		2019	[149]
	ITO/PEDOT:PSS/PAL/Ca/Al	BDT_2 :$PC_{71}BM$	Spin-coating	Hal	Amb	90	11	77.8 /		7.45 7.2 [(b)]		2016	[150]
	glass/ITO/ZnO-NPs/PAL/MoOx/Ag	PNTz4T-5MTC:$PC_{71}BM$	D-bar-coated	Non-Hal	Amb	240	11	54.45 /		6.46 / 6.61		2019	[151]
		PNTz4T:$PC_{71}BM$				100				3.91 / 4.29			
	glass/ITO/ZnO/PAL/MoO_3/Ag	TPD-3F:IT-4F	Spin-coated	Non-Hal	Amb		5	20.4	37	10.08 [(a)]		2020	[152]
			Spin-coated					29.75 / 81		10.13			
			Blade-coated							10.40			
	Glass/ITO/ZnO/PEIE/PAL/MoOx/Ag.	PTB7-Th:EH-IDTBR:T2-OEHRH	D-bar-coated	Non-Hal	Amb	100	11	55.5		/ 9.32		2020	[153]
	ITO/PEDOT:PSS/PAL/PNDIT-F3NBr/Ag	PM6:DTY6	Blade-coated	Non-Hal	Amb	110	6	18 / 25.5	70.6	14.4		2020	[154]
	ITO/PEDOT:PSS/PAL/ZnO/Al	PBTIBDTT:ITIC-F	Spin-coated	Hal			5	3.48 / 4.0	87	/ 8.6	/ 7.48	2018	[155]
	glass/ITO/PEDOT:PSS/PAL/ZrOx/Al	PBDB-T:ITIC:$PC_{71}BM$	Blade-coated	Hal	Inert	103	16	216 /		/ 7.7		2019	[156]
	Glass/ITO/ETL/PAL/PEDOT:PSS/Al	Merck formulation	Spin-coated	----	Inert	200	8	3.67 / 4.5	81.8	4.4		2017	[158]
WITHO	IMI/ETL/PAL/HTL/TCL/Ag	PBTZT-stat-BDTT-8:$PC_{61}BM$	Blade-coated	Non-Hal	Amb		9	114.5 / ~120	~95	4.3 / 4.5		2016	[103]
	glass/ITO/PEDOT:PSS/PAL/Field's metal cathode	P3HT:PCBM	Slot-die coated	Hal	Amb		3	9 /		/ 2.1		2017	[107]
	ProcessOne	P3HT:PCBM	Slot-die-coated	Hal	Amb	127		96		1.79 / 2.00		2010	[115]
								160		1.22 / 1.36			

UT VACUUM								360		1.18 / 1.69			
	PET/TCO/ZnO/PAL/PEDOT:PSS/Ag(PV4 16)	P3HT:PCBM	Reverse gravure coated	Hal	Amb		5	45		2.1		2016	[147]
	glass/ITO/Cs_2CO_3/PAL/m-PEDOT (ST)	P3HT:PCBM	Spray-coated	Hal	Amb		50	30 /		1.80		2011	[165]
	PET/ITO/ZnO/PAL/PEDOT:PSS/Ag	P3HT:PCBM	Slot-die coated				13	156 /	92.5	1.15		2015	[166]
	glass/ITO/PEDOT:PSS/PAL/ZnO/AgNW	pDPP5T-2:$PC_{61}BM$	Blade-coated	Hal	Amb	120	10	1.6 /	> 95	2.25		2015	[167]
							16	64 /	> 95	2.34			
	PET/ITO/ZnO/PAL/PEDOT:PSS/Ag	P3HT:PCBM	Gravure Printed	Hal	Amb		8	8 /		2.22		2016	[168]
	PET/ITO/Ag/ITO/PAL/PEDOT:PSS/Ag	PV-D4610:$PC_{71}BM$	Slot-die coated	Hal		200		100 /		2.87		2016	[169]
	PET/ITO/PEIE/PAL/PEDOT:PSS/Ag-grid	P3HT:PCBM	Reverse gravure coated	Hal	Amb	200	5	52.5 /		2.1 /		2016	[170]
	glass/FTO/ZnO/PAL/PEDOT:PSS /AgNW	PBTZT-stat-BDTT-8:PCBM	Blade-coated	Non-Hal	Amb		30	197.40	94	4.8		2017	[171]
	PET/IMI/ZnO/PAL/PEDOT:PSS /AgNW		Slot-die coated			290	19	68.76		4.3			
	glass/ITO/ZnO/PAL/PEDOT:PSS	P3HT:PCBM	Spray-coated	Hal	Amb	200	3	12		2.44		2018	[172]
		P3HT:PCBM	Inkjet printing	Hal	Amb			84		1.60		2018	[173]
	ITO/ZnO/PAL/PEDOT:PSS/Ag	P3HT:ICBA	Gravure printing	Hal			20	57		3.4		2018	[174]
	glass/ITO/ZnO/PAL/PEDOT:PSS/AgNW	P3HT:IDTBR	Blade-coating	Hal	Amb	200	12	59.52 / 64		4.8 / 5.0		2018	[175]
			Slot-die-coated							4.3 / 4.4			
			Blade-coating	Non-Hal						4.5 / 4.7			
	ITO/ZnO/PAL/WO_3/HTL /Ag	SMD2:ITIC	Slot-die coated	Hal	Amb	200	10	80 /	74.7	5.25		2019	[176]
	PET/IMI/SnOx/PAL/PEDOT:PSS/AgNWs	P3HT:PCBM	Blade-coated	Hal	Amb	250	10	40 /		2.4		2019	[177]

(a) APCE is the PCE of the module in active area and MPCE is the PCE of the module in total area.
(b) Certified efficiencies

Table S2. Performance of ITO-based large area (≥ 1.0 cm^2) modules with and without metal evaporated top electrodes

	Bottom Electrode (TCE/BE)	Device Structure	PAL	Cell (C) or Module (M) (nº cells)	Total Active Area / Total area (cm^2)	APCE (%) avg/max	Year	Ref.
Metal grids	Ag-grid	PET/TCE/PEDOT:PSS/ZnO/PAL/PEDOT:PSS/Ag-grid	PV2000 (Polyera)	C	1	4.1	2015	[78]
			P3HT:PCBM			1.6		
		PET/TCE/ZnO/PAL/MoOx/Ag	PTB7-Th:p-DTS(FBTTH$_2$)$_2$):PC$_{71}$BM	C	1.25	8.28	2017	[92]
		PET/TCE/PEDOT:PSS/ZnO/PAL/MoOx/Ag	PffBT4T-2OD:PC$_{61}$BM:PC$_{71}$BM	C	1.2	7.6	2016	[101]
		PET/TCE/PEDOT:PSS/ZnO/PAL/AgNWs:PEDOT:PSS				5.8		
		PET/TCE/PEDOT:PSS/ZnO/PAL/PEDOT:PSS/Ag	P3HT:PCBM	C	6	1.84		[198]
		PET/TCE/PEDOT:PSS/ZnO/PAL/PEDOT:PSS/	P3HT:PCBM	M (16)	15.4/ 30.8	1.7	2013	[199]
		PET/TCE/PEDOT:PSS/ZnO/PAL/PEDOT:PSS/Ag	P3HT:PCBM	C	1	1.8	2014	[200]
		PET/TCE/PEDOT:PSS/ZnO/PAL/PEDOT:PSS/Ag	P3HT:PCBM	C	1	1.5	2013	[201]
		PET/TCE/PEDOT:PSS/ZnO/PAL/PEDOT:PSS/Ag	P3HT:PCBM	C	6	2.1	2013	[202]
				M (4)	24 / ---	2.09		
		PET/TCE/PEDOT:PSS/ZnO/PAL/PEDOT:PSS/Ag	P3HT:PCBM	C	1	2.2	2015	[203]
		PET/TCE/PAL/PEDOT:PSS/ZnO/PAL/PEDOT:PSS/Ag	P3HT:PCBM	C	1	1.3	2014	[204]
		PET/TCE/PEDOT:PSS/ZnO/PAL/HTL/Ag-grid	P3HT:PC$_{61}$BM	C	1	2.05		[205]
		PET/TCE/PEDOT:PSS/ZnO/PAL/PEDOT:PSS/Ag-grid	P3HT:PC$_{61}$BM	M (4)	24.00 / 38.28	1.36	2013	[207]
				M (7)	70.00/ 110.47	1.60		
				M (9)	121.5 / 186.20	1.62		
		PET/TCE/PEDOT:PSS/ZnO/PAL/PEDOT:PSS/Ag	P3HT:PCBM	C	6	1.82	2013	[208]
				M (11)	66 / ---	1.50/1.60		
		PET/TCE/PEDOT:PSS/ZnO/PAL/PEDOT:PSS/Ag-grid	P3HT:PCBM	C	1	2.3	2014	[209]
				M (4)	8 / ---	2.1		
			PV-D4610:PCBM	C	1	3.2		
				M (4)	8 / ---	3.0		
			PDTSTTz-4:PCBM	C	1	3.0		

				M (4)	8 / ---	3.2		
			PBDTTTz-4:PCBM	C	1	3.0		
				M (4)	8 / ---	2.9		
		PET/TCE/HC-PEDOT:PSS/ZnO/PAL/PEDOT:PSS/Ag	P6:PCBM	C	1	3.8	2014	[212]
		PET/TCE/PEDOT:PSS/ZnO/PAL/PEDOT:PSS/Ag	P3HT:DPP(BT-N_3)$_2$	C	1	0.067	2014	[213]
		PET/TCE/PEDOT:PSS/ZnO/PAL/PEDOT:PSS/Ag-grid	P3HTT–DPP-10%: PCBM	C	1	1.31	2014	[214]
		TCE/PAL/PEDOT:PSS/ZnO/PAL/PEDOT:PSS/Ag-grid				1.36		
		PET/TCE/PEDOT:PSS/ZnO/PAL/PEDOT:PSS/Ag	PDTSTTz-4:PCBM	C	1.0	3.35 / 3.5	2013	[216]
		PET/TCE/PEDOT:PSS/ZnO/PAL/PEDOT:PSS/Ag-grid	SMs 1-4 : PCBM	C	1.0	1	2014	[217]
		PET/TCE/PEDOT:PSS/PH1000/ZnO/PAL/PEDOT:PSS EL-P5010/Ag	PBDTTT-C-T/$PC_{71}BM$	C	1	2.09	2014	[220]
		14-layer tandem stack	MH301:PCBM & MH306:PCBM	M (8)	52.2 / ---	1.76	2014	[221]
		PEN/TCE/PEDOT:PSS/PAL/LiF/Al	P3HT:$PC_{61}BM$	C	4	1.93	2011	[222]
		glass/TCE/PEDOT:PSS/PAL/LiF/Al	P3HT:PCBM	C	4	1.92	2012	[223]
		PET/TCE/VPP-PEDOT/ZnO/PFN/PAL/MoO_3/Al	P3HT:$PC_{61}BM$	C	1.21	3.36	2015	[224]
		PET/TCE/PEDOT:PSS/ZnO/PFN/PAL/MoO3/Ag	P3HT:$PC_{61}BM$	C	1.21	3.36	2014	[225]
		PET/TCE/PEDOT:PSS/ZnO/PFN/PAL/MoO3/Ag	PTB7:$PC_{71}BM$	C		5.85		
		PET/TCE/PEDOT:PSS/PAL/LiF/Al	P3HT:PCBB-C8	C	1.21	/1.36	2013	[226]
		PET/TCE/PEDOT:PSS/PAL/AZO/Al	P3HT:ICxA	C	4.0	0.88	2016	[227]
		TCE/PEDOT:PSS/ZnO/PAL/PEDOT:PSS/Ag	PTB7:$PC_{71}BM$	C	2.10	5.79	2016	[228]
		PET/TCE/PEDOT:PSS/ZnO/PFN/PAL/MoO_3/Ag	PTB7-Th:$PC_{71}BM$	C	2.25	6.51	2017	[229]
		PET/TCE/PEDOT:PSS/ZnO/PAL/PEDOT:PSS/Ag	PBDTTTz-4:PCBM	C	1.0	3.5/	2015	[230]
				M (16)	29 / ---	3.3/		
		PET/TCE/PEDOT:PSS/PAL/NP-ZnO/Ag	PM6:IDIC	C	1.25	6.54	2018	[231]
		PET/TCE/PEDOT:PSS/ZnO/PAL/PEDOT:PSS/Ag-grid	PBDTTTz-4:PCBM	C	1	3.71 / 3.77	2015	[249]
	Cu/Au-grid	SU8/TCE/PEDOT:PSS(PH1000)/PEIE/PAL/ MoO_3/Ag	P3HT:ICBA	C	9.3	2.4	2015	[235]
	Mo/Al/Mo grid	Glass/TCE/PEDOT:PSS/PAL/LiF/Al	P3HT:PCBM	C	2.4	1.6	2014	[236]
					14.4	0.8		
		glass/TCE/PEDOT:PSS/ZnO/PAL/MoOx/Ag	P3HT:PCBM	M (4)	92 / ---	0.98	2015	[237]
	Ag/Cu-grid	PET/TCE/E100/ZnO/ZrAcac/PAL/MoO_3/Al	PBDB-T:ITIC	C	1.0	9.37	2019	[238]
			PTB7-Th:$PC_{71}BM$			8.15		
			PBDB-TF:IT-4F			11.18		
			NF3000-P:NF3000-N			12.26		
			PBDB-T:ITIC		2.4	8.75		

					4	7.79		
					9	7.35		
Metal Nano-wires	AgNWs	PET/TCE/ZnO/PAL/MoOx/Ag	PPDT2FBT:$PC_{71}BM$	C	7.0	/ 3.04	2017	[102]
	AgNW	PET/TCE/ZnO/PAL/PEDOT:PSS/Ag-grid	PBDTTTz-4:PCBM	C	1	3.09 / 3.30	2015	[249]
	AgNWs	glass/TCE/ZnO/PAL/PEDOT:PSS/AgNWs	PV2000:$PC_{71}BM$	C	1.0	4.3	2016	[250]
	AgNWs@PI	TCE/ZnO/PAL/HXMoO_3/PEDOT:PSS/AgNWs	PBDB-T-2F:IDIC:Y6	C	1.0	10.3	2020	[252]
UTMF	Ag (< 20 nm)	PET/TCE/ZnO/PAL/PEDOT:PSS/Ag	P3HT:PCBM	C	1	1.6	2012	[261]
				M	35.5 / ---	0.44		
	Ag (8 nm)	TCE/MoOx (10 nm)/PAL/BCP/Al	PCDTBT:$PC_{71}BM$	C	1.0	3.7	2012	[262]
	Au (8 nm)					4.25		
Carbon based	rGOMM	PET/TCE/PAL/TiOx/Al	PCDTBT:$PC_{71}BM$	C	1.35	1.07	2015	[291]
	graphene/PEDOT:PSS	Glass/TCE/ZnO/PEIE/PAL/V_2O_5/Ag	PffBT4T-2OD:$PC_{71}BM$	M (3)	1.6 / ---	0.44	2018	[292]
PEDOT:PSS	hc-PEDOT:PSS	PET/TCE/ZnO/PAL/MoO_3/Ag	PTB7-Th:$PC_{71}BM$	M (6)	15 / 25	7.25 / 7.58	2019	[68]
			PBDB-T:ITIC			8.64 / 8.90		
	PEDOT:PSS PH1000	Glass/TCE/MoOx/PAL/Ca/Al	BQR:$PC_{71}BM$	C	1.6	5.2	2019	[301]
Opaque Bottom electrode	Ag film (80 nm)	PES/BE/PEI/PAL1/m-PEDOT:PSS /PEI/PAL2/hc-PEDOT:PSS/Ag-grid	P3HT:ICBA(1) & PTB7-Th:PC61BM (2)	C	10.50	6.50	2017	[36]
			P3HT:ICBA (1 & 2)		10.90	4.43		
	Ag film (100 nm)	glass/BE/FPI-PEIE/PAL/MoO_3/UTMF-Ag/TeO_2	PBDTT-F-TT:$PC_{71}BM$		1 /	7.21	2015	[100]
	Ag film	PET/BE/ZnO/PAL/PEDOT:PSS/Ag-grid	P3HT:PCBM	C	1	2.52	2014	[303]
	Ag film (100 nm)	glass/BE/PFN/PAL/MoO_3/thickness-gradient Ag TCE/MoO_3	PTB7-Th:$PC_{71}BM$	C	4	7.15	2015	[304]
	Ag film (100 nm)	glass/BE/PFN/PAL/MoO_3/triangular shaped Ag grid/MoO_3	PTB7:$PC_{71}BM$	C	4	6.02 / 6.41	2017	[305]
		glass/BE/PFN/PAL/MoO_3/triangular shaped Ag grid/MoO_3	PTB7-Th:$PC_{71}BM$	C	4	6.71 / 6.93		
		PET/BE/PFN/PAL/MoO_3/triangular shaped Ag grid/MoO_3	PTB7-Th:$PC_{71}BM$	C	4	6.09 / 6.73		
	Ag film (165 nm)	Glass/BE/ZnO/PAL/PEDOT:PSS:AgNWs	PBTZT-stat-BDTT-8:PCBM	C	1.04	4.5	2017	[306]
				M	19.7 / ---	3.6		
	Ag film (100 nm)	BE/TiOx/ZnO/PAL/PEDOT:PSS	PTB7-Th:ITIC	C	2.03	7.32 / 7.60	2018	[307]

	Ag film (100 nm)	PET/BE/TiOx/ZnO/PFN/PAL/PEDOT:PSS	PTB7-Th:PNDI-T10	C	2.03	6.42/6.65	2018	[308]
			PTB7-Th:$PC_{71}BM$	C		5.32/5.71		
	Ag(100 nm) film	Glass/BE/PFN/PTB7:$PC_{71}BM$/PEDOT:PSS	PTB7:$PC_{71}BM$	C	1.0	4.81	2019	[309]
	$HxMoO_3$/Ag film (70 nm)	glass/BE/PAL/$HxMoO_3$/Ag (8nm)/MoO_3	PM6:IT-4F	C	10	9.91 / 10.24	2020	[310]
	Al film (100 nm)	glass/BE/PAL/MoOx/Ag/MoOx	PCDTBT:$PC_{71}BM$	C	25.0	3.08 / 3.17	2012	[311]
					2.9			
	Al film (120 nm)	glass/BE/PAL/MoOx/Ag/ZnS	PCDTBT:$PC_{71}BM$	C	25	2.7	2014	[312]
	Al film (100 nm)	Glass/BE/PAL/PEDOT:PSS/Ag	PF2:$PC_{71}BM$	M (15)	66 / ---	6.1	2019	[313]
	Al/Cr	Kapton/BE/PAL/PEDOT:PSS/Ag	P3HT:PCBM	C	3	1.4	2011	[314]
				M (16)	235 / ---	0.5		
	Steel foil	BE/PEDOT:PSS/PAL/LiF/Al/Ag/ZnS	P3HT:PCBM	C	1.0	1.3	2012	[315]
	Cr/Al/Cr	BE/PAL/PEDOT:PSS/metal-grid	P3HT:PCBM	C	1.1	2.7	2014	[316]

Table S3. Performance of ITO-free large area (≥ 1.0 cm^2) OPV cells and modules

Active area (cm^2)	PAL	Encapsulation system	Initial PCE (%)	Test protocols	Location	Test duration	Lifetime	Year Published	Ref.
1.1	PAL-1	Glass-glass & UV curing epoxy glue	2.7	Continuous illumination 1000 W/m^2; low UV content; T ~ 50 ºC and RH ~ 6% (IEC 61646).	-------	-------	T_{90} > 500 days	2014	[316]
> 1	PAL-1	Barrier film	> 1	outdoor	Lowell, MA (USA)	13 months	T_{80} > 1 year	2008	[390]
35.5	PAL-1	UV filter/barrier (Amcor); pressure sensitive adhesive (467 MPF, 3 M)	1.43	Outdoor ISOS-O-3	Germany, Israel, Australia, Denmark	17 months	T_{80} > 416 days	2013	[391]
70 – 100	PAL-1	Barrier foil and adhesive; edge sealing margin > 1 cm	> 1.5	Outdoor: ISOS-O-1 (Netherlands); ISOS-O-3 (Denmark)	DTU (Denmark); ECN (Netherlands)	1 year	T_{80} > 1 year	2014	[392]
100	PAL-1	PET barrier foil with thickness of ~60 µm from Amcor (Batch E75Y08). UV-curable adhesive from DELO (DELO-Katibobond LP 655)	~ 2	Outdoor ISOS-O-3	Roskilde, Denmark	2 years	T_{80} > 2 years	2015	[371]
50	PAL-1	3M™ Ultra Barrier Solar Films, EVA sheets and edge sealing tape	N.A.	Outdoor ISOS-O-2	Victoria, Australia	1 year	Estimated T_{80} ~ 3 year	2016	[393]

Table S4. For each reference, only the best device stability results are indicated. PAL-1 = P3HT:PCBM